

TECHNISCHE UNIVERSITÄT WIEN

INSTITUT FÜR ENERGIE-TECHNIK UND THERMODYNAMIK

DISSERTATION

Fatigue Analysis of Prototype Francis Turbines Using Numerical Simulations and Site Measurements

ausgeführt zum Zwecke der Erlangung des akademischen Grades eines
Doktors der technischen Wissenschaften (Dr. techn.)

eingereicht an der TU Wien, Fakultät für Maschinenwesen und Betriebswissenschaften von

Dipl.-Ing. Markus EICHHORN

Mat.Nr.: 0525514

unter der Leitung von

Univ.Prof. Dipl.-Ing. Dr.Ing. Christian BAUER

Institut für Energietechnik und Thermodynamik, E302

begutachtet von

Univ.Prof. Dipl.-Ing. Dr.techn. Manfred KALTENBACHER

Institut für Mechanik und Mechatronik, E325

und

Ao.Univ.Prof. Dipl.-Ing. Dr.techn. Reinhard WILLINGER

Institut für Energietechnik und Thermodynamik, E302

Erklärung

Diese Arbeit wurde von der Österreichischen Forschungsförderungsgesellschaft (FFG) im Rahmen des COMET K-Projektes *GSG-GreenStorageGrid* (Projektnummer 836636) unterstützt.

Ich nehme zur Kenntnis, dass ich zur Drucklegung meiner Arbeit unter der Bezeichnung **Dissertation** nur mit Bewilligung der Prüfungskommission berechtigt bin.

Eidesstattliche Erklärung

Ich erkläre an Eides statt, dass die vorliegende Arbeit nach den anerkannten Grundsätzen für wissenschaftliche Abhandlungen von mir selbstständig erstellt wurde. Alle verwendeten Hilfsmittel, insbesondere die zugrunde gelegte Literatur, sind in dieser Arbeit genannt und aufgelistet. Die aus den Quellen wörtlich entnommenen Stellen, sind als solche kenntlich gemacht.

Das Thema dieser Arbeit wurde von mir bisher weder im In- noch Ausland einer Beurteilerin/einem Beurteiler zur Begutachtung in irgendeiner Form als Prüfungsarbeit vorgelegt. Diese Arbeit stimmt mit der von den Begutachterinnen/Begutachtern beurteilten Arbeit überein.

Wien, 24. Mai 2017

Markus EICHHORN

Vorwort

Ich möchte an dieser Stelle dem Vorstand des Institutes für Energietechnik und Thermodynamik, Herrn Univ.Prof. Dipl.-Ing. Dr.Ing. Christian Bauer für die Betreuung dieser Arbeit danken. Weiterer Dank gilt Herrn Ass.Prof. Dipl.-Ing. Dr.techn. Eduard Doujak für seine Unterstützung während des Forschungsprojektes. Ich möchte mich ebenfalls bei Herrn Univ.Prof. Dipl.-Ing. Dr.techn. Manfred Kaltenbacher und bei Herrn Ao.Univ.Prof. Dipl.-Ing. Dr.techn. Reinhard Willinger für die Begutachtung dieser Arbeit bedanken.

Besonderer Dank gilt den Projektpartnern *Andritz Hydro*, *Verbund Hydro Power*, *ZT Hirtenlehner*, *TIWAG Tiroler Wasserkraft AG* und *Vorarlberger Illwerke AG* für die hervorragende Zusammenarbeit. Ohne ihre Unterstützung wäre ein erfolgreicher Projektverlauf und die Erstellung dieser Arbeit wohl nicht möglich gewesen.

Ganz herzlich möchte ich mich auch bei allen Institutskollegen für die mitunter recht amüsante Zeit während und vor allem abseits der Arbeit bedanken. So manche Feier im ehemaligen Labor bleibt mir mit Sicherheit in guter Erinnerung.

Letztendlich gilt mein größter Dank meiner Familie, die mich während meiner gesamten Ausbildungszeit unterstützt hat und natürlich meiner lieben Kathi, die es immer wieder schafft, dass ich die wirklich wichtigen Dinge im Leben nie aus den Augen verliere.

Markus Eichhorn
im Mai 2017

Abstract

The changing operating conditions for pumped storage plants to balance the electric grid due to the rising amount of volatile wind and solar power causes an increased excitation of the hydraulic machines in part-load. Francis turbines are particularly affected thereby leading to a higher risk of fatigue damages and a reduced lifetime. Dynamic flow phenomena in the best efficiency point like the rotor-stator interaction as well as unsteady pressure fluctuations in off-design conditions like draft tube vortex ropes or interblade vortices are responsible for high structural loads. In order to prevent fatigue cracks and as a consequence expensive failure events, reliable prediction of critical operating points and the associated impact on the runner structure is needed. As site measurements are not feasible in most cases numerical computations have to be used instead.

In the scope of this thesis an approach consisting of fluid-structure interaction simulations is proposed and assessed on a medium and high head prototype Francis turbine. Therefore, unsteady CFD and different kinds of FEM computations are performed with the open-source tools OpenFOAM and Code_Aster. The flow simulations are used to obtain the static and dynamic pressure distributions in different load conditions. The influence of turbulence modeling is further obtained by using the two-equation RANS model $k-\omega$ SST and the hybrid RANS-LES model SST-SAS. The results of the CFD simulations are compared to global parameters and pressure measurements on the according prototype machines.

The computed pressure distributions are applied as boundary conditions for the FEM simulations to evaluate the mechanical response of both runners. Static structural computations are performed in several operating points, ranging from full-load to low-load, using a cyclic sector model to assess the overall load conditions. The dynamic behavior considering the natural mode shapes and eigenfrequencies is obtained by a modal analysis. The impact of the added-mass effect due to the surrounding water volume is evaluated as well. The influence of the rotor-stator interaction on the high head Francis turbine is investigated by a harmonic response analysis. In the critical low-load operating points of both runners transient FEM simulations are performed to evaluate the impact of more stochastic and broadband pressure fluctuations. The influence on the fatigue is assessed by the application of the rainflow cycle counting algorithm to the obtained uniaxial and multiaxial stresses.

The applicability and accuracy of the numerical approach is validated by strain gauge measurements on the according prototype Francis turbines.

Kurzfassung

Die veränderlichen Betriebsbedingungen von Pumpspeicherkraftwerken zur Regelung des elektrischen Netzes aufgrund des steigenden Anteils volatiler Wind- und Solarenergie, verursacht erhöhte Beanspruchungen der hydraulischen Maschinen im Teillastbetrieb. Speziell Francis Turbinen sind davon betroffen, was zu einem höheren Risiko von Ermüdungsschäden und einer geringeren Lebensdauer führt. Dynamische Strömungsphänomene im optimalen Betriebspunkt, wie die Rotor-Stator Interaktion, sowie instationäre Druckschwankungen im Off-Design Betrieb, wie Saugrohrwirbelzöpfe oder Kanalwirbel, sind verantwortlich für diese Beanspruchungen. Um Ermüdungsrisse und damit verbundene Schadensfälle zu vermeiden, ist eine zuverlässige Vorhersage von kritischen Lastbereichen und deren Auswirkung auf das Laufrad notwendig. Da Messungen an den Maschinen in den meisten Fällen nicht durchführbar sind müssen vermehrt numerische Berechnungen herangezogen werden.

Im Zuge dieser Dissertation wird eine Vorgehensweise bestehend aus Fluid-Struktur Interaktionen vorgestellt und anhand einer Mittel- und einer Hochdruck Prototyp Francis Turbine bewertet. Dazu werden instationäre CFD und verschiedene FEM Simulationen mit den Open Source Programmen OpenFOAM und Code_Aster durchgeführt. Die Strömungssimulationen werden zur Berechnung der statischen und dynamischen Druckverteilungen in verschiedenen Betriebsbedingungen verwendet. Der Einfluss der Turbulenzmodellierung wird anhand des Zweigleichungsmodells $k-\omega$ SST und des hybriden RANS-LES Modells SST-SAS evaluiert. Die Ergebnisse der CFD Simulationen werden mit globalen Größen sowie mit Druckmessungen an den entsprechenden Prototypmaschinen verglichen.

Die berechneten Druckverteilungen werden anschließend als Randbedingungen für die FEM Simulationen verwendet, um die mechanischen Belastungen beider Laufräder zu beurteilen. Dabei werden statische Strukturberechnungen in verschiedenen Betriebspunkten, von Vollast bis tiefer Teillast, mittels eines zyklischen Sektormodells durchgeführt. Das dynamische Verhalten bezüglich der Eigenschwingungen und Eigenfrequenzen wird anhand einer Modalanalyse beurteilt. Der Einfluss der umgebenden Wassermassen um das Laufrad wird dabei ebenfalls berücksichtigt und bewertet. Die Auswirkung der Rotor-Stator Interaktion auf das Hochdrucklaufrad wird mittels einer Harmonic Response Analyse berechnet. In den kritischen Teillastbetriebspunkten beider Maschinen werden transiente FEM Simulationen durchgeführt, um den Einfluss stochastischer und breitbandiger Druckschwankungen zu evaluieren. Die Auswirkung auf die Materialermüdung wird durch die Anwendung des Rainflow Cycle Counting Algorithmus unter Berücksichtigung ein- und mehrachsiger Spannungszustände bewertet.

Anwendbarkeit und Genauigkeit der numerischen Simulationen werden anhand von Messungen mittels Dehnmessstreifen an den entsprechenden Prototyp Francis Turbinen validiert.

Contents

1	Introduction	1
1.1	Motivation and Background	1
1.1.1	Transition on the Energy Market	1
1.1.2	Role of Pumped Hydro Energy Storage	2
1.1.3	Impact of Volatile Energy Production on PHES	3
1.2	Literature Review	4
1.3	Research Objective and Scope of the Thesis	6
2	Hydraulic Turbomachines	8
2.1	Classification of Hydraulic Turbomachines	8
2.2	The Francis Turbine	9
2.2.1	Energy Conversion in the Turbine	10
2.2.2	Velocity Triangles	13
2.2.3	Operating Range	14
2.2.4	Unsteady Flow Effects	15
3	CFD in Hydraulic Turbomachines	18
3.1	Introduction of OpenFOAM	18
3.2	Basic Equations of CFD	19
3.3	Finite Volume Discretization	20
3.3.1	Spatial Discretization	21
3.3.2	Interpolation Schemes	22
3.3.3	Temporal Discretization	23
3.3.4	Solving the Navier-Stokes Equations	25
3.4	Simulation of Turbulent Fluid Flow	27
3.4.1	RANS Modeling Approach	28
3.4.2	LES Modeling Approach	30

CONTENTS

3.4.3	Scale-Adaptive Simulation Approach	31
3.4.4	Wall Treatment in Turbulent Flows	32
3.4.5	Boundary Conditions	33
4	FEM in Hydraulic Turbomachines	35
4.1	Introduction of Code_Aster	35
4.2	Basics of the Linear Elasticity Theory	36
4.3	Equation of Motion	37
4.4	Finite Element Discretization	38
4.5	Element and Global Matrix Definitions	39
4.5.1	Element Matrices for the Undamped System	39
4.5.2	Element Matrices Considering Damping	40
4.5.3	Assembly of the Global Matrices	40
4.6	Finite Element Analysis Types	41
4.6.1	Static Analysis	41
4.6.2	Modal Analysis	41
4.6.3	Harmonic Response Analysis	42
4.6.4	Transient Analysis	42
4.7	Fluid-Structure Interaction	43
4.7.1	Bidirectional Coupling	43
4.7.2	Unidirectional Coupling	43
4.7.3	Fluid Added Mass Effect	43
5	Fatigue of Structures	45
5.1	Influences on the Structural Fatigue	45
5.2	Complex Load Histories	47
5.3	Elasto-plastic Behavior	49
5.4	Multiaxial Load Conditions	49
6	Numerical Approach	51
6.1	Paper 1	51
7	Static Structural Investigations	62
7.1	Paper 2	62
8	Dynamic Structural Investigations	73

CONTENTS

8.1	Paper 3	73
9	Fatigue Analysis	84
9.1	Paper 4	84
9.2	Paper 5	95
9.3	Impact on the Structural Damage	104
10	Conclusion and Outlook	107
10.1	Summary of the Thesis	107
10.2	Future Work	109
	Bibliography	110
A	Uncertainty Assessment	118
A.1	Strain Gauge Measurements	118
A.2	Numerical Simulations	119
A.2.1	CFD Simulations	119
A.2.2	FEM Simulations	120
	Curriculum Vitae	124

Nomenclature

Abbreviations

AMI	Arbitrary Mesh Interface
ASM	Algebraic Stress Models
BEP	Best efficiency point
BP	Best-point
CAES	Compressed air energy storage
CDS	Central Difference Scheme
CFD	Computational Fluid Dynamics
CFL	Courant-Friedrichs-Lewy
DES	Detached Eddy Simulation
DNS	Direct Numerical Simulations
DOF	Degree of freedom
EDF	Électricité de France
EVM	Eddy Viscosity Models
FDM	Finite Difference Method
FE	Fatigue endurance
FEA	Finite Element Analysis
FEM	Finite Element Method
FL	Full-load
FOAM	Field Operation and Manipulation
FSI	Fluid-structure interaction
FVM	Finite Volume Method

NOMENCLATURE

GCI	Grid convergence index
GPL	General Public License
HCF	High cycle fatigue
HH	High head
HRA	Harmonic response analysis
LCF	Low cycle fatigue
LES	Large Eddy Simulation
LL	Low-load
MH	Medium head
MPI	Message Passing Interface
PHES	Pumped hydro energy storage
PL	Part-load
PSP	Pumped storage plant
RANS	Reynolds Averaged Navier-Stokes
RSI	Rotor-stator interaction
RSM	Reynolds Stress Models
SAS	Scale Adaptive Simulation
SG	Strain gauge
SGS	Subgrid-scale stress
SNL	Speed-no-load
SST	Shear Stress Transport
SU	Start-up
UDS	Upwind Difference Scheme
URANS	Unsteady Reynolds Averaged Navier-Stokes

Dimensionless Numbers

b	Fatigue strength exponent	[-]
C	Total fatigue damage factor	[-]

NOMENCLATURE

c	Fatigue ductility exponent	[-]
C_r	Reduced fatigue damage factor	[-]
C_μ	Turbulence model constant	[-]
Co	Courant number	[-]
D	Fatigue damage for a certain stress amplitude and load number	[-]
h_n	Normalized mesh size	[-]
K'	Cyclic strength coefficient	[-]
K_s	Stress concentration factor	[-]
n'	Cyclic strain hardening exponent	[-]
r_g	Grid refinement factor	[-]
Re	Reynolds number	[-]
S	Strain coefficient	[-]
u^+	Dimensionless velocity	[-]
y^+	Dimensionless wall distance	[-]

Greek Letters

α	Mass proportional Rayleigh damping coefficient	[-]
α_i	Incidence angle of the absolute velocity component at the optimum	[°]
α'_i	Incidence angle of the absolute velocity component in part load	[°]
α''_i	Incidence angle of the absolute velocity component in full load	[°]
α_w	Limiting function	[-]
α_Φ	Under-relaxation factor	[-]
β	Stiffness proportional Rayleigh damping coefficient	[-]
β_i	Incidence angle of the relative velocity component at the optimum	[°]
β'_i	Incidence angle of the relative velocity component in part load	[°]
β''_i	Incidence angle of the relative velocity component in full load	[°]
β_t	Turbulence model constant	[-]
δ_r	Relaxation factor for the direct time integration method	[-]

NOMENCLATURE

δ_{ij}	Kronecker delta	[-]
ϵ	Mechanical strain	[-]
ϵ'_f	Fatigue ductility coefficient	[-]
ϵ_a	Strain amplitude	[-]
ϵ_n	Normal strain	[-]
$\epsilon_{a,e}$	Strain amplitude due to elastic deformation	[-]
$\epsilon_{a,p}$	Strain amplitude due to plastic deformation	[-]
η	Efficiency	[%]
η_f	Side chamber friction efficiency	[%]
η_h	Hydraulic efficiency	[%]
η_m	Mechanical efficiency	[%]
η_T	Total turbine efficiency	[%]
η_v	Volumetric efficiency	[%]
Γ	Diffusion coefficient	[-]
γ	Shear angle	[-]
γ_e	Equivalent shear strain for multiaxial loads	[-]
γ_r	Relaxation factor for the direct time integration method	[-]
γ_{max}	Shear strain in the maximum shear strain plane	[-]
κ	Von Karman constant	[-]
λ	Linear interpolation factor	[-]
μ	Dynamic viscosity	[Pa s]
μ_t	Turbulent viscosity	[Pa s]
ν	Poisson ratio	[-]
ν_k	Kinematic viscosity	[m ² /s]
ν_p	Plastic Poisson ratio	[-]
ν_t	Eddy viscosity	[m ² /s]
ω	Turbulent dissipation frequency	[s ⁻¹]
ω_a	Angular velocity	[s ⁻¹]

NOMENCLATURE

ω_f	Excitation frequency	$[\text{s}^{-1}]$
ω_i	Angular eigenfrequencies	$[\text{s}^{-1}]$
Φ	Scalar variable	$[-]$
ϕ	Guide vane opening angle	$[\circ]$
ρ	Density	$[\text{kg}/\text{m}^3]$
ρ^n	Remaining iteration term	$[-]$
σ	Mechanical stress	$[\text{N}/\text{m}^2]$
σ'_f	Fatigue strength coefficient	$[-]$
σ_a	Stress amplitude	$[\text{N}/\text{m}^2]$
σ_e	Equivalent von Mises stress	$[\text{N}/\text{m}^2]$
σ_l	Fatigue limit	$[\text{N}/\text{m}^2]$
σ_m	Mean stress	$[\text{N}/\text{m}^2]$
σ_n	Normal stress	$[\text{N}/\text{m}^2]$
σ_T	Thoma cavitation number	$[-]$
σ_u	Ultimate tensile strength	$[\text{N}/\text{m}^2]$
σ_y	Yield strength	$[\text{N}/\text{m}^2]$
σ_{max}	Maximum stress	$[\text{N}/\text{m}^2]$
σ_{min}	Minimum stress	$[\text{N}/\text{m}^2]$
τ_e	Equivalent shear stress for multiaxial loads	$[\text{N}/\text{m}^2]$
τ_w	Wall shear stress	$[\text{N}/\text{m}^2]$
τ_{max}	Shear stress in the maximum shear stress plane	$[\text{N}/\text{m}^2]$
ε	Turbulent dissipation rate	$[\text{m}^2/\text{s}^3]$
φ	Blade angle	$[\circ]$
ξ	Damping ratio	$[-]$

Superscripts

$*$	Loss-free
c	Convective term

NOMENCLATURE

d Diffusive term

Subscripts

1 Runner pressure side

2 Runner suction side

i Index

in Inlet

j Index

m Meridional velocity amount

t Turbulent

u Circumferential velocity amount

w Wall

0 Initial condition

e Finite element

ext Extrapolated value

f Fluid

fs Fluid-structure

n Time step

opt Optimum operating point

s Structure

Tensors, Vectors, Matrices

ϵ Strain vector

ϕ_i Eigenvectors

ϕ Amplitude vector

σ Stress vector

$\ddot{\mathbf{U}}$ Global acceleration vector

$\dot{\mathbf{U}}$ Global velocity vector

$\mathbf{c}_{1,2}$ Absolute velocity vector at the runner inlet and outlet

NOMENCLATURE

\mathbf{C}	Damping matrix
\mathbf{D}	Strain-displacement matrix
\mathbf{d}	Differential operator matrix
\mathbf{E}	Elasticity matrix
\mathbf{F}_e	Force vector of all nodes of a finite element
\mathbf{f}_e	Field force vector of all nodes of a finite element
\mathbf{K}	Stiffness matrix
\mathbf{L}	Load vector
\mathbf{M}	Mass matrix
\mathbf{N}	Shape function matrix
\mathbf{n}	Normal face vector
\mathbf{O}	Assembly operator
\mathbf{p}_e	Surface load vector of all nodes of a finite element
\mathbf{P}	Pressure vector
\mathbf{u}_i^e	Displacement vector of the i^{th} node of a finite element
\mathbf{u}^e	Displacement vector of a point of a finite element
\mathbf{U}_e	Displacement vector of all nodes of a finite element
$\mathbf{u}_{1,2}$	Circumferential velocity vector at the runner inlet and outlet
\mathbf{U}	Global displacement vector
\mathbf{u}	Displacement vector
$\mathbf{w}_{1,2}$	Relative velocity vector at the runner inlet and outlet
τ_{ij}	Viscous stress tensor
τ_{ij}^S	Subgrid-scale stress tensor
A	Coefficient matrix
Q	Vector for the volume integrals
q_Φ	Source or sink term
S_{12}	Strain-rate tensor

NOMENCLATURE

T_{ij} Total stress tensor

Variables

\ddot{u}	Acceleration of a structure	[m/s ²]
\dot{m}	Mass flow rate	[m ³ /s]
\dot{u}	Velocity of a structure	[m/s]
A	Area	[m ²]
a	Fluid sound of speed	[m/s]
c_i	Absolute velocity components	[m/s]
$c_{1,2}$	Absolute velocity at the runner inlet and outlet at the optimum	[m/s]
$c'_{1,2}$	Absolute velocity at the runner inlet and outlet in part load	[m/s]
$c''_{1,2}$	Absolute velocity at the runner inlet and outlet in full load	[m/s]
D	Diameter	[m]
d	Pipe diameter	[m]
E	Young's modulus	[N/m ²]
E_m	Measurement error	[%]
e_{ext}	Relative error compared to the extrapolated value	[%]
e_{it}	Iteration error	[-]
f	Eigenfrequencies	[Hz]
F_e	Surface integral in the point e	[-]
F_i	Punctual forces on a solid body	[N]
f_i	Field forces on a solid body	[N/m ³]
F_n	Blending functions for the SST model	[-]
f_0	Runner rotational frequency	[Hz]
f_{BP}	Blade passing frequency	[Hz]
F_{LES}	Spatial LES filter	[-]
G	Shear modulus	[N/m ²]
g	Gravitational constant	[m/s ²]

NOMENCLATURE

H	Head	[m]
I	Turbulence intensity	[-]
k	Turbulent kinetic energy	[m ² /s ²]
L	Expected lifetime	[years]
l_m	Turbulent mixing length	[m]
L_{vK}	Von Karman length scale	[m]
M	Angular momentum	[Nm]
N	Number of load cycles	[-]
n	Rotational speed	[min ⁻¹]
N_c	Number of cells	[-]
N_f	Elasto-plastic fatigue life	[-]
n_i	Load cycles at a certain stress amplitude	[-]
n_n	Number of nodes	[-]
n_q	Specific speed	[min ⁻¹]
n_{11}	Unit speed	[min ⁻¹]
P	Power	[W]
p	Static pressure	[Pa]
P_h	Hydraulic power	[W]
p_i	Surface loads on a solid body	[N/m ²]
P_m	Mechanical power	[W]
p_t	Total pressure	[Pa]
Q	Discharge	[m ³ /s]
Q_P	Volume integral in the cell P	[-]
Q_{11}	Unit discharge	[m ³ /s]
Q_{SAS}	Additional source term in the SST-SAS turbulence model	[-]
R	Ratio between the minimum and maximum mechanical stress	[-]
r	Radius	[m]
s	Slope of the S-N curve above the fatigue limit	[-]

NOMENCLATURE

s^*	Slope of the S-N curve below the fatigue limit	[-]
s_e^*	Slope of the S-N curve for the elementary Miner rule	[-]
s_m^*	Slope of the S-N curve for the modified Miner rule	[-]
s_o^*	Slope of the S-N curve for the original Miner rule	[-]
t	Time	[s]
T_m	Turbine torque	[Nm]
u	Mechanical displacement	[m]
U_E	Elastic energy	[J]
$u_{1,2}$	Circumferential velocity at the runner inlet and outlet at the optimum	[m/s]
$u'_{1,2}$	Circumferential velocity at the runner inlet and outlet in part load	[m/s]
$u''_{1,2}$	Circumferential velocity at the runner inlet and outlet in full load	[m/s]
u_τ	Friction velocity	[m/s]
V	Volume	[m ³]
V_E	Total potential energy	[J]
W_E	Potential energy of external forces	[J]
$w_{1,2}$	Relative velocity at the runner inlet and outlet at the optimum	[m/s]
$w'_{1,2}$	Relative velocity at the runner inlet and outlet in part load	[m/s]
$w''_{1,2}$	Relative velocity at the runner inlet and outlet in full load	[m/s]
x_i	i^{th} Cartesian coordinate	[m]
Y	Specific turbine energy	[J/kg]
Y_a	Specific turbine energy in the absolute frame of reference	[J/kg]
Y_a^*	Loss-free specific turbine energy in the absolute frame of reference	[J/kg]
Y_h	Specific hydraulic energy losses	[J/kg]
Y_r	Specific turbine energy in the rotating frame of reference	[J/kg]
Y_r^*	Loss-free specific turbine energy in the rotating frame of reference	[J/kg]
z	Geodetic height	[m]
z_g	Number of guide vane blades	[-]

Chapter 1

Introduction

1.1 Motivation and Background

1.1.1 Transition on the Energy Market

The worldwide efforts to reduce greenhouse gas emissions have changed the energy policy significantly in the last few decades, especially in the industrial countries. The total gross electric energy production in the 28 member countries of the European Union (EU-28) has increased from about 2.5 million GWh in 1990 to more than 3 million GWh in 2014 (see Figure 1.1) . Although the largest amount is still produced by the combustion of coal, oil and gas or by nuclear power plants, the significance of renewable energy sources is growing rapidly.

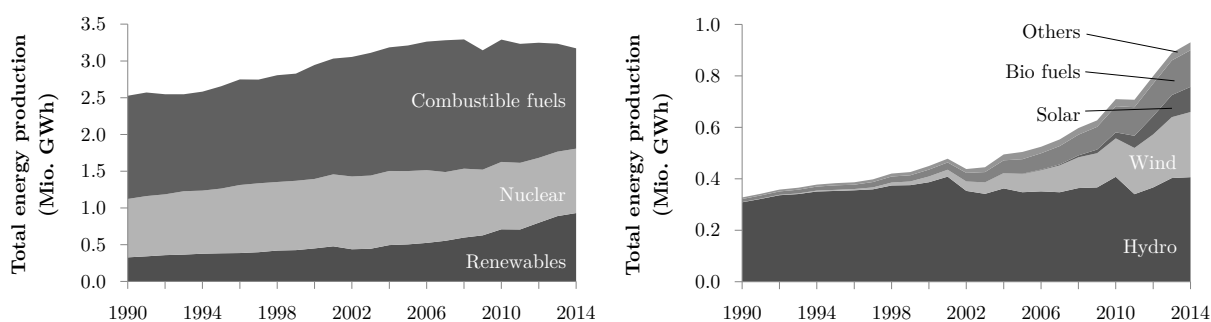


Figure 1.1: Total gross electric energy production in EU-28 (left) and share of renewables (right) from 1990 to 2014 (data from Eurostat [24]).

In 2008, the European Union agreed on the 2020 Climate and Energy Package, which defines three important climate and energy targets for the year 2020:

- 20 % cut in greenhouse gas emissions (from 1990 levels)
- 20 % of EU energy from renewables
- 20 % improvement in energy efficiency

This agreement caused a rising investment in new renewable energy technologies like wind, solar, geothermal, tidal and bio fuel sources. In 2014 the share of renewables on the total electric energy production was nearly one million GWh or 30 %. Whereas the amount of solar and wind power systems is especially rising rapidly, the role of hydropower plants encompassing nearly 44 % of the 2014 market is still significant (see Fig. 1.2 left). In order to fulfill the ambitious plans of the European Union to keep climate change below 2°C and to reduce greenhouse gas emissions by 80 % in 2050 compared to 1990 (see European Commission [23]), the amount of renewables has to be increased continuously. One problem, which arises thereof, is the volatility of wind and solar power systems due to the strong dependence on meteorological conditions (see Fig. 1.2 right). To keep the electric power grid in balance, the demand and the generated power must correspond at every moment in time. The feed-in of the new renewables causes higher fluctuations in the load curve, leading to an energy surplus in times of low demand and to a deficit in times of high demand. To compensate these oscillations, conventional power sources like thermal or hydropower plants have to be throttled or started-up, as described by Leonard et al [55]. The occurring large energy gradients of wind and solar power require faster response times to compensate for those load variations. This issue will be of major importance for the forthcoming decades.

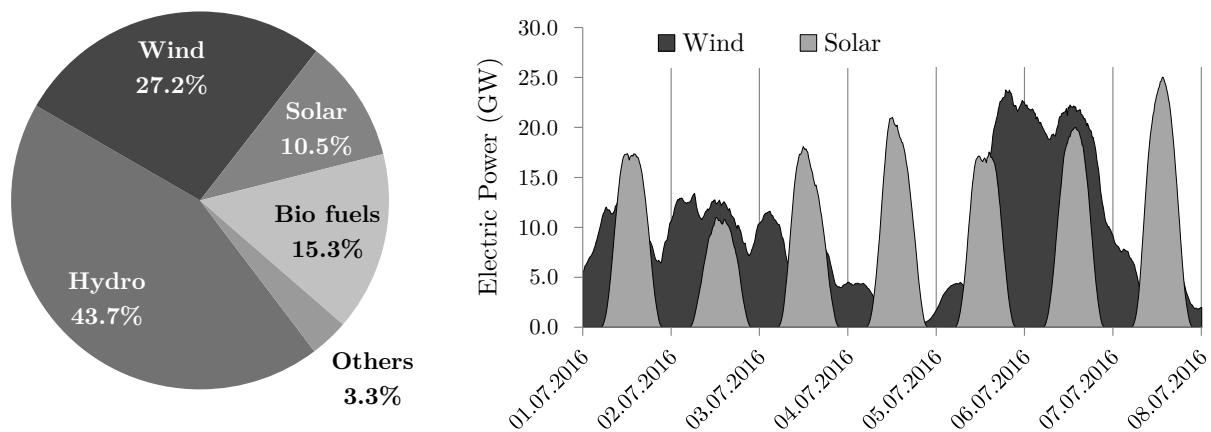


Figure 1.2: Left: Share of renewables in EU-28 in 2014 (data from Eurostat [24]). Right: Electric energy generation by wind and solar power in Germany for July 2016 (data from ENTSO-E [21]).

1.1.2 Role of Pumped Hydro Energy Storage

The most competitive and mature technology for grid control even in large-scales are pumped hydro energy storage (PHES) power plants (see Guittet et al. [38]). Although other systems like compressed-air energy storage (CAES), chemical storage or battery solutions will become more advanced in the future (see Teller et al [91]), PHES combines a couple of advantages: Fast response times (seconds to minutes), large storage capacities, high round-cycle efficiencies (70 to 80 %, up to 87 %), low operation and maintenance costs, 'black-start' capability (to restart the electric grid after a blackout) and long asset life (50 - 100 years), as described by Rehman et al. [82] and Zach et al. [107]. PHES power

plants are converting the potential energy of water into mechanical energy to provide power to the electric grid or to store an energy surplus by the conversion of mechanical energy into potential energy. The first case is known as turbine operation mode. Therefore, the stored water volume in the headwater reservoir flows through the turbine into the tailwater reservoir. The mechanical torque at the runner shaft is transformed by the generator to electric power (see Figure 1.3). In the other case, the pump operation mode, the water in the tailwater basin is pumped in the reverse direction up to the headwater reservoir by obtaining electric power from the grid.

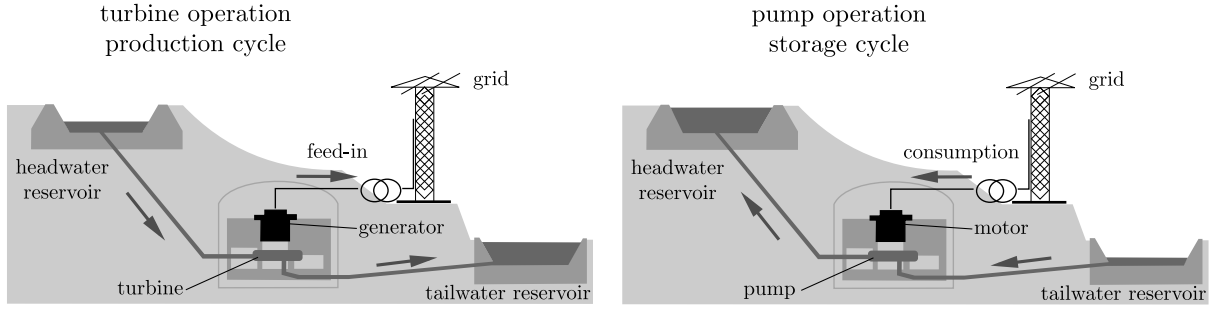


Figure 1.3: Scheme of pumped hydro energy storage technology in turbine operation (left) and pump operation (right). Graphics from Unterberger [97].

For the hydraulic machinery of a pumped storage power plant two assemblies exist with different advantages and disadvantages. First, a ternary set can be used consisting of a turbine, a pump and the motor-generator. The pump and the turbine are therefore usually coupled by a hydraulic torque converter. The advantages of this assembly are higher efficiencies, faster response and start-stop times, increased operating flexibility and the possibility of hydraulic short circuit operation. The disadvantages are mainly higher investment costs and the requirement of larger construction space. The second possible assembly consists of a reversible pump-turbine and a motor-generator. To switch between both operation modes the rotational direction has to be reversed, which leads to increased response times. Although the efficiency of a pump-turbine is lower compared to a ternary set (especially in turbine operation), the economical advantage can be beneficial in some cases.

The world-wide installed capacity of PHES in 2014 was more than 150 GW including approximately 400 power plants with more than 100 MW output power (see Guittet et al. [38]). The countries with the most installed pumped storage power (PSP) capacities are Japan (26.7 GW), China (24.8 GW) and the USA (22.8 GW). All European countries together have a total installed PHES capacity of about 48 GW, with the highest concentrations in Italy (7.2 GW), Germany (6.7 GW), Spain (6.5 GW) and France (5.2 GW). Although PSP represents only 2.5 % of the worldwide power generation, it has an amount of nearly 99 % on the global electricity storage capacity, according to Zach et al. [107].

1.1.3 Impact of Volatile Energy Production on PHES

PHES power plants are still the best option for longtime energy storage due to high capacities and also to balance the load curve of the electric grid. However, the high gradients

of wind and solar energy generation require more flexibility of existing and newly designed hydraulic machinery to stay competitive on the energy market. An example of the fast transition between operating modes of PHES power plants in Germany is displayed in Fig. 1.4 (left). As a result, the number of transient load conditions of the hydraulic machines are increasing significantly (e.g. start-stop cycles and load variations) as well as the operating amount in steady off-design points like part-load, low-load or speed-no-load regime. As the fluid flow in transient and off-design conditions does not coincide with the runner geometry, dynamic and unsteady effects occur in the hydraulic machine, affecting the structural response of its components (see Dörfler et al. [16]). Especially Francis turbines are influenced thereby, as reported by Trivedi et al. [95, 96]. An example of measured stresses on a medium head prototype Francis runner from start-up to full-load operation is displayed in Fig. 1.4 (right). Advanced manufacturing technologies and the efforts to maximize the hydraulic efficiency at reduced costs result in thinner and sophisticated blade geometries with more lightweight structures. In consequence, higher stress amplitudes and stress concentration may occur leading to fatigue cracks and further damages. Different examples have been reported by Egusquiza et al. [20], Frunzăverde et al. [28] or Dorji and Ghomashchi [17]. To prevent such failure and therefore high maintenance costs, reliable fatigue assessment of existing and newly designed runners are needed.

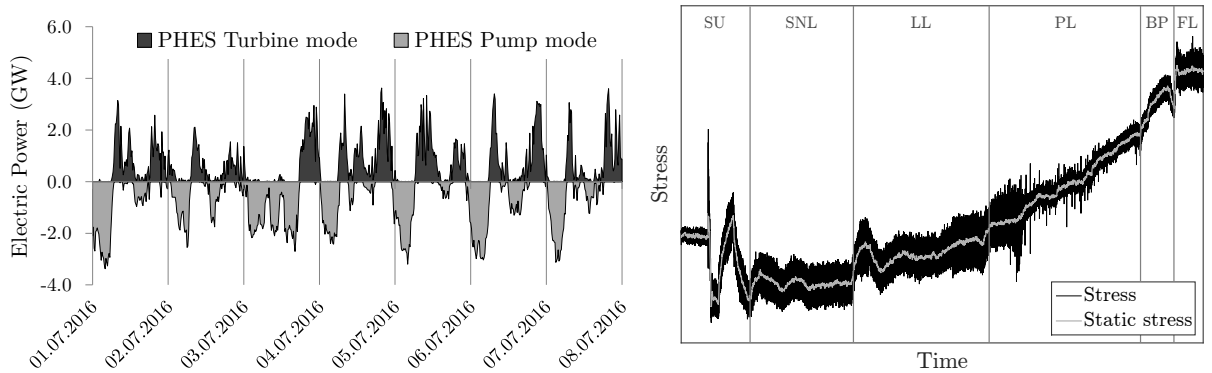


Figure 1.4: Left: Power generation and consumption by PHES in Germany for July 2016 (data from ENTSO-E [21]). Right: Measured stresses on a Francis runner during start-up (SU), speed-no-load (SNL), low-load (LL), part-load (PL), best-point (BP) and full-load (FL) operation.

1.2 Literature Review

Strain gauge measurements on a model or even prototype runner of hydraulic power plants, as previously shown, can give detailed results about the static and dynamic excitations of the structure. They are especially useful to obtain the impact of the flexible operation of hydropower plants in transient and off-design conditions, as described by Coutu and Chamberland-Lauzon [13]. Gagnon et al. [29] used strain gauge data for different start-up schemes to investigate the influence on the runner life expectancy. Löfflad et al. [60] gives a detailed description of the equipment and procedure using strain gauge measurements

at various hydraulic turbines. Coutu et al. [14] carried out prototype measurements on an old and a new high head Francis turbine in the course of runner replacement due to fatigue cracking. The advantage of strain gauge measurements are detailed results of appearing stresses under realistic load conditions, which can be used for a fatigue analysis and to determine critical operating conditions, as described by Löfflad and Eissner [59] and Monette et al. [70]. The disadvantages are high efforts and costs (especially for prototype machines) and a limited number of applicable sensors and therefore observable locations of the structure. Hence, high-stressed areas must be evaluated in advance using Finite Element Analysis (FEA) for a correct sensor application (see Löfflad et al. [60]). In the design phase of new hydraulic runners prototype measurements are usually not available. Although model tests can be conducted, uncertainties for the stress transfer from model to prototype machine remain. Further, long-term measurements, to gain enough data for reliable fatigue evaluation, are not available in most cases and therefore extrapolation methods have to be used like the extreme value theory proposed by Johannesson [47]. Gagnon et al. [31] investigated further approaches to extrapolate the strain response of a single recorded occurrence on a Francis runner during start-up procedures.

In case of fatigue damages a failure analysis has to be performed probably without any available measurement data. Metallurgic analysis can help to identify the influence of fatigue as discussed by Frunzäverde et al. [28] but cannot reveal the root cause of such damages. Recent advances in the field of fluid-structure interactions (FSI) allow more detailed investigations to obtain the origin of dynamic excitations and to improve existing or new runner structures (see Egusquiza et al. [20]). A current review of different studies and main topics considering FSI for hydraulic turbines has been summarized by Trivedi and Cervantes [93]. The developments of numerical flow computations in the last decades increased the possibilities and the accuracy of predicting the pressure fluctuations induced by unsteady phenomena like the rotor-stator interaction (RSI), draft tube vortex ropes or vortex shedding in hydraulic turbomachines as discussed by Keck and Sick [48] or Sick et al. [88]. Measurements and CFD simulations by Magnoli and Maiwald [62] and Trivedi et al. [94] proved the applicability of numerical flow simulations. Nennemann et al. [74] investigated the influence of turbulence modeling on the dynamic pressure fluctuations and also stress response in speed-no-load operation. Compared to the two-equation $k-\varepsilon$ model the hybrid RANS-LES model SAS (Scale Adaptive Simulation) revealed much better results, especially in the low frequency range. Seidel et al. [87] performed similar investigations with comparisons between URANS and LES simulations.

Many studies deal with the usage of commercial software for CFD computations but according to the advances of OpenFOAM (**O**pen **S**ource **F**ield **O**peration and **M**anipulation) in recent years, several studies have been published considering the application of the open-source code for hydraulic turbomachines: Page et al. [77] investigated the steady-state capabilities of OpenFOAM for a Francis turbine. Lenarcic et al. [54] and Lenarcic and Bauer [53] compared the numerical results of steady and unsteady operating conditions of the Francis99 machine using the FOAM-extend version with a commercial software and different turbulence models. Erne [22] performed CFD simulations with OpenFOAM on a pump-turbine using an extended $k-\omega$ SST turbulence model with the implementation of the streamline curvature correction.

For the assessment of a hydraulic runner structure the knowledge of the natural frequencies and mode shapes is significant to avoid any appearing resonance problems during operation.

Hence, the modal analysis including the added mass effect of the surrounding water volume of the runner has become a useful tool. Different investigations using measurements and FEM simulations on model and prototype runners have been performed by Coutu et al. [15], Flores et al. [27], Liang et al. [56] and Valentín et al. [98, 99]. Although the approach using acoustic elements to model the surrounding water volume includes some simplifications, as later discussed, the numerical studies reveal more precise results for the eigenmodes compared to neglecting the added mass.

The main impact for the structural excitation of especially high head machines is the rotor-stator interaction between the static guide vanes and the rotating runner blades. To obtain the influence of the RSI on the dynamic behavior, harmonic response simulations are a common approach in industrial design processes. Several investigations have been published by Huang et al. [43], Hübner et al. [44], Liang et al. [57] and Seidel et al. [86], proving the applicability of this approach.

In addition to structural excitations affected by harmonic phenomena, stochastic or dynamic effects without a particular frequency may appear, which cannot be examined using a harmonic analysis. Extended approaches using quasi-static FEM simulations, which neglect the inertial effects of a dynamic motion, show good agreements compared to strain gauge measurements, as discussed by Duparchy et al. [18] and Weber et al. [104]. On the other hand, time-dependent FEM simulations can deliver more detailed and accurate results, although the computational effort is higher (see Morissette et al. [72]).

For the reliable assessment of the runner lifetime, further influences like crack growth have to be considered by the Linear Elastic Fracture Mechanics theory, as discussed by Gagnon et al. [30, 32], Thibault et al. [92] and Huth [45]. Therefore, data from strain gauge measurements or obtained by numerical simulations can be used.

1.3 Research Objective and Scope of the Thesis

The future challenge for the manufacturers and also the operators of pumped storage power plants will be the accurate prediction of fatigue for the hydraulic components, especially the runner, to cope with the recent requirements of the energy market. Therefore, profound investigations will be necessary even in the design phase of new power plants or in the course of the refurbishment processes. As measurement data is not available in many cases the reliability of numerical computations becomes more important. One state of the art approach, which is usually used during the design process of Francis runners, is the application of static FEM simulations to assess the static stresses on the structure (see Fig. 1.5). Steady CFD computations are usually performed to obtain the pressure field in the machine, which is used as boundary condition for the FEM simulations. Another approach, which has been developed in recent years, is the application of harmonic response FEM computations to evaluate appearing dynamic stress amplitudes. This method is useful if the runner structure is excited at a significant frequency induced for example by the rotor-stator interaction. In cases of more stochastic pressure fluctuations appearing in low-load operation of Francis turbines, this procedure is not sufficient. Therefore, an advanced numerical approach consisting of unsteady CFD and transient FEM simulations is proposed, which is not state of the art for industrial design processes (see Fig. 1.5). In the scope of this thesis the applicability and accuracy of this method is obtained on a

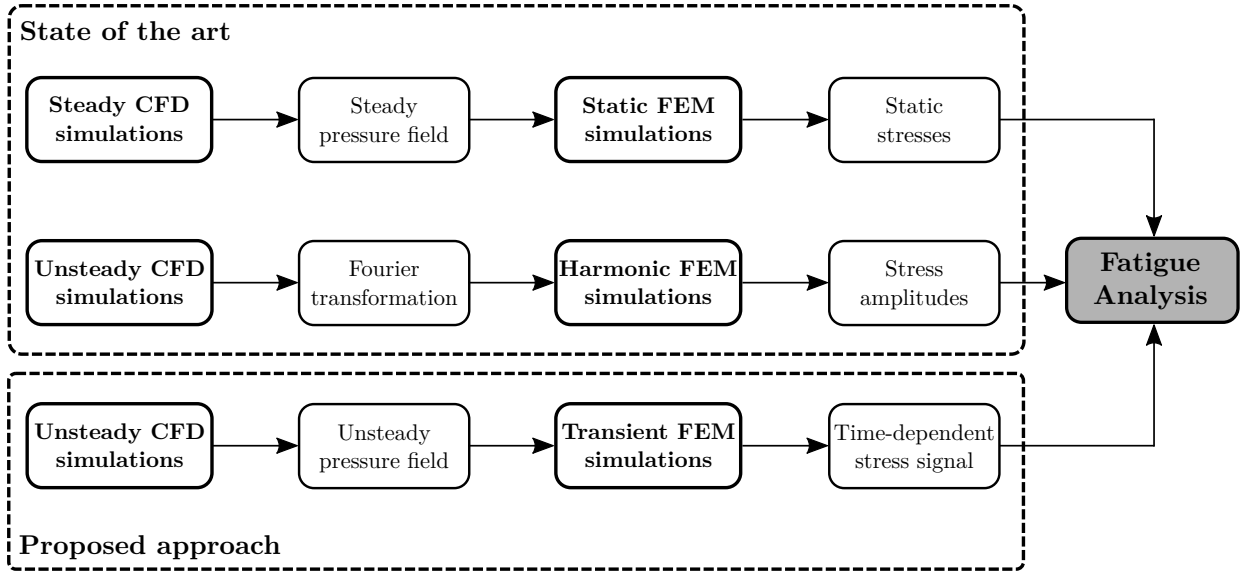


Figure 1.5: Numerical approach for the fatigue analysis of Francis turbines - state of the art and proposed approach.

high and a medium head prototype Francis turbine to examine the impact of stochastic pressure fluctuations in low-load conditions on the runner response and on the fatigue. The results of the numerical simulations are compared with measurements on the according prototype machines, which have been performed in the course of a large research project. Thereby, strain gauges have been applied to the Francis runners to obtain the static and dynamic stresses in steady and transient operating conditions. Further, pressure measurements should give a more detailed insight on the flow behavior.

Due to continuously increasing costs for commercial CFD and FEM tools, the main emphasis of this work lies on the application of open-source codes. Hence, the flow simulations are performed with OpenFOAM and the structural investigations are done with Code_Aster. Static and also harmonic FEM computations will be considered as well in this thesis, but the main objective is the implementation and validation of the transient FEM simulations for the usage in future industrial design processes.

Chapter 2

Hydraulic Turbomachines

2.1 Classification of Hydraulic Turbomachines

Hydraulic turbomachines are used to convert the hydraulic energy of a flowing fluid - usually water - into mechanical and electric energy by turbines or in the reverse direction by pumps. The field of the hydraulic turbines can be mainly classified according to DIN 4320 by the aspect of the operation mode into impulse turbines (Pelton and Ossberger turbines) and reaction turbines (Francis and Kaplan turbines) as displayed in Fig. 2.1. Regarding impulse turbines the pressure energy is converted into kinetic energy by a nozzle and the impulse of the resulting jet is converted into mechanical energy by the runner. In contrast, the runner of a reaction turbine is surrounded entirely by water and additionally to the kinetic energy the pressure difference between the runner inlet and outlet is converted into mechanical energy.

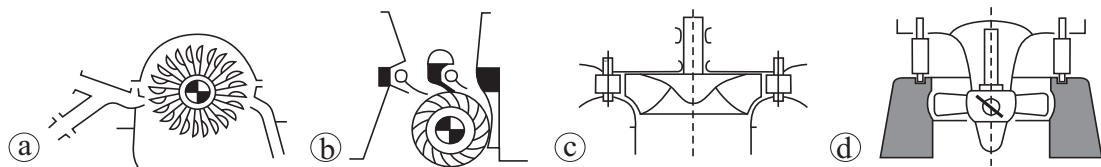


Figure 2.1: Common types of hydraulic turbines: a) Pelton turbine; b) Ossberger turbine; c) Francis turbine; d) Kaplan turbine. Graphics from Giesecke and Mosonyi [34].

In addition to the distinction by the operation mode, hydraulic turbines can be further classified by:

- the shaft direction (vertical or horizontal),
- the water intake type (spiral casing, duct, nozzle),
- the control mode (single or double regulation),
- the topographic conditions (head H and discharge Q).

For usual hydropower plants (except small hydro concepts) mainly three different turbine types are used: The Pelton turbine for a large head (up to 2000 m) and small discharge. The Kaplan turbine, which is mostly used in run of river plants for small head and large discharge. And the Francis turbine used for a wide range of head and discharge between the before mentioned types. A characteristic number to classify the different turbine types is the specific speed n_q defined by

$$n_q = n \frac{\sqrt{Q}}{H^{0.75}} \quad (2.1)$$

depending on the rotational speed n , the head H and the discharge Q . In Fig. 2.2 the operating ranges of the main turbine types are displayed considering the specific speed and the head. The Pelton turbine is therefore located at the lower end of the specific speed up to $n_q \approx 30 \text{ min}^{-1}$. The Francis turbines are located at a range of $20 \text{ min}^{-1} \leq n_q \leq 120 \text{ min}^{-1}$. The Kaplan turbines are located above the Francis turbines with the highest specific speeds.

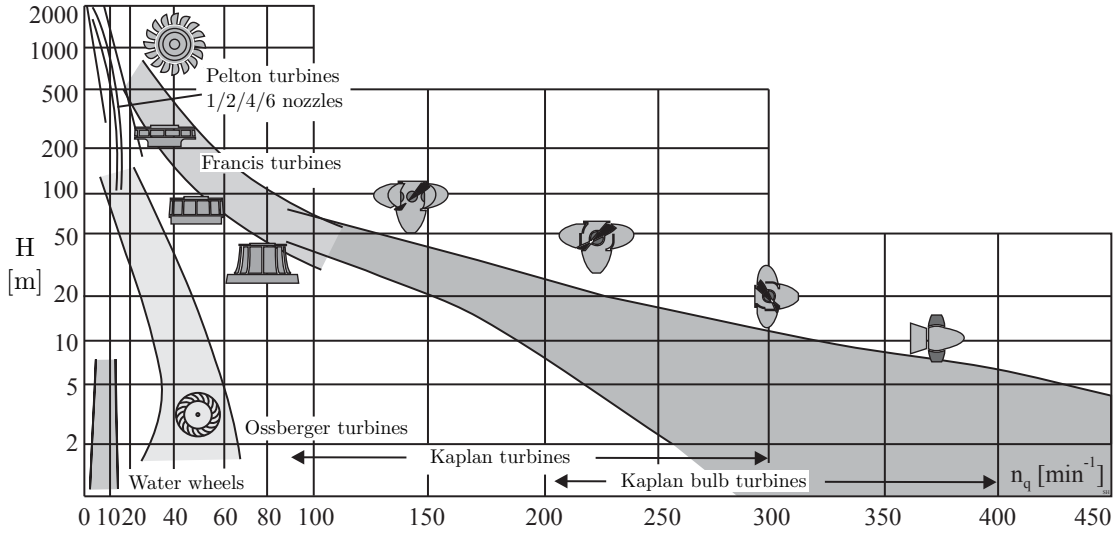


Figure 2.2: Classification of hydraulic turbines depending on the specific speed n_q and the head H . Graphics adapted from Giesecke and Mosonyi [34].

2.2 The Francis Turbine

The most common turbine type is the Francis turbine, which is used for a head range between 50 m and up to 700 m and a power range of more than 800 MW. It is the turbine type with the highest hydraulic efficiency of more than 96 % (see Bauer [4]). Depending on the specific speed the runner geometries vary from a more radial shape with narrow blade channels (high head runner) to more axial shapes with large blade channels (medium and low head runners), as displayed in Fig. 2.3. Francis turbines are mostly constructed with a vertical shaft to achieve a more uniform flow behavior inside the runner. Horizontal designs are only used for low pressure machines. The runner consists of several blades, which are

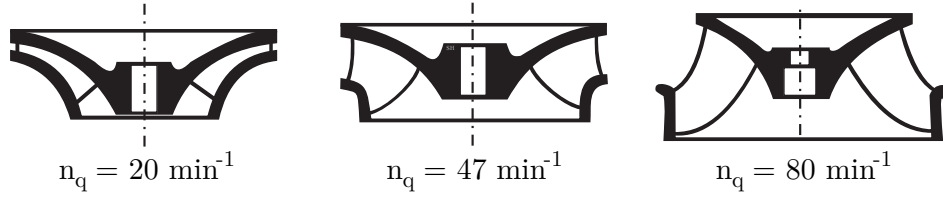


Figure 2.3: Different types of Francis turbines depending on the specific speed n_q . Graphics adapted from Giesecke and Mosonyi [34].

rigidly coupled to the shroud on the bottom side and to the hub on the top. The water flows in the radial direction into the turbine inlet and leaves the outlet in the axial direction at the suction side of the runner. The appearing torque is converted to electric energy by the generator, which is coupled by the shaft with the runner hub (see Fig. 2.4). The headwater is distributed to the turbine by the spiral casing, the stay vanes and the adjustable guide vane blades, which are used to control the operating conditions and the output power of the hydraulic machine. At the suction side of the runner the water flows through the usually bended elbow draft tube to the tailwater. The deceleration of the water in the draft tube cone is used to increase the turbine efficiency.

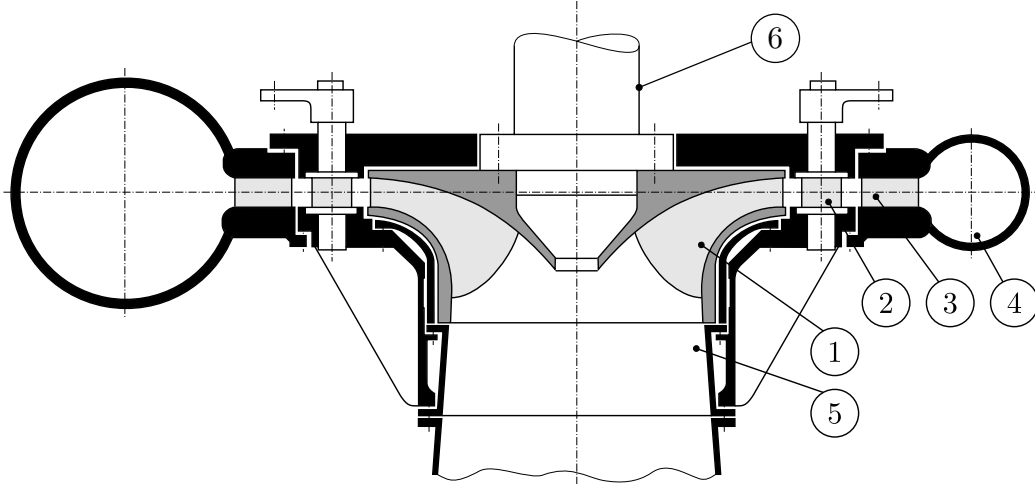


Figure 2.4: Francis turbine components: 1) runner, 2) guide vanes, 3) stay vanes, 4) spiral casing, 5) draft tube, 6) shaft. Graphics adapted from Wachauer [101], based on Raabe [80].

2.2.1 Energy Conversion in the Turbine

According to the theorem of Bernoulli for an incompressible fluid with a constant density ρ the specific energy along a streamline without any energy gradient remains constant. Applied on a fluid particle flowing through the blade channel of a turbine runner (see Fig. 2.5) the loss-free specific energy in an absolute frame of reference Y_a^* can be defined by

$$Y_a^* = \frac{p_1 - p_2}{\rho} + \frac{c_1^2 - c_2^2}{2} + (z_1 - z_2)g. \quad (2.2)$$

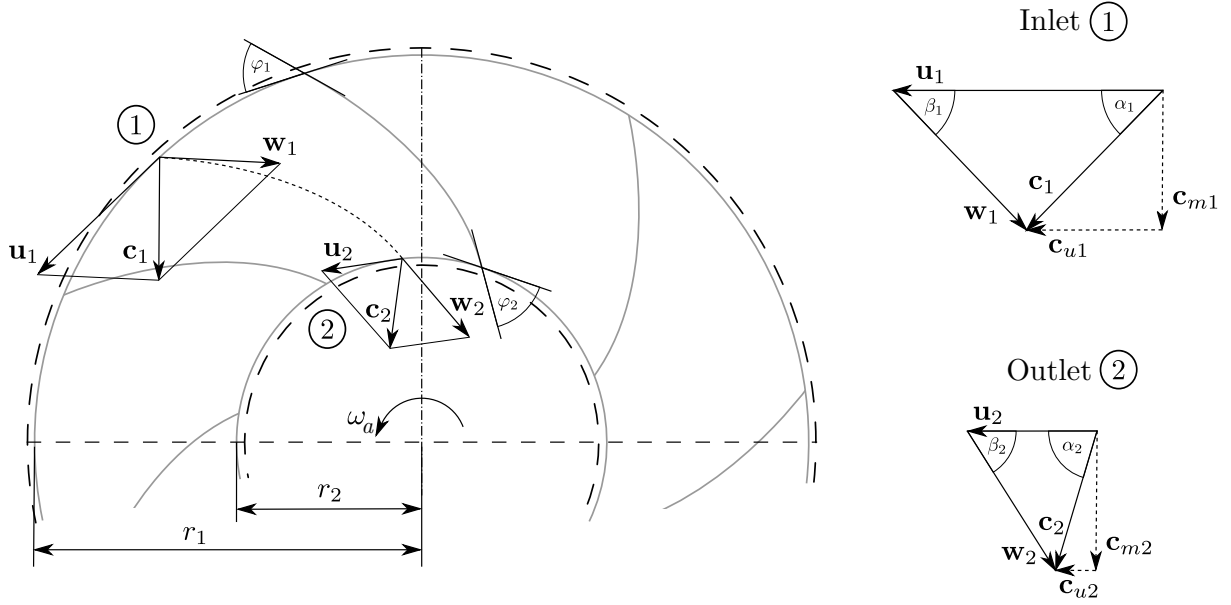


Figure 2.5: Fluid flow through a radial turbine with the according velocity triangles. Graphics adapted from Wachauer [101].

The fluid enters the turbine at the pressure side (radius r_1) with the static pressure p_1 , the absolute velocity c_1 and the geodetic height z_1 and leaves the runner at the suction side (radius r_2) with the static pressure p_2 , the velocity c_2 and the geodetic height z_2 . With the definition of the total pressure $p_t = p + c^2 \rho / 2$ and the correlation $H = Y/g$ the total pressure difference can also be expressed by the water net head

$$H = \frac{\Delta p_t}{\rho g} + \Delta z \quad (2.3)$$

For the energy conversion in hydraulic turbines the angular momentum generated by the flowing water through the blade chambers in the runner is relevant. Based on the fluid dynamics momentum equation with the discharge through the turbine Q and the assumption of a constant fluid density ρ the angular momentum M transferred from the fluid to the runner can be expressed by the equation of Euler

$$M = \rho Q (r_1 c_1 \cos \alpha_1 - r_2 c_2 \cos \alpha_2) \quad (2.4)$$

with the incidence angles $\alpha_{1,2}$ of the absolute velocities at the inlet and outlet. The available hydraulic power P_h can be expressed in the rotating frame of reference with the angular velocity $\omega_a = u/r$ and the correlation $P_h = M \omega_a$ by

$$P_h = \rho Q (u_1 c_1 \cos \alpha_1 - u_2 c_2 \cos \alpha_2) = \rho Q (u_1 c_{u1} - u_2 c_{u2}). \quad (2.5)$$

The maximum power can be therefore assumed for the case when the circumferential amount of the absolute velocity at the turbine outlet becomes zero ($c_{u2} = 0$). For the best efficiency point (BEP) the flow at the turbine outlet must be therefore free of rotation. The hydraulic

power can also be defined using the loss-free specific energy in the rotating frame of reference $Y_r^* = u_1 c_{u1} - u_2 c_{u2}$ by

$$P_h = \rho Q Y_r^* = \rho Q g H. \quad (2.6)$$

Due to the specific energy losses induced by the friction and turbulence inside the blade channels Y_h (hydraulic losses) the available specific energy results in $Y_r = Y_r^* - Y_h$. The hydraulic efficiency can be expressed by

$$\eta_h = \frac{Y_r}{Y_r^*} = \frac{Y_r^* - Y_h}{Y_r^*} \quad (2.7)$$

or by the available mechanical turbine power at the shaft P_m , the hydraulic power P_h and the turbine torque T_m

$$\eta_h = \frac{P_m}{P_h} = \frac{T_m \omega_a}{\rho Q g H}. \quad (2.8)$$

The total efficiency of the hydraulic turbine η_T results from further influences besides the hydraulic losses like the volumetric efficiency η_v due to gap leakage flows, the friction efficiency in the runner side chambers η_f or the mechanical efficiency due to the friction in bearings and seals η_m (see Fig. 2.6):

$$\eta_T = \eta_h \cdot \eta_v \cdot \eta_f \cdot \eta_m \quad (2.9)$$

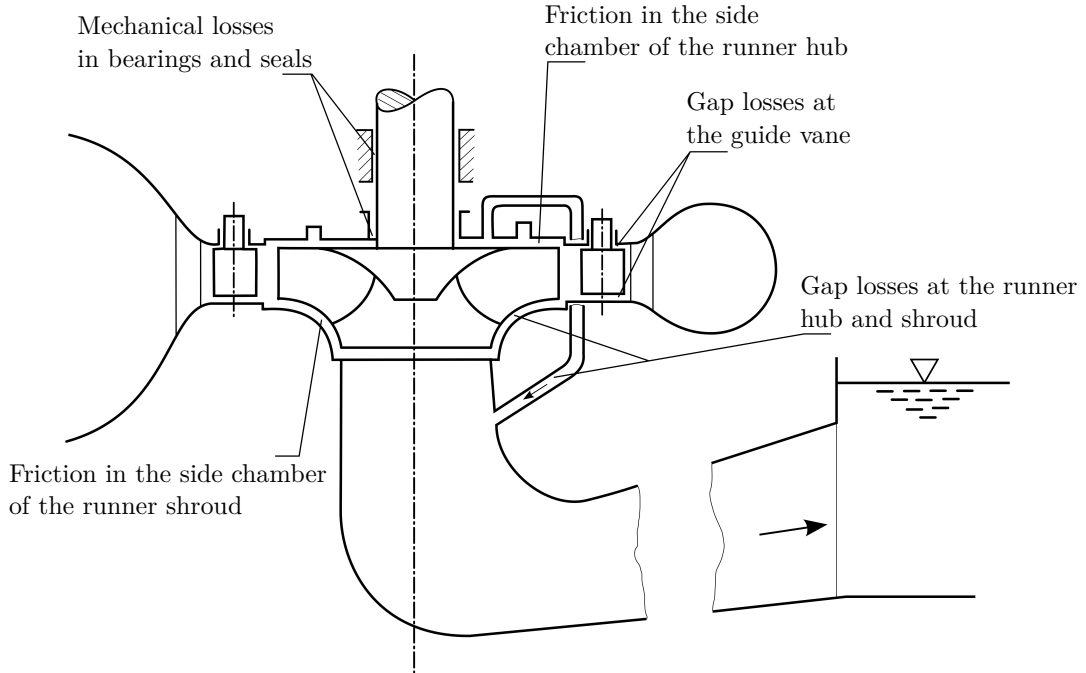


Figure 2.6: Losses in a Francis turbine. Graphics adapted from Bauer [4].

For CFD simulations only the hydraulic losses are considered as gaps, bearing and seals are usually not included in the simplified numerical models. The boundaries are in most cases at the spiral casing inlet and at the draft tube outlet, so the hydraulic losses of each component are considered.

2.2.2 Velocity Triangles

As shown in the previous section, the operating point and the flow conditions of a Francis turbine can be described by the velocity components at the inlet and outlet of the runner blades. Whereas the rotational velocity of the runner is resulting from the radius and the angular velocity to $u = r\omega_a$ the vectors for the absolute and relative velocity \mathbf{c} and \mathbf{w} are resulting from the angles α and β in the absolute and rotating frame of reference. According to Eq. 2.6 the desired output power is attained at a given head H by varying the discharge through the runner Q . For Francis turbines this is realized by the adjustable guide vane blades in front of the runner (see Fig. 2.7).

The vector of the absolute velocity \mathbf{c}_1 can be derived with the angle α_1 and the correlation between the discharge and the meridional component of the absolute velocity

$$c_{m1} = \frac{Q}{A_1} \quad (2.10)$$

with the inlet area of the runner A_1 . For the flow conditions at the leading edge of the blade the incidence angle β_1 is significant. This can be derived further by the relative velocity vector \mathbf{w}_1 and the circumferential velocity vector \mathbf{u}_1 .

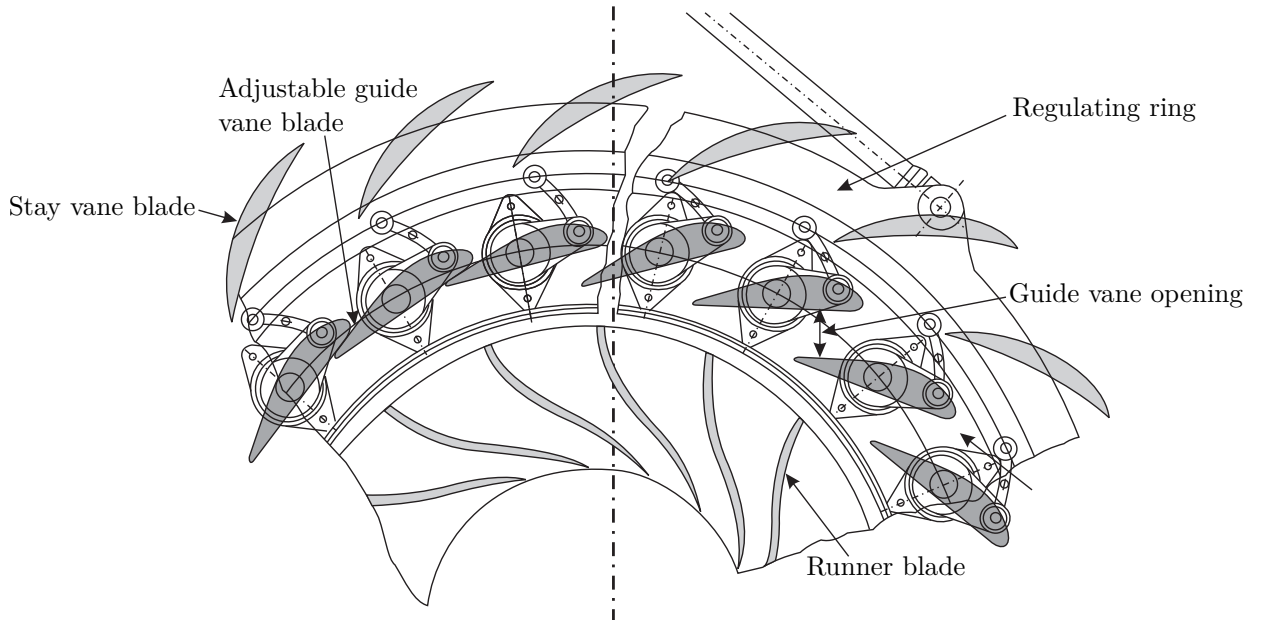


Figure 2.7: Adjustable guide vanes for a Francis turbine. Graphics adapted from Giesecke and Mosonyi [34].

At the runner outlet the flow direction in the rotating frame of reference β_2 is equal to the blade angle φ_2 , even deviations have been experimentally observed by Schilling et al. [84]. With the meridional amount of the absolute velocity c_{m2} using Eq. 2.10 with the outlet area A_2 the relative velocity vector \mathbf{w}_2 can be calculated. As already mentioned, the circumferential amount c_{u2} of the vector \mathbf{c}_2 becomes zero at the optimum operating point and therefore $\alpha_2 = 90^\circ$. At part load conditions the angle gets smaller with $\alpha'_2 < 90^\circ$ and therefore $c'_{u2} \neq 0$. At overload conditions the direction of c''_{u2} switches to the opposite of the rotating direction with $\alpha''_2 > 90^\circ$ (see Fig. 2.8).

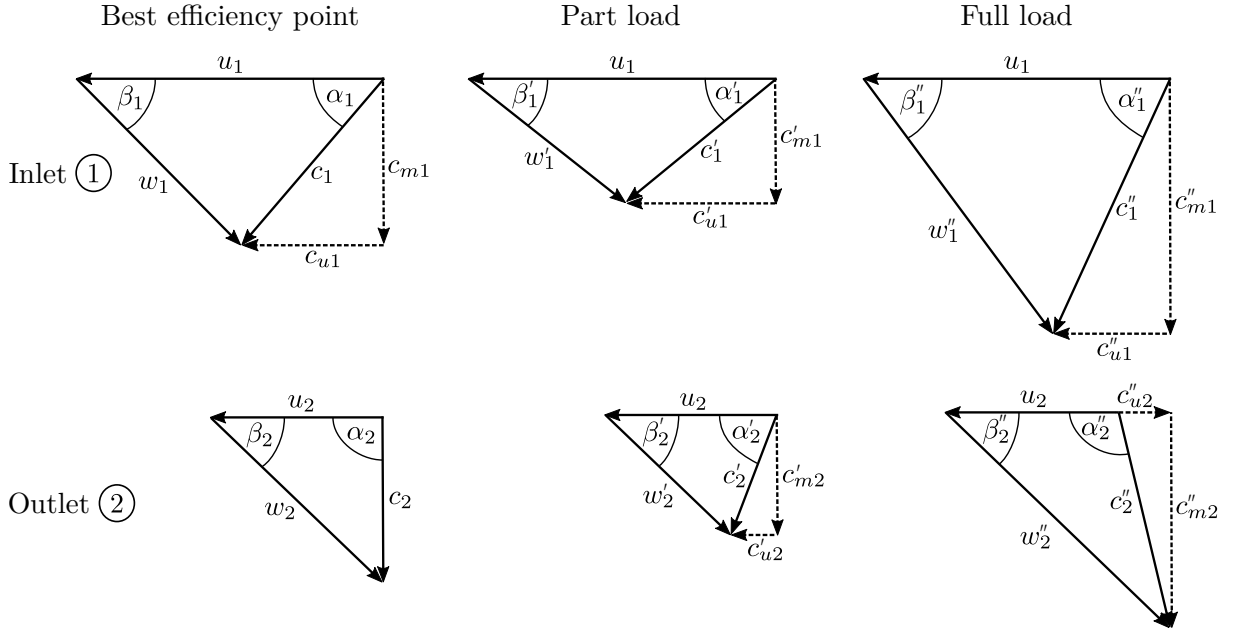


Figure 2.8: Velocity triangles for different operating points at the inlet and outlet of a Francis runner.

2.2.3 Operating Range

The operating range of a Francis turbine is determined by the head between the upper and the lower water level and the discharge. The characteristics of the hydraulic machine are usually described using a hill chart including the guide vane opening angle ϕ , the efficiency η and the resulting output power P . These values are normally measured using homologous model tests in a laboratory as prototype measurements are expensive and require a large effort. Those measurements are also used during the design phase to evaluate the behavior of the machine in different operating conditions considering unsteady effects, pressure fluctuations, instability limitations or cavitation. To transpose the characteristics from the model tests to the prototype machine the unit speed n_{11} and the unit discharge Q_{11} , which correspond to a geometrically similar turbine with a runner diameter of $D = 1 \text{ m}$ at a head of $H = 1 \text{ m}$, are used:

$$n_{11} = \frac{nD}{\sqrt{H}} \quad Q_{11} = \frac{Q}{D^2\sqrt{H}} \quad (2.11)$$

A typical hill chart of a Francis turbine is displayed in Fig. 2.9 including the operating range and iso-curves for the efficiency and the guide vane opening. Due to lower viscous losses at the prototype machine resulting from different Reynolds numbers Re and a higher ratio between the inertial and viscous forces the efficiency for the prototype turbine is higher than for the model. Empirically based correlations allow a transposition for the efficiency from model to prototype, as described by Giesecke and Mosonyi [34].

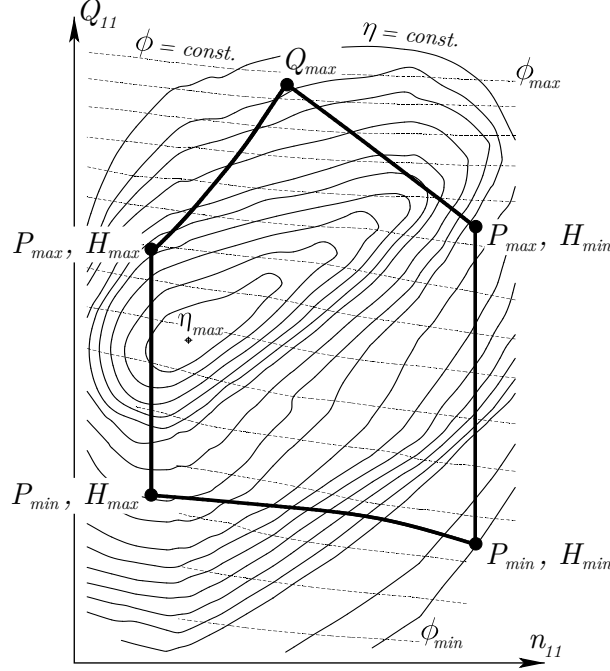


Figure 2.9: Hill chart of a Francis turbine including the operating range and iso-curves for the efficiency η and the guide vane opening ϕ . Graphics adapted from Magnoli [61].

2.2.4 Unsteady Flow Effects

Depending on the operating point of Francis turbines, different unsteady effects appear inside the machine causing dynamic pressure pulsations and structural excitations of affected components.

Best efficiency point

In the range of the best efficiency point the rotor-stator interaction (RSI), induced at the runner inlet by the pressure wakes of the guide vane blades, is mainly responsible for dynamic excitations. Especially high head Francis turbines with a low specific speed n_q are affected by the RSI due to the higher pressure difference and the smaller gap size between the runner and guide vane blades, as described by Seidel et al. [86]. The Francis turbine is harmonically excited at the so-called blade passing frequency f_{BP} induced by the RSI, which can be derived using the correlation

$$f_{BP} = z_g \frac{n}{60} = z_g f_0 \quad (2.12)$$

with the rotational frequency of the runner f_0 and the number of guide vane blades z_g . At the turbine outlet section the flow conditions are quite homogeneous in the BEP with hardly any swirl appearing and therefore the dynamic pressure oscillations are relatively low.

Full load operation

In high and full load operation the meridional amount of the absolute outlet velocity c''_{m2} increases due to a higher discharge. Hence, the circumferential component c''_{u2} increases as well with an absolute outflow angle of $\alpha''_2 > 90^\circ$, resulting in a counter-rotating swirl. In cases, where the static pressure drops below the vapor pressure of water due to local flow acceleration, a cavitating vortex core becomes visible similar to a torch pattern (see Fig. 2.10). According to Seidel et al. [87], the pressure fluctuations are usually small due to relatively stable flow conditions but in some cases oscillations may appear induced by the interaction of the vortex rope with the hydraulic system, as described by Flemming et al. [26]. As the guide vane blades reach their maximum opening position in full load operation resulting in a minimum gap to the runner, the RSI usually still remains the effect with the highest excitation at the turbine inlet section.

Part load operation

At part load operation the meridional component c'_{m2} decreases together with the outflow angle $\alpha'_2 < 90^\circ$. Hence, the circumferential velocity at the runner suction side and in the draft tube inlet section c'_{u2} increases. As a result, a part load vortex rope appears, which rotates in the runner direction and may lead to cavitation as well. In the center of the draft tube cone the velocity conditions induce a backflow leading to a spiral-like pattern of

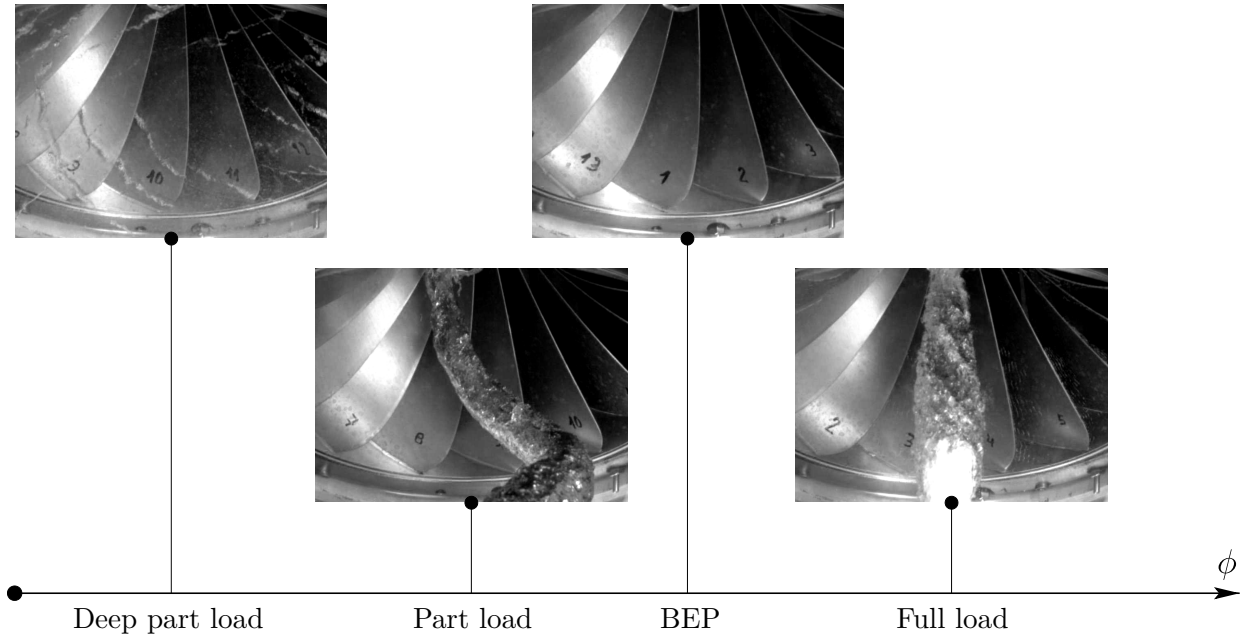


Figure 2.10: Dynamic flow effects at different operating conditions for a Francis turbine. Graphics adapted from Magnoli [61].

the vortex rope (see Fig. 2.10). Due to its rotating motion, periodic pressure fluctuations occur below the runner rotational frequency f_0 , which excite the machine structures in a harmonic way, as described by Seidel et al. [87]. Usually, the pressure oscillations are in the range of $0.2 < f_0 < 0.4$ but for high specific speed Francis turbines and for low Thoma cavitation numbers σ_T hydro-acoustic pressure waves in higher frequency ranges may appear, as discussed by Arpe et al. [1].

Deep part load operation

In deep part load operation the inlet velocity conditions are not consistent with the blade angle φ_1 and secondary flow effects may appear, especially for Francis turbines with high specific speeds. As a result, channel vortices occur inducing broadband pressure fluctuations and also cavitation due to the pressure drop inside the vortex core region. (see Fig. 2.10). With decreasing guide vane opening the draft tube vortex rope disappears and the flow becomes more stochastic leading to high energy dissipation. The numerical study of deep part load operation requires large computational efforts and the use of sophisticated turbulence models. Relevant investigations have been performed by Conrad et al. [12] and Yamamoto et al. [106].

Chapter 3

CFD in Hydraulic Turbomachines

In the last decades the role of numerical simulations to solve the fluid flow in hydraulic turbomachines has significantly increased. Experimental research in laboratory models can deliver certain information about the flow conditions and its impact but they require a large effort and do not yield detailed results for different flow parameters. Even though the basic equations for the description of the fluid motion have been well known for centuries, their analytical solution was limited to simple problems in most cases. The rapid rise of computing power together with its affordability enabled the numerical solution of the fluid dynamic equations in the field of CFD (Computational Fluid Dynamics). The implementation of the numerical formulations in the open-source CFD software OpenFOAM provides a broad access to the application of flow simulations. Hence, a short overview about OpenFOAM, which is used in the scope of this thesis, will be given at the beginning of this section, before the fundamentals of CFD are further discussed.

3.1 Introduction of OpenFOAM

OpenFOAM is an open-source code written in C++ and published under the *GNU General Public License* (GPL). It was invented in the late 1980s at the Imperial College of London and initially released in 2004 by the *OpenCFD Ltd.* However, the source code remains accessible for free even today. This circumstance encouraged further development especially in the field of academic and scientific research. In recent years, the growing capabilities of OpenFOAM have been considered as well as in industrial applications in addition to the usage of commercial software. The progress to exchange the technological knowledge in the course of various communities, conferences and workshops emphasizes its future role in the field of CFD. The extensibility for custom libraries and utilities is another advantage of OpenFOAM: Existing objects like turbulence models, boundary conditions or solvers can be modified and newly developed ones can be implemented without profound experience in C++. The possibility of parallel computing using e.g. the *OpenMPI* application and further third-party packages like the visualization tool *ParaView* enhance the significance of OpenFOAM. Pre-processing and I/O-interfaces further enable the connectivity with external software. The basic structure and simulation process of OpenFOAM is described in [76] and displayed in Fig. 3.1.

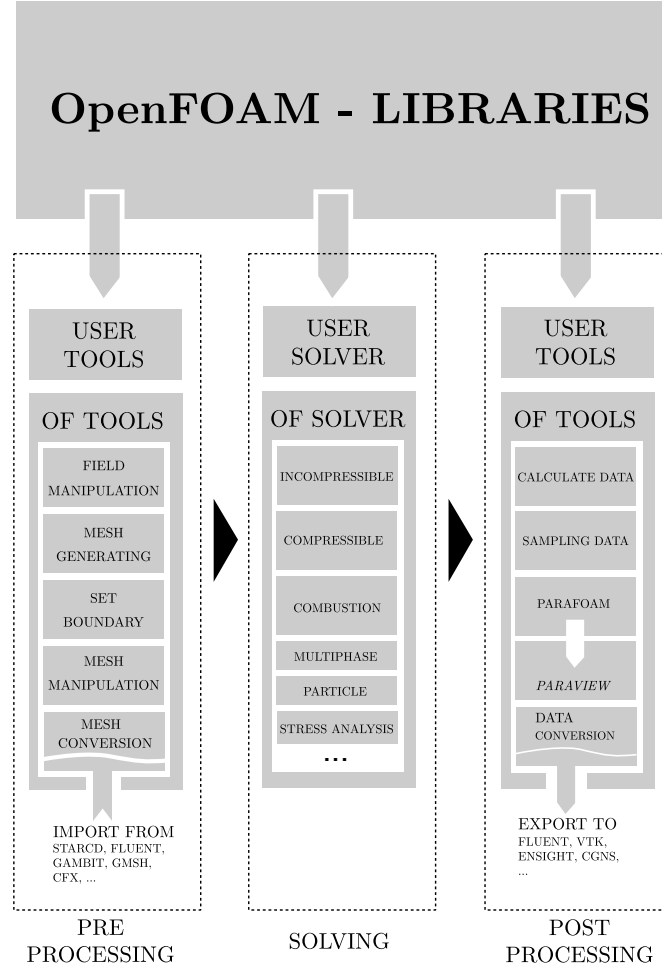


Figure 3.1: Basic structure and simulation process of OpenFOAM. Graphics from Erne [22].

3.2 Basic Equations of CFD

The motion of a fluid can be fully described in respect of the conservation laws for its extensive characteristics, the mass, momentum and energy, applied to an infinitesimal control volume. For the investigations performed in the course of this thesis the fluid is considered to be incompressible and isothermal. Hence, the energy equation is not considered. The knowledge of the pressure p and the velocity \mathbf{c} together with the fluid characteristics are sufficient to fully describe the flow. The equations for the conservation laws, also called the transport equations, are usually expressed in a differential form using a Cartesian coordinate system with the spatial coordinates x_i ($i = 1, 2, 3$ or x, y, z), the components c_i (c_x, c_y, c_z) of the velocity vector \mathbf{c} and the time t . Considering a constant density $\rho = \rho_0$ for incompressible fluids the mass conservation, also called continuity equation, can be therefore described in its reduced form according to Ferziger and Peric [25] by

$$\frac{\partial c_i}{\partial x_i} = \frac{\partial c_x}{\partial x} + \frac{\partial c_y}{\partial y} + \frac{\partial c_z}{\partial z} = \nabla \cdot \mathbf{c} = 0. \quad (3.1)$$

The conservation law for the momentum without any external field forces (e.g. gravitation) is described by

$$\rho_0 \frac{\partial c_i}{\partial t} + \rho_0 \frac{\partial(c_j c_i)}{\partial x_j} = \frac{\partial \tau_{ij}}{\partial x_j} - \frac{\partial p}{\partial x_i} \quad (3.2)$$

with the viscous part τ_{ij} of the total stress tensor T_{ij} . Considering the assumption of a Newtonian fluid, as it is valid for most fluids in the engineering area like water or air, and a constant dynamic viscosity $\mu = \mu_0$, the viscous stress tensor can be expressed by

$$\tau_{ij} = \mu_0 \left(\frac{\partial c_i}{\partial x_j} + \frac{\partial c_j}{\partial x_i} \right). \quad (3.3)$$

The first term in the momentum conservation equation is the variation with time (temporal term), followed by the convective term, the diffusive term, and the pressure gradient, respectively. In the field of CFD the conservation laws for the mass and the momentum are together commonly known as the Navier-Stokes equations¹. They are sufficient to describe the motion of a Newtonian, incompressible fluid but the analytical solution of the partial differential equations is only possible in simple cases. To solve the equations for more complex geometries and applications, numerical methods can be used to approximate the differential equations by a system of algebraic equations. Therefore, a discretization method has to be applied, which divides the system into smaller cells and allows to numerically solve the differential equations at discrete points in space and time (see Fig. 3.2). In addition to the Finite Difference Method (FDM) and the Finite Element Method (FEM) the most common and advanced discretization method for CFD is the Finite Volume Method (FVM). The related spatial and temporal discretization methods, interpolation schemes and solver are implemented in OpenFOAM and subsequently described below.

3.3 Finite Volume Discretization

The above introduced transport equation for the momentum can be written in its general vector form for a scalar variable Φ by

$$\rho_0 \frac{\partial \Phi}{\partial t} + \rho_0 \nabla \cdot (\Phi \mathbf{c}) - \nabla \cdot (\Gamma \nabla \Phi) = q_\Phi \quad (3.4)$$

with the diffusion coefficient Γ and the source or sink term q_Φ . The Finite Volume Method uses the integral formulation of the transport equation by integrating Eq. 3.4 for a control volume. By applying the Gauss theorem for the convective and diffusive terms the volume integrals can be expressed by surface integrals with the according normal face vector \mathbf{n} . Thus, the transport equation is written by

$$\rho_0 \frac{\partial}{\partial t} \int_V \Phi \, dV + \rho_0 \int_A \Phi \mathbf{c} \cdot \mathbf{n} \, dA = \int_A \Gamma \nabla \Phi \cdot \mathbf{n} \, dA + \int_V q_\Phi \, dV. \quad (3.5)$$

¹In physics the Navier-Stokes equations usually represent only the conservation law of the momentum.

3.3.1 Spatial Discretization

The Finite Volume Method divides the fluid domain into a finite number of small cells (control volumes), where the transport equations are applied. The numerical mesh represents the boundaries for each control volume and the variable Φ must be solved at each cell center. In the field of CFD usually structured meshes are used. The control volumes for an orthogonal and a non-orthogonal Cartesian 2D mesh with the indices of the structured grid i and j and the notation of the adjacent cell centers are displayed in Fig. 3.2.

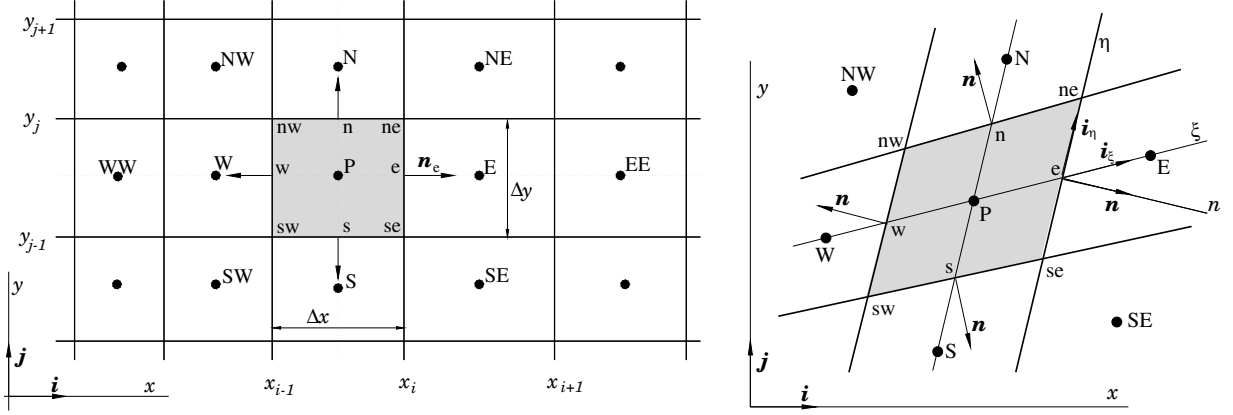


Figure 3.2: Control volume of an orthogonal (left) and a non-orthogonal structured 2D mesh (right) including the notation and indices. Graphics from Ferziger and Peric [25].

The biggest advantage of the Finite Volume Method is the implementation of the physical conservatism: For steady-state conditions the amount of a scalar variable, which enters and exits a control volume must be equal if no source or sink terms exist. In the case of the FVM the sum of the integral equation of each control volume is equal to the conservation equation of the whole solution area, which requires non-overlapping boundaries between the cells. As the interesting variable Φ is only available in the center of each control volume but the knowledge of the surface and volume integrals are needed to solve Eq. 3.5, the integral relations have to be approximated by algebraic expressions.

Numerical Approximations

For the surface integral F_e usually the so-called midpoint rule is applied with a second order accuracy expressed by

$$F_e = \int_{A_e} f \, dA = \bar{f}_e A_e \approx f_e A_e. \quad (3.6)$$

The variable value f in the point “e” must be approximated using an interpolation method for the values in adjacent control volumes. To assure the second order accuracy of the midpoint rule the used interpolation scheme must also be second order accurate.

The approximation for the volume integral Q_P is performed similar to the surface integral

and expressed by

$$Q_P = \int_V q \, dV = \bar{q} \Delta V \approx q_P \Delta V. \quad (3.7)$$

For the calculation of value q_P of q in the cell center no interpolation is necessary due to the knowledge of all variables in the center.

Discretization of the Convective Term

The flux of the convective term through the boundaries of the control volume is equal to the sum of the integrals for each cell face. Using Eq. 3.6 the convective flux through the face e can be approximated by

$$F_e^c = \rho_0 \int_{A_e} \Phi \mathbf{c} \cdot \mathbf{n} \, dA = \rho_0 \Phi_e \int_{A_e} \mathbf{c} \cdot \mathbf{n} \, dA \approx \Phi_e \dot{m}_e \quad (3.8)$$

with the mass flux \dot{m}_e through the cell face and the value Φ_e of Φ in the center of the control volume, which has to be approximated using a second order interpolation scheme.

Discretization of the Diffusive Term

The diffusive term for the cell face e can be approximated using the midpoint rule by

$$F_e^d = \int_{A_e} \Gamma \nabla \Phi \cdot \mathbf{n} \, dA \approx (\Gamma \nabla \Phi \cdot \mathbf{n})_e A_e = \Gamma_e \left(\frac{\partial \Phi}{\partial x_j} \right)_e \mathbf{n}_e A_e. \quad (3.9)$$

Related to the face normal direction the derivation can be written by

$$F_e^d = \Gamma_e \left(\frac{\partial \Phi}{\partial n} \right)_e \mathbf{n}_e A_e. \quad (3.10)$$

and it has to be approximated by a second order interpolation scheme as well.

3.3.2 Interpolation Schemes

Several interpolation schemes with different orders of accuracy exist and are further developed. The most common are the upwind difference scheme (UDS) and the central difference scheme (CDS):

Upwind Difference Scheme

The easiest determination of the value Φ_e in the midpoint of the control volume surface is the approximation using the value Φ_P in the center of the upwind adjacent cell (or downwind - depending on the flow direction). The Taylor series expansion around the point P for a

Cartesian coordinate system is expressed by

$$\Phi_e = \Phi_P + (x_e - x_P) \left(\frac{\partial \Phi}{\partial x} \right)_P + \frac{(x_e - x_P)^2}{2} \left(\frac{\partial^2 \Phi}{\partial x^2} \right)_P + H \quad (3.11)$$

with the terms of higher order H . The upwind difference scheme only consists of the first term on the right side and is therefore a first order accurate flux approximation. The leading truncation error resembles the diffusive flux

$$f_e^d = \Gamma_e \left(\frac{\partial \Phi}{\partial x} \right)_e \quad (3.12)$$

with the numerical diffusion coefficient $\Gamma_e = (\rho c)_e \Delta x / 2$. The upwind difference scheme is therefore “numerically diffusive” and the accuracy of the solution depends on the mesh density. The application of the UDS for most CFD simulations should be avoided as the usually used meshes are too coarse to achieve sufficient accuracy. Due to the advantage of the UDS regarding its stability it can be used for initial computations as it produces no oscillating solutions.

Central Difference Scheme

In addition to the determination of the value Φ_e by the upwind cell center value, it can also be obtained using an interpolation between two adjacent cells centers P and E . This interpolation method is called the central difference scheme (CDS). The Taylor series expansion can be written by

$$\Phi_e = \Phi_E \lambda_e + \Phi_P (1 - \lambda_e) - \frac{(x_e - x_P)(x_E - x_e)}{2} \left(\frac{\partial^2 \Phi}{\partial x^2} \right)_P + H \quad (3.13)$$

with the linear interpolation factor

$$\lambda_e = \frac{x_e - x_P}{x_E - x_P}. \quad (3.14)$$

The leading truncation error is depending on the square of the mesh distance and is therefore of second order accuracy. As the interpolation is done along a straight line between the cell center points, its application on non-orthogonal meshes introduces an additional error as the face center is not aligned on the connecting line. Especially, the interpolation of the gradient for the diffusive flux $\nabla \Phi$ can lead to convergence oscillations as the face normal derivatives have to be interpolated from the cell center to the face center. The orthogonality of the used meshes is therefore an important factor to ensure accurate numerical results.

3.3.3 Temporal Discretization

For unsteady fluid flows the temporal term in the transport equation has to be discretized as well. The change of a variable Φ along the time t can be described by a first order

differential equation

$$\frac{d\Phi(t)}{dt} = f(t, \Phi(t)) \quad (3.15)$$

with the initial condition $\Phi(t_0) = \Phi^0$. The value $\Phi^{n+1} = \Phi(t_{n+1})$ at a time step $t_{n+1} = t_n + \Delta t$ can be determined by the integration of Eq. 3.15 from the interval t_n to t_{n+1} :

$$\int_{t_n}^{t_{n+1}} \frac{d\Phi(t)}{dt} dt = \Phi^{n+1} - \Phi^n = \int_{t_n}^{t_{n+1}} f(t, \Phi(t)) dt. \quad (3.16)$$

The solution of Eq. 3.16 is not directly possible as the temporal progression of f is not known. Therefore, an approximation of the temporal integral has to be used. The implemented schemes in OpenFOAM are subsequently described below.

Implicit Euler Scheme

One approach is to approximate the integral with the integrand at the end of the interval:

$$\Phi^{n+1} = \Phi^n + f(t_{n+1}, \Phi^{n+1}) \Delta t. \quad (3.17)$$

The temporal derivative can be therefore expressed by

$$\frac{\partial \Phi}{\partial t} = \frac{\Phi^{n+1} - \Phi^n}{\Delta t} \quad (3.18)$$

The so called implicit Euler method is the simplest temporal discretization scheme implemented in OpenFOAM. It has a high numerical stability but the accuracy is of first order in time as the value Φ^{n+1} has to be determined implicitly. It should only be used for initial computations of unsteady problems.

Crank-Nicolson Scheme

Another temporal discretization approach is the approximation of the integral by the values at the beginning and end of the interval:

$$\Phi^{n+1} = \Phi^n + \frac{1}{2} [f(t_n, \Phi^n) + f(t_{n+1}, \Phi^{n+1})] \Delta t. \quad (3.19)$$

The Crank-Nicolson scheme is unconditionally stable and is second order accurate in time but it can lead to oscillating solutions. The advantage of this discretization method is the higher accuracy for small time steps.

Backward Difference Scheme

The backward time discretization scheme is similar to the implicit Euler method but uses three time steps instead. It is therefore of second order accuracy and unconditionally stable. It can also produce oscillating solutions but only at larger time steps compared to

the Crank-Nicolson scheme. According to Hairer and Wanner [41] the temporal derivative can be written by

$$\frac{\partial \Phi}{\partial t} = \frac{3\Phi^{n+1} - 4\Phi^n + \Phi^{n-1}}{2\Delta t}. \quad (3.20)$$

Stability of the Temporal Discretization

For the stability of a temporal discretization scheme the so called CFL (Courant-Friedrichs-Lewy) or Courant number Co can be used, which is the ratio between the propagation time of a disturbance $c/\Delta x$ and the time step size Δt :

$$Co = \frac{c\Delta t}{\Delta x} \leq Co_{max}. \quad (3.21)$$

The maximum Courant number depends on the used discretization scheme. For an explicit method (e.g. explicit Euler) it is limited by $Co_{max} \leq 1$ but the previously mentioned schemes are even stable at higher CFL numbers. The Courant number depends also on the local mesh size and differs therefore along the fluid domain. For the CFD simulations performed in this thesis, investigating the fluid flow in Francis turbines with OpenFOAM, the time step size is adjusted according to maximum Courant numbers of $Co_{max} \approx 50$.

3.3.4 Solving the Navier-Stokes Equations

Iterative Solvers

The result of the spatial and temporal discretization using the Finite Volume Method is a system of algebraic equations for the whole solution domain in matrix form, which consists of the partial differential equations for each control volume. In the field of CFD the most common approach is the application of iterative solution methods. Usually an accuracy in the range of the discretization is sufficient and therefore a precise solution of the algebraic equations, which needs a high amount of resources, is not necessary. Considering a matrix problem

$$A\Phi = Q \quad (3.22)$$

with the coefficient matrix A , the vector Φ consisting of the exact variable values in the control volumes and the vector Q consisting of the volume integrals Q_P , an iterative method yields an approximate solution Φ^n after n iterations:

$$A\Phi^n = Q - \rho^n. \quad (3.23)$$

The remaining term ρ^n is therefore different from zero. With the iteration error $e_{it}^n = \Phi - \Phi^n$

the residuum is defined by

$$Ae_{it}^n = \rho^n \quad (3.24)$$

which should approach to zero for an infinite iteration number. It is therefore important to define convergence criteria to minimize the number of iteration steps for a solution with sufficient accuracy. Based on empirical knowledge the iterative process can be aborted if the residuals have dropped by an order of three to five, as described by Ferziger and Peric [25].

Pressure and Velocity Coupling

In the Navier-Stokes equations the pressure field p is only related to the momentum equation but not to the continuity equation. The velocity field with the components c_x , c_y and c_z in the 3D case can be derived from the momentum equation but therefore the pressure gradient must be known. The most common approach for stationary, incompressible fluid flows considering the coupled behavior of the pressure and velocity field is the SIMPLE algorithm by Caretto et al. [8]: To satisfy the mass conservation the velocity and the pressure field are sequentially solved. The particular velocity components are solved with presumed values of the pressure and the remaining velocities from the previous iteration step. The continuity equation is usually not satisfied with the achieved velocity field and therefore a pressure correction is used to compute a new velocity field. At the end the continuity equation should be satisfied using the corrected velocity field within a certain tolerance. Considering the convergence a drop of the residuals of one magnitude is sufficient except the solution of the pressure correction. A method to improve the convergence for the SIMPLE algorithm is the under-relaxation, which limits the change of a variable in the Navier-Stokes equations between each iteration. For a variable Φ at the iteration step n it can be expressed by

$$\Phi^n = \Phi^{n-1} + \alpha_\Phi(\Phi - \Phi^{n-1}) \quad (3.25)$$

with the under-relaxation factor α_Φ , which satisfies the condition $0 < \alpha_\Phi < 1$. The convergence is therefore more stable using a smaller under-relaxation factor but the disadvantage is a reduction of speed. For unsteady problems the PISO algorithm can be used proposed by Issa [46], which can be coupled with the SIMPLE algorithm to the so called PIMPLE method. It combines the advantage of relative large time steps with an improved convergence and stability using inner iteration loops. It is implemented in OpenFOAM and is used for the unsteady CFD simulations in this thesis.

Parallelisation

Presently due to the affordable computing power, the distribution of the algebraic system defined in Eq. 3.22 to several computer cores helps to significantly improve the simulation duration. Therefore, the computational mesh of the full domain is partitioned according to the number of processors, which solve the equations separately. The information at the interfaces is exchanged between the cores, which limits the increase of speed to a maximum

number of processors, depending on the mesh size and the used communication tool (e.g. OpenMPI).

3.4 Simulation of Turbulent Fluid Flow

The fluid flow in most practical cases, especially for hydraulic turbomachines, is determined by a turbulent behavior. The characteristic values like the velocity are unsteady and intensely fluctuating in space and time scale. Several mathematical approaches exist to describe the physical behavior of turbulent fluid flows but an exact solution is hard to achieve. One main characteristic of turbulence is the presence of eddies in different size, which are responsible for the dissipation of energy. The kinetic energy is transferred from large scaled eddies to smaller scales and is dissipated at the smallest eddies to internal energy due to friction. The larger eddies contain the biggest energy amount, which is derived from the small variations of the characteristic flow values around the mean flow. The most precise description of turbulence is achieved using Direct Numerical Simulations (DNS) to exactly solve the Navier-Stokes equations. However, the numerical effort using DNS is huge and its application is limited to simple geometries. Hence, it is not appropriate to solve the flow in hydraulic turbomachines and therefore different modeling approaches have been developed with varying scope of application and accuracy. The most important apart from DNS are categorized as follows:

- RANS (Reynolds Averaged Navier-Stokes): This approach is based on the statistical averaging of the transport equations. The achieved partial differential equations (Reynolds averaged Navier-Stokes equations) do not form a closed system and therefore numerical approximations are necessary (turbulence modeling). RANS models are the most common approach to determine turbulence but they are only able to describe an averaged flow field.
- LES (Large Eddy Simulation): The above described approximations are applied only to small scale eddies. The transport equations for large scale fluid motions are solved directly. It is therefore a compromise between the RANS modeling approach and DNS.

Further, hybrid turbulence models have been developed, which combine the advantages of RANS and LES approaches. The most common hybrid models are DES (Detached Eddy Simulation) or SAS (Scale-Adaptive Simulation).

It is important to mention that turbulence modeling is only an approximation of the physical fluid behavior. In addition, no single turbulence model exists, which is capable of predicting reliable results for all kinds of turbulent flows. In the following sections the RANS and LES approaches together with the hybrid SST-SAS model are discussed, as they are used in the scope of this thesis. Further, the wall treatment for turbulent CFD simulations is mentioned.

3.4.1 RANS Modeling Approach

The characteristic values Φ of a turbulent fluid flow can be described by the sum of its average $\bar{\Phi}$ and the according fluctuating term Φ' :

$$\Phi(x_i, t) = \bar{\Phi}(x_i) + \Phi'(x_i, t). \quad (3.26)$$

For statistical steady fluid flows a temporal averaging approach can be applied with a preferably large averaging interval T (see Fig. 3.3, left). For an unsteady flow behavior the Ensemble averaging approach can be used (see Fig. 3.3, right).

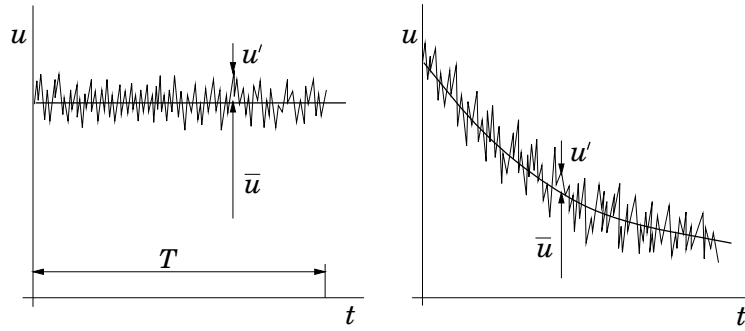


Figure 3.3: Temporal averaging of the velocity u for a statistical steady flow (left) and Ensemble averaging of unsteady flows (right). Graphics from Ferziger and Peric [25].

The application of an averaging procedure (Reynolds averaging) to the Navier-Stokes equations leads subsequently to the averaged mass and momentum conservation equations:

$$\frac{\partial \bar{c}_i}{\partial x_i} = 0, \quad (3.27)$$

$$\rho_0 \frac{\partial \bar{c}_i}{\partial t} + \rho_0 \frac{\partial}{\partial x_j} (\bar{c}_i \bar{c}_j + \overline{c'_i c'_j}) = \frac{\partial \bar{\tau}_{ij}}{\partial x_j} - \frac{\partial \bar{p}}{\partial x_i}, \quad (3.28)$$

with the averaged viscous stress tensor

$$\bar{\tau}_{ij} = \mu_0 \left(\frac{\partial \bar{c}_i}{\partial x_j} + \frac{\partial \bar{c}_j}{\partial x_i} \right). \quad (3.29)$$

The additional term $\overline{c'_i c'_j}$ compared to the momentum equation is known as the Reynolds stress tensor, although it is not a stress tensor in the common sense. The presence of these further unknown variables exceeds the number of available equations, which is called the *closure problem*. As it is not possible to derive a closed system of exact equations, numerical approximations have to be used - the so-called turbulence models. Several approaches exist with an increasing number of model equations and therefore related complexity. The simplest way of turbulence modeling is represented by algebraic or zero equation models with low required computational effort but limited applicability for fluid flow problems.

The most common approach for CFD simulations is using first-order closure **Eddy-Viscosity Models (EVM)**. They are based on the hypothesis by Boussinesq [6], who postulated that the influence of turbulence on energy dissipation and the transport of mass and momentum can be described by an increased viscosity, similar to laminar flows. Hence, the Reynolds stresses can be derived by

$$-\overline{c'_i c'_j} = \nu_t \left(\frac{\partial \bar{c}_i}{\partial x_j} + \frac{\partial \bar{c}_j}{\partial x_i} \right) - \frac{2}{3} \delta_{ij} k \quad (3.30)$$

with the kinetic energy of turbulence $k = \frac{1}{2} \overline{c'_i c'_i}$ and the turbulent or eddy viscosity $\nu_t = \mu_t / \rho_0$. The latter is a function of the local flow conditions and not a characteristic value of the fluid like the molecular viscosity μ . The determination of the eddy viscosity is the purpose of the EVM to solve the closure problem. A large variety of first-order closure models exist ranging from simple algebraic or zero-equation models over one-equation models as proposed by Spalart and Allmaras [90] to advanced multi-equation approaches. The most common applied ones are two-equation turbulence models like the k - ε model, the k - ω model developed by Wilcox [105] or the widespread Shear-Stress-Transport model k - ω SST developed by Menter [65].

The disadvantage of the Eddy-Viscosity Models is the lack of capturing anisotropic non-linear effects in 3D fluid flows caused for example by strong streamline curvature, vortex flow effects or separated flows. Second-order closure models like the more sophisticated **Reynolds Stress Models (RSM)** or **Algebraic Stress Models (ASM)** are able to consider anisotropy but are quite complex in their application and therefore seldom used. In the scope of this thesis only the EVM based k - ω SST model implemented in OpenFOAM 2.3 is used, which seeks to combine the advantages of both the k - ε and the k - ω model. They are therefore briefly discussed below.

k - ε Turbulence Model

One approach for two-equation turbulence models is the expression of the eddy viscosity ν_t as a function of the turbulent kinetic energy k and the turbulent dissipation rate ε . The coupled partial differential equations lead to the correlation

$$\nu_t = C_\mu \frac{k^2}{\varepsilon} \quad (3.31)$$

with the turbulence model constant C_μ . This approach is used in a large range of k - ε models (e.g. the standard k - ε model by Launder and Spalding [52]). The advantages of the k - ε models are the relatively simple implementation in CFD applications and the reasonable prediction of the flow in free stream zones with fully developed turbulence. The disadvantage is the lack of accuracy in the near-wall region, where high flow gradients appear. To stay valid in the viscous sublayer close to the wall, low- Re versions are used including so-called damping functions. However, to compute the flow explicitly in the near-wall region very fine meshes are necessary, especially considering high Reynolds numbers. The wall treatment of turbulent flows will be discussed in the following section.

k- ω Turbulence Model

Another approach to obtain the eddy viscosity ν_t is the expression using a modified equation for k from the k - ε model and a transport equation for the turbulent dissipation frequency

$$\omega = \frac{1}{C_\mu} \frac{\varepsilon}{k}, \quad (3.32)$$

which leads to the formulation $\nu_t = k/\omega$. The numerical behavior of the k - ω turbulence model is similar to the k - ε model but it needs no damping functions and has therefore an improved numerical stability in the near-wall region. On the other hand it exhibits an increased sensitivity of the flow behavior due to free stream boundary conditions of ω .

k- ω SST Turbulence Model

The two-equation turbulence model k - ω SST combines both previously mentioned approaches by switching from the k - ε model in the free stream zone to the k - ω formulation in the near-wall region with the use of blending functions F_n . The coefficients in the transport equations for the SST model are blended linearly between a value Φ_1 for k - ω and Φ_2 for k - ε by

$$\Phi = F_1 \Phi_1 + (1 - F_1) \Phi_2. \quad (3.33)$$

The eddy viscosity is obtained by

$$\nu_t = \frac{a_1 k}{\max(a_1 \omega, |\mathbf{S}| F_2)} \quad (3.34)$$

with the first invariant $|\mathbf{S}|$ of the strain-rate tensor S_{12} and the constant $a_1 = 0.31$. A detailed formulation of the transport equations, coefficients and blending functions for the SST model is described by Blazek [5] or Erne [22].

3.4.2 LES Modeling Approach

The general idea of the Large Eddy Simulation approach is to explicitly solve large scale eddies, which contain the most energy in turbulent fluid flows, as originally proposed by Smagorinsky [89]. The dynamics of small turbulent structures are modeled depending on their influence on the large scale motions. Presently LES is commonly applied to engineering problems with complex geometries, where standard RANS models lack accuracy or even fail. This is additionally supported by the increased computing power at a low-cost level. Although LES requires high-resolution grids with a large number of cells, it is in practice far more applicable than DNS. It can be further combined with RANS turbulence models (hybrid models) and wall function approximations to apply it at reasonable computational costs.

To evaluate the influence of small scale eddies spatial filtering is used to decompose the flow variables like the velocity c_i into a filtered LES component \bar{c}_i , which is resolved, and a

sub-filter component c'_i , which is modeled:

$$c_i = \bar{c}_i + c'_i. \quad (3.35)$$

The LES component is determined using a spatial filter function $F_{LES}(\mathbf{x}, \mathbf{x}', \Delta)$ applied to the complete fluid volume V by

$$\bar{c}_i(\mathbf{x}, t) = \int_V c_i(\mathbf{x}', t) F_{LES}(\mathbf{x}, \mathbf{x}', \Delta) dV' \quad (3.36)$$

with the filter width Δ . Different filter functions are used like the Tophat filter, the sharp Fourier cut-off filter, or the Gaussian filter. A detailed description of the filters would exceed the scope of the thesis but can be found in Vasilyev et al. [100]. The application of the filter function to the Navier-Stokes equations eliminates the small turbulent structures. In the governing equations the so-called subgrid-scale stress (SGS) tensor τ_{ij}^S appears with the correlation

$$\tau_{ij}^S = \overline{c_i c_j} - \bar{c}_i \bar{c}_j. \quad (3.37)$$

It describes the effects of the small scales, which have to be modeled to solve the closure problem. The subgrid-scale models have to determine the energy transfer between the large and small scales. Different approaches exist like the Eddy-Viscosity Model or the Smagorinsky [89] SGS Model.

3.4.3 Scale-Adaptive Simulation Approach

Pure LES simulation approaches still exceed reasonable computational efforts in most engineering fluid dynamic problems but would reveal more precise information about the flow behavior. In cases of distinct differences between dominant large eddies and the turbulent fluid motion regarding their characteristic frequencies, a combination of URANS (unsteady RANS) and LES methods can be used in hybrid models. One approach besides the Detached-Eddy-Simulation is the so-called Scale-Adaptive Simulation method suggested by Menter and Egorov [67]. The idea of SAS is to dynamically switch from standard RANS in stable flow regions to LES behavior to resolve the turbulent spectrum in unsteady zones. The information for the automatic adjustment is provided by the von Karman length-scale L_{vK} , which is based on the reformulation of the integral length-scale by Rotta [83]. The SAS approach can be applied in conjunction with different two-equation turbulence models, but it is usually combined with the $k-\omega$ SST model as proposed by Menter and Egorov [67], leading to the SST-SAS formulation. The difference in the governing equations to the RANS-SST model is an additional source term Q_{SAS} in the transport equation for the turbulent dissipation frequency ω , which reduces the turbulent viscosity, as described in the latest version of the SST-SAS model by Egorov and Menter [19]. This formulation has been implemented in OpenFOAM 2.3 and is used as well in the scope of this thesis to evaluate the capabilities for hydraulic turbomachines compared to the RANS-SST model. Similar investigations have been performed using commercial codes by Nennemann et al. [74]. The

advantage of the SAS approach in comparison to DES is the ability to operate on coarser meshes as well by switching to a RANS formulation. Although, fine mesh resolution is required to resolve small scale turbulence, the eddy viscosity and therefore the damping of flow structures can be reduced by one order compared to pure RANS-SST even on a coarse mesh as shown by Krappel et al. [50].

3.4.4 Wall Treatment in Turbulent Flows

The wall treatment in turbulent fluid flows is of special interest as the boundary flow can influence the behavior in the whole fluid domain and needs therefore proper assessment in CFD. In hydraulic turbomachines with high Reynolds numbers the resolution of the narrow viscous sublayer would require fine mesh densities in the wall-adjacent region leading to an excessive computational effort. Hence, the introduction of mathematical approximations (“wall functions”), to adequately describe the flow behavior close to no-slip walls, is desired, especially if the flow in the laminar sublayer is not of primary interest. The investigation of the viscous flow effects in the course of the boundary layer theory evolved a detailed knowledge of the flow in the near-wall region. To describe this behavior the introduction of non-dimensional variables like the dimensionless wall distance y^+ and the dimensional velocity u^+ is a common approach. They are defined by

$$y^+ = \frac{yu_\tau}{\nu_k} \quad \text{and} \quad u^+ = \frac{u}{u_\tau} \quad (3.38)$$

with the velocity u parallel to the wall, the friction or shear velocity u_τ , the kinematic viscosity ν_k and the scalar wall distance y . According to Fig. 3.4 the description of the velocity profile in the wall-normal direction can be divided into three main regions:

- Laminar sublayer ($y^+ < 5$)
- Buffer layer ($5 < y^+ < 60$)
- Log-law region ($y^+ > 60$)

Laminar sublayer

The flow behavior in the near-wall region is mainly characterized by the wall shear stress τ_w with the correlation

$$u_\tau = \sqrt{\frac{\tau_w}{\rho}}. \quad (3.39)$$

As the turbulent fluctuations together with the Reynolds number are decreasing close to the wall due to high velocity gradients the molecular viscosity of the fluid is dominant. The velocity profile can be subsequently assumed with a linear relationship between u^+ and y^+ :

$$u = \frac{y\tau_w}{\mu} = \frac{yu_\tau^2}{\nu_k} \rightarrow u^+ = y^+. \quad (3.40)$$

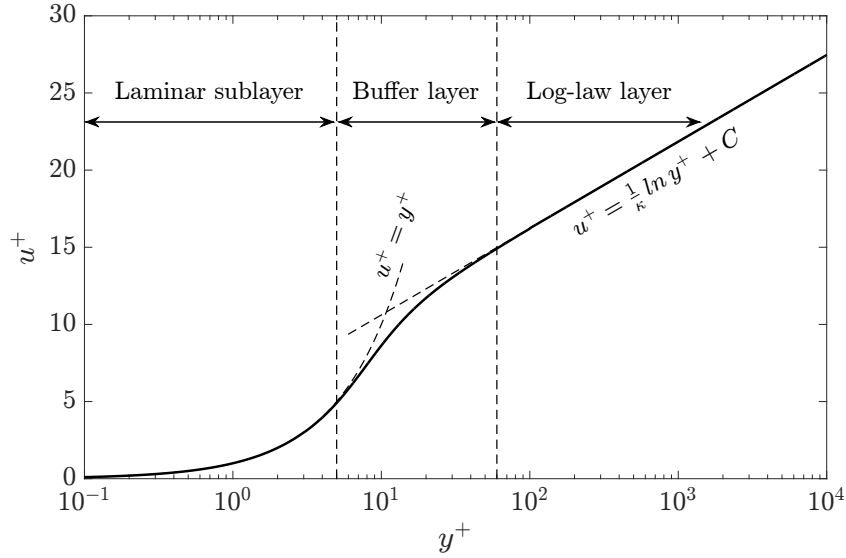


Figure 3.4: Velocity profile in the near-wall region of a turbulent fluid flow defined by the dimensionless velocity u^+ as a function of the dimensionless wall distance y^+ .

Log-law layer

With an increasing distance y in the wall-normal direction the turbulent viscosity is mainly influencing the flow behavior and the velocity profile can be approximated by the logarithmic law

$$u = \frac{u_\tau}{\kappa} \ln y^+ + C u_\tau \quad \rightarrow \quad u^+ = \frac{1}{\kappa} \ln y^+ + C. \quad (3.41)$$

In Eq. 3.41 κ is the von Karman constant ($\kappa = 0.41$) and C is an empirical constant in relation to the thickness of the viscous sublayer and the surface roughness of the wall. For smooth walls it can be derived by $C = 5.2$.

With the application of wall functions in a turbulent CFD simulation, the velocity profile in the near-wall region can be adequately approximated using a sufficient mesh resolution considering the wall-adjacent cell to be in the log-law layer region. It is important to mention that wall functions are only valid in stable boundary regions without considerable flow separation. Different wall function approaches have been developed with varying advantages and disadvantages. A detailed description would exceed the scope of this thesis. Nevertheless, the standard wall functions implemented in OpenFOAM have been used here in combination with the applied turbulence models for all CFD simulations.

3.4.5 Boundary Conditions

To solve the numerical system for turbulent flows, appropriate boundary conditions at the borders of the fluid domain (inlet, outlet, wall) have to be defined. Further, if separate block type fluid domains are used, according definitions at the non-conformal mesh interfaces have to be applied to assure the mass conservation. The most common definitions, which have been used in this thesis, are briefly described as follows.

Inlet

At the inlet surface the flow velocity with its components c_i or the discharge Q together with the flow direction and an optional velocity profile can be set. The pressure gradient for an incompressible fluid is assumed to be constant and the pressure values are therefore extrapolated from the internal fluid domain. The turbulent kinetic energy is usually derived by the inlet velocity C_{in} and the turbulent intensity I , which is typically in the range between 1 % and 20 %:

$$k_{in} = \frac{3}{2} I^2 C_{in}^2. \quad (3.42)$$

For long enough inlet sections the influence of the turbulent intensity on observed flow regions is negligible. The turbulent dissipation frequency at the inlet ω_{in} can be assumed with the turbulent mixing length $l_m = 0.07 d_{in}$ and the pipe diameter d_{in} by

$$\omega_{in} = C_\mu^{-0.25} \frac{\sqrt{k_{in}}}{l_m}. \quad (3.43)$$

Outlet

At the outlet surface the velocity gradient is set to be constant as well as the gradients for the turbulence quantities. The pressure can be defined to a constant value for each face or to a surface average, which usually improves the convergence for the simulation.

Wall

At the solid walls the mass flow in the normal direction n is zero and usually a no-slip condition is applied with a smooth surface roughness. Therefore, the velocity components are equal to the velocity for the wall itself. The turbulent kinetic energy and its derivative at the wall are equal to zero ($k_w = 0$, $\partial k_w / \partial n = 0$). For the dissipation frequency the value close to the wall tends to $\omega_w \rightarrow 0$, which requires a limiting function α_w for the numerical computation. The value for the limiter was proposed by Menter [66] to $\alpha_w = 10$ and the dissipation frequency at the center of the wall adjacent cell can be described by

$$\omega_w = \alpha_w \frac{6\nu_k}{\beta_t y_w^2} \quad (3.44)$$

with the distance of the cell center to the wall y_w and the constant $\beta_t = 0.075$.

Interfaces

As the fluid zones in the simulation of hydraulic turbomachines are usually discretized using separate block domains, the non-conformal interfaces between each domain have to be connected appropriately. Further, this approach is necessary to couple stationary and rotating domains. At the interfaces the flux conservation has to be assured by an interpolation between the adjacent surfaces. In the scope of this thesis the Arbitrary Mesh Interface (AMI) approach implemented in OpenFOAM 2.3 is applied.

Chapter 4

FEM in Hydraulic Turbomachines

To obtain the static and dynamic structural response of the investigated Francis runners affected by the fluid flow behavior, numerical computations are performed using the Finite Element Method (FEM). The concept is based on the formulations of the linear elasticity theory and the equation of motion for elastic, solid bodies. The first applications of FEM started in the 1950s in the field of aerospace engineering and were further extended to the automotive engineering sector. Similarly to the development of numerical flow simulations the significance of FEM increased steadily according to rising computing power. Hence, it is presently the most common approach for the structural computation in a wide range of engineering applications. Various commercial FEM programs exist but the usage of open-source tools is gaining popularity due to their advanced capabilities. In the scope of this thesis the freely available program Code_Aster is used for the structural investigations, which is briefly described below. Further, the basic equations and the concept of FEM including the discretization method are described according to Rammerstorfer [81]. The idea of fluid-structure interactions (FSI) to couple CFD and FEM for more detailed investigations is outlined in addition.

4.1 Introduction of Code_Aster

Code_Aster is an open-source FEM code written in the program language *Fortran*. It was developed by the French electricity company *Électricité de France (EDF)* primarily for internal use only but had later been published in 1999 under GPL. Although its communication language is French, the program is increasingly used outside the French-speaking community, also supported by the English documentation and the developed usability. Further, the extensibility for custom utilities and the application of Python-based codes for I/O-commands enhances the capabilities of Code_Aster. Different types of structural simulations are available like static, dynamic, thermal, non-linear or fatigue analysis. Pre- and post-processing tools like the Salome platform can be used for the discretization and evaluation of mechanical problems. The advanced capabilities and possibilities of Code_Aster have been considered as well for industrial applications in addition to the usage of commercial software.

4.2 Basics of the Linear Elasticity Theory

For the assessment of the static and dynamic structural behavior of an elastic body the mechanical strains and stresses are significant. The linearized relation between the displacements and the strains can be described by

$$\epsilon_{ij} = \frac{1}{2} \left(\frac{\partial u_i}{\partial x_j} + \frac{\partial u_j}{\partial x_i} \right) \quad (4.1)$$

with the strain tensor ϵ_{ij} and the local structural displacement $u_i = (u, v, w)$ at the point $x_i = (x, y, z)$. The relation can be written in its general form by

$$\boldsymbol{\epsilon} = \mathbf{d} \mathbf{u} \quad (4.2)$$

with the strain vector $\boldsymbol{\epsilon}$, the differential operator matrix \mathbf{d} and the displacement vector $\mathbf{u} = (u \ v \ w)^T$. In a Cartesian coordinate system the strain vector is defined by

$$\boldsymbol{\epsilon} = \left(\epsilon_{xx} \ \epsilon_{yy} \ \epsilon_{zz} \ \gamma_{xy} \ \gamma_{yz} \ \gamma_{xz} \right)^T \quad (4.3)$$

with the shear angle $\gamma_{ij} = 2 \epsilon_{ij}$. The differential operator matrix is defined by

$$\mathbf{d} = \begin{pmatrix} \partial/\partial x & 0 & 0 & \partial/\partial y & 0 & \partial/\partial z \\ 0 & \partial/\partial y & 0 & \partial/\partial x & \partial/\partial z & 0 \\ 0 & 0 & \partial/\partial z & 0 & \partial/\partial y & \partial/\partial x \end{pmatrix}^T \quad (4.4)$$

The relation between the strain and stress for an isotropic, isothermal, linear elastic material (as used in this thesis) can be written according to Hooke's law by

$$\sigma_{ij} = 2G \left(\epsilon_{ij} + \frac{\nu_p}{1 - 2\nu_p} e \delta_{ij} \right) \quad \text{with} \quad e = \epsilon_{ii} = \epsilon_{xx} + \epsilon_{yy} + \epsilon_{zz}. \quad (4.5)$$

In Eq. 4.5 G is the shear modulus, ν is the Poisson ratio and δ_{ij} is the Kronecker delta:

$$G = \frac{E}{2(1 + \nu)} \quad \delta_{ij} = \begin{cases} 0, & \text{if } i \neq j \\ 1, & \text{if } i = j \end{cases} \quad (4.6)$$

The Young's modulus E , the Poisson ratio ν and therefore the shear modulus G are characteristic constants for isotropic, linear elastic materials. The formulation of the stress strain relation can be written in its general form by

$$\boldsymbol{\sigma} = \mathbf{E} \boldsymbol{\epsilon} \quad (4.7)$$

with the algebraic stress vector according to Voigt notation

$$\boldsymbol{\sigma} = \left(\sigma_{xx} \ \sigma_{yy} \ \sigma_{zz} \ \sigma_{xy} \ \sigma_{yz} \ \sigma_{xz} \right)^T \quad (4.8)$$

and the elasticity tensor

$$\mathbf{E} = \frac{E}{(1+\nu)(1-2\nu)} \begin{pmatrix} 1-\nu_p & \nu & \nu & 0 & 0 & 0 \\ \nu & 1-\nu & \nu & 0 & 0 & 0 \\ \nu & \nu & 1-\nu & 0 & 0 & 0 \\ 0 & 0 & 0 & \frac{1-2\nu}{2} & 0 & 0 \\ 0 & 0 & 0 & 0 & \frac{1-2\nu}{2} & 0 \\ 0 & 0 & 0 & 0 & 0 & \frac{1-2\nu}{2} \end{pmatrix} \quad (4.9)$$

4.3 Equation of Motion

The equation of motion for elastic bodies can be derived using the energy method considering the displacement $u_i = u_i(x_i, t)$ and the stresses $\sigma_{ij} = \sigma_{ij}(x_i, t)$. The total potential energy V_E of a linear elastic body can be defined as the sum of the internal potential elastic energy U_E (strain energy) and the potential of the external forces W_E :

$$V_E = U_E + W_E \quad (4.10)$$

The strain energy for the elastic body can be derived by the integration of the strain energy density \hat{U}_E over the body volume:

$$U_E = \int_V \hat{U}_E dV = \frac{1}{2} \int_V \sigma_{ij} \epsilon_{ij} dV. \quad (4.11)$$

The potential of the external forces W is the sum of the punctual forces $\sum F_i$, the integration of the surface loads p_i over the body surface and the integration of the field forces f_i over the body volume (see Fig. 4.1). According to the principle of d'Alembert the equilibrium of a dynamic rigid body is reached by adding the inertial forces $\rho \ddot{u}_i dV$ for an infinitesimal mass with the acceleration \ddot{u}_i . The inertial forces act therefore as an external force and have to be included in the potential W_E . In dynamic structural problems dissipation appears in most cases due to internal or external damping forces (e.g. viscous damping). For a correct

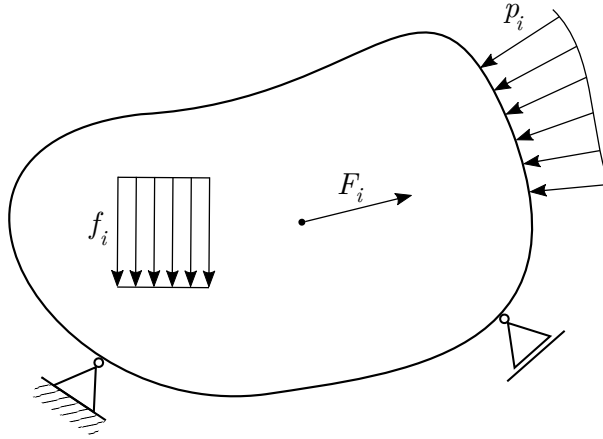


Figure 4.1: External forces acting on a solid body.

description of the dynamic behavior of a solid body dissipation has to be considered in the equation of motion. The dissipation is usually depending on the velocity of the structure \dot{u}_i . Assuming a damping distribution $c = c(x, y, z)$, the dissipation is included in the potential of the external forces, which can be finally expressed by

$$W_E = - \sum_i F_i - \int_A p_i u_i dA - \int_V f_i u_i dV + \int_V \rho \ddot{u}_i u_i dV + \int_V c \dot{u}_i u_i dV. \quad (4.12)$$

A correct damping distribution is hard to determine for complex structural problems and therefore approximation approaches are usually applied, which are discussed later.

For a body in its equilibrium state the sum of the virtual work for the internal forces δU and the external forces δW at a virtual, infinitesimal variation of the displacement δu_i is equal to zero (variation principle). Hence, the variation of the total energy potential becomes zero and V gets a minimum:

$$\delta U_E + \delta W_E = 0 \quad \rightarrow \quad \delta V_E = 0 \quad (4.13)$$

The equilibrium equation of motion for an elastic body can be finally written by

$$\int_V \rho \ddot{u}_i \delta u_i dV + \int_V c \dot{u}_i \delta u_i dV + \int_V \sigma_{ij} \delta \epsilon_{ij} dV = \sum_i F_i \delta u_i + \int_A p_i \delta u_i dA + \int_V f_i \delta u_i dV. \quad (4.14)$$

4.4 Finite Element Discretization

As the exact analytical solution of the equation of motion (Eq. 4.14) is only possible for simple geometries and load cases, approximation methods have to be used. The most common approach for structural computations is the Finite Element Method, which reduces the continuous problem of a solid body to a finite number of discrete equations. Therefore, different types of elements can be applied. In three-dimensional cases the most common ones are hexahedral and tetrahedral elements as displayed in Fig. 4.2. Hexahedral elements enable higher accuracies at low element numbers but need more discretization effort. Tetrahedral meshes have the advantage of flexible adaption even to complex geometries and can therefore be easily implemented in automatic discretization processes. The disadvantage of their lower accuracy can be compensated by using higher order interpolation functions. This is achieved by additional nodes in the elements (see Fig. 4.2, right). To obtain the displacements $\mathbf{u}^e = \begin{pmatrix} u_x^e & u_y^e & u_z^e \end{pmatrix}^T$ at any structure point (x, y, z) an approximation approach is used with the displacements of the element nodes $\mathbf{u}_i^e = \begin{pmatrix} u_{ix}^e & u_{iy}^e & u_{iz}^e \end{pmatrix}^T$ and according shape functions N_i :

$$\mathbf{u}^e = \sum_{i=1}^N N_i(x, y, z) \mathbf{u}_i^e = \mathbf{N}(x, y, z) \mathbf{U}_e \quad (4.15)$$

The vector \mathbf{U}_e is the displacement vector containing the displacements of all nodes i of a

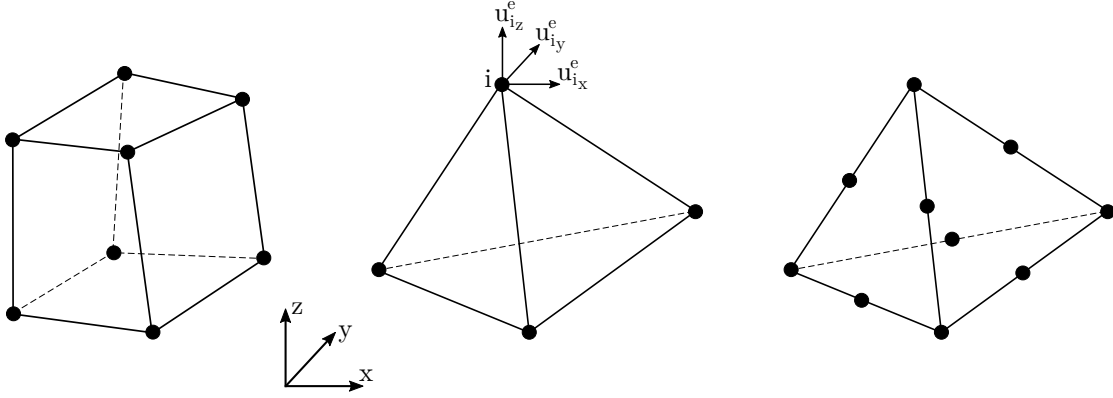


Figure 4.2: FEM discretization: Hexahedral element (left), tetrahedral element (middle) and quadratic tetrahedral element (right).

single element e and the matrix \mathbf{N} contains the individual shape functions. The approximation of the displacements using shape functions in FEM is based on the method by Ritz to describe the solution of a structural problem by analytical functions. The advantage of the discretization process is that the shape functions do not have to correspond to the overall kinematic boundary conditions, which is hard to realize, but only have to agree with the continuity terms at the boundaries of each element. Hence, the interpolation functions, which are usually of polynomial type, are more simple to achieve and similar element types can be equipped with equal shape functions.

With the basics of the linear elasticity theory the strain at any point can be calculated using the nodal displacements by

$$\boldsymbol{\epsilon} = \mathbf{d} \mathbf{N}(x, y, z) \mathbf{U}_e = \mathbf{D} \mathbf{U}_e \quad (4.16)$$

with the strain-displacement matrix $\mathbf{D} = \mathbf{d} \mathbf{N}(x, y, z)$. The stresses can be further derived using the elasticity matrix \mathbf{E} from Eq. 4.9:

$$\boldsymbol{\sigma} = \mathbf{E} \boldsymbol{\epsilon} = \mathbf{E} \mathbf{D} \mathbf{U}_e \quad (4.17)$$

4.5 Element and Global Matrix Definitions

4.5.1 Element Matrices for the Undamped System

The equation of motion for an equilibrium state of an elastic body described in Eq. 4.14 applied to a discretized system leads to a set of algebraic equations, which can be used to numerically solve the nodal displacements \mathbf{U}_e of an element e . The matrix form of the equation of motion is at first expressed for an undamped system neglecting the influence of dissipation by

$$\int_V \rho \ddot{\mathbf{u}}^e \delta \mathbf{u}^e dV + \int_V \boldsymbol{\sigma}^T \delta \boldsymbol{\epsilon} dV = \sum \mathbf{F}_e^T \delta \mathbf{u}^e + \int_A \mathbf{p}_e^T \delta \mathbf{u}^e dA + \int_V \mathbf{f}_e^T \delta \mathbf{u}^e dV. \quad (4.18)$$

The Eq. 4.15 to 4.17 lead to the relations $\delta \mathbf{u}^e = \mathbf{N} \delta \mathbf{U}_e$ and $\delta \boldsymbol{\epsilon} = \mathbf{D} \delta \mathbf{U}_e$. Thus, the matrix form of the equation of motion can be further expressed by

$$\left(\int_V \mathbf{N}^T \mathbf{N} dV \right) \ddot{\mathbf{U}}_e + \left(\int_V \mathbf{D}^T \mathbf{E} \mathbf{D} dV \right) \mathbf{U}_e = \sum \mathbf{N}^T \mathbf{F}_e + \int_A \mathbf{N}^T \mathbf{p}_e dA + \int_V \mathbf{N}^T \mathbf{f}_e dV \quad (4.19)$$

With the use of the mass matrix \mathbf{M}_e , the stiffness matrix \mathbf{K}_e and the load vector \mathbf{L}_e the time dependent, discretized equation of motion is defined by

$$\mathbf{M}_e \ddot{\mathbf{U}}_e(t) + \mathbf{K}_e \mathbf{U}_e(t) = \mathbf{L}_e(t). \quad (4.20)$$

4.5.2 Element Matrices Considering Damping

In dynamic structural problems usually a certain kind of dissipation due to damping forces appears as previously described. It can be considered in the matrix form of the equation of motion by the damping matrix \mathbf{C}_e and the velocity vector $\dot{\mathbf{U}}_e$:

$$\mathbf{M}_e \ddot{\mathbf{U}}_e(t) + \mathbf{C}_e \dot{\mathbf{U}}_e(t) + \mathbf{K}_e \mathbf{U}_e(t) = \mathbf{L}_e(t). \quad (4.21)$$

As already mentioned, a precise damping behavior for complex structural problems is usually not known in advance and the damping matrix can only be determined by experimental investigations. A common approximation approach is the so-called Rayleigh damping, which is based on the assumption that the damping can be described by the mass and stiffness distribution:

$$\mathbf{C}_e = \alpha \mathbf{M}_e + \beta \mathbf{K}_e. \quad (4.22)$$

The scalar values α and β are the mass and stiffness proportional Rayleigh damping coefficients, which are depending on the angular eigenfrequency $\omega_i = 2\pi f_i$. According to Clough and Penzien [10] the Rayleigh coefficients can be expressed using the damping ratio ξ by

$$2\xi_i = \frac{\alpha}{\omega_i} + \beta\omega_i. \quad (4.23)$$

The advantage of the Rayleigh damping approach is the uncoupled treatment of the motion equation and the simple implementation for numerical computations. On the other hand, the approximation of the global damping behavior considering two parameters is only a rough assumption.

4.5.3 Assembly of the Global Matrices

The previously described element matrices and vectors are used to define the discretized structural problem of the global system. Therefore, the individual element matrices and vectors are summed in an appropriate manner to fulfill the equilibrium conditions for each

element and between shared nodes of adjacent elements. The global displacement vector $\mathbf{U} = (\mathbf{U}_{e_1} \dots \mathbf{U}_{e_N})^T$ contains the displacement vectors for the total number of elements N . The certain element matrices are re-arranged considering the dimension of the global matrices and the position of the according nodal displacements in \mathbf{U} . Afterward, the resulting matrices are assembled to the global matrices with the assembly operator \mathbf{O} by

$$\mathbf{M} = \mathbf{O}_i \mathbf{M}_i \quad \mathbf{K} = \mathbf{O}_i \mathbf{K}_i \quad \mathbf{L} = \mathbf{O}_i \mathbf{L}_i \quad (4.24)$$

leading to the definition of the equation of motion for the complete structure:

$$\mathbf{M}\ddot{\mathbf{U}}(t) + \mathbf{C}\dot{\mathbf{U}}(t) + \mathbf{K}\mathbf{U}(t) = \mathbf{L}(t). \quad (4.25)$$

4.6 Finite Element Analysis Types

4.6.1 Static Analysis

For static structural problems the time dependent derivatives of the displacement vector $\dot{\mathbf{U}}(t)$ and $\ddot{\mathbf{U}}(t)$ can be neglected and the equation of motion reduces to the simple formulation

$$\mathbf{K}\mathbf{U} = \mathbf{L}. \quad (4.26)$$

The resulting set of linear algebraic equations with the unknown displacements can be numerically computed.

4.6.2 Modal Analysis

To obtain the natural behavior considering the mode shapes and eigenfrequencies of an undamped structure without any external forces, a modal analysis can be performed. The equation of motion can be described therefore by

$$\mathbf{M}\ddot{\mathbf{U}}(t) + \mathbf{K}\mathbf{U}(t) = \mathbf{0}. \quad (4.27)$$

Implementing the harmonic function $\mathbf{U}(t) = \boldsymbol{\phi} \sin[\omega(t - t_0)]$ with the amplitude vector $\boldsymbol{\phi}$ in the equation of motion leads to the linear eigenproblem

$$\mathbf{M}\boldsymbol{\phi} \left(-\omega^2 \sin[\omega(t - t_0)] \right) + \mathbf{K}\boldsymbol{\phi} \sin[\omega(t - t_0)] = \mathbf{0} \quad (4.28)$$

and further to

$$\left(-\omega^2 \mathbf{M} + \mathbf{K} \right) \boldsymbol{\phi} = \mathbf{0}. \quad (4.29)$$

The solution of the eigenproblem results in the eigenvalues ω_i^2 and the according eigenvectors

ϕ_i with $i = 1, \dots, N$. As N denotes to the degrees of freedom (DOF) for the discretized structure, usually a limited number of mode shapes $M < N$ is of interest and therefore computed.

4.6.3 Harmonic Response Analysis

In the case of oscillating structures excited by harmonic loads (e.g. the rotor-stator interaction in a Francis turbine), the dynamic response and amplitudes can be obtained using a harmonic response analysis (HRA). Hence, the load vector is assumed by $\mathbf{L}(t) = \mathbf{L}_0 \sin \omega_f (t - t_0)$ with the exciting frequency ω_f . The displacements are therefore also varying harmonically and can be described by $\mathbf{U}(t) = \mathbf{U}_0 \sin \omega_f (t - t_0)$ with the complex valued vector \mathbf{U}_0 . The equation of motion for the harmonic excitation of a damped structure is defined by

$$(-\omega_f^2 \mathbf{M} + i\omega_f \mathbf{C} + \mathbf{K}) \mathbf{U}_0 = \mathbf{L}_0, \quad (4.30)$$

which can be solved similar to static problems.

4.6.4 Transient Analysis

In cases of complex structural excitations with varying loads in the time domain, a harmonic response analysis is not sufficient to obtain the correct displacements, strains and stresses. If the load vector $\mathbf{L}(t)$ is known, a transient FEM analysis can be performed. Therefore, it is not only necessary to discretize the problem in space but also in time. According to the equation of motion (Eq. 4.25) the displacement \mathbf{U} , the velocity $\dot{\mathbf{U}}$ and the acceleration $\ddot{\mathbf{U}}$ are unknown. To numerically solve this unsteady problem the direct time integration method proposed by Newmark [75] can be used. Thereby, it is assumed that the displacement \mathbf{U}_n , velocity $\dot{\mathbf{U}}_n$ and acceleration $\ddot{\mathbf{U}}_n$ at the time t_n are known. By the introduction of the two parameters δ_r and γ_r the following relations for the time $t_{n+1} = t_n + \Delta t$ can be defined:

$$\mathbf{U}_{n+1} = \mathbf{U}_n + \Delta t \dot{\mathbf{U}}_n + (\Delta t)^2 \left(\frac{1}{2} - \delta_r \right) \ddot{\mathbf{U}}_n + (\Delta t)^2 \delta_r \ddot{\mathbf{U}}_{n+1} \quad (4.31)$$

$$\dot{\mathbf{U}}_{n+1} = \dot{\mathbf{U}}_n + \Delta t (1 - \gamma_r) \ddot{\mathbf{U}}_n + \Delta t \gamma_r \ddot{\mathbf{U}}_{n+1} \quad (4.32)$$

The numerical constants δ_r and γ_r are relaxation values to assure convergence and stability. They were originally proposed by Newmark [75] to $\delta_r = 0.25$ and $\gamma_r = 0.5$. By the explicit expression of $\ddot{\mathbf{U}}_{n+1}$ from Eq. 4.31 and its substitution in Eq. 4.32 the resulting functions for $\ddot{\mathbf{U}}_{n+1}$ and $\dot{\mathbf{U}}_{n+1}$ can be implemented in the equation of motion (Eq. 4.25) for the time t_{n+1} with the known load vector \mathbf{L}_{n+1} . Hence, solely the unknown \mathbf{U}_{n+1} remains in the reduced matrix problem with the form $\mathbf{Ax} = \mathbf{b}$, which can be solved consequently.

4.7 Fluid-Structure Interaction

In a large range of physical phenomena solid structures are influenced by the motion of fluids as well as in the reverse direction (e.g. airfoils, valves, turbomachines). To investigate such phenomena a so-called fluid-structure interaction (FSI) can be performed. Depending on the intensity of the influence between the solid and fluid domain, different approaches exist with varying computational effort, which are briefly described below.

4.7.1 Bidirectional Coupling

In the case of a strong influence of the fluid motion on the behavior of a solid body and in the reverse direction, a two-way coupling approach has to be used. This is necessary for thin and flexible structures with large deformations, which additionally modify the fluid flow. For the bidirectional coupling approach the direct connection of both discretized domains is necessary and the interaction between them has to be solved for each numerical time step. Although it enables the most accurate results, an increased computational effort is required. Two methods exist within the bidirectional coupling:

- Monolithic approach: The fluid and the structure fields are computed simultaneously before updating the meshes and proceeding to the next time step. It requires matching meshes at the domain interfaces, which is hard to achieve for complex geometries, and is also less stable.
- Partitioned approach: The fluid and the structure fields are solved consecutively. Hence, non-matching meshes can be applied but this requires according coupling approaches for the exchange of data.

4.7.2 Unidirectional Coupling

If the influence of the solid motion on the fluid can be neglected or for a minor impact of the fluid motion to a solid body, a one-way or unidirectional coupling is sufficient. This is the case in the field of hydraulic turbomachines, where the pressure of the flow has a major impact on the structural behavior of the runner but the small appearing displacements hardly affect the fluid motion. Therefore, the flow field, which is dominant, can be separately solved by CFD and the pressure distribution can be applied as boundary condition to the FEM simulation. The advantage is a reduced numerical effort at a simultaneously marginal loss of accuracy by neglecting the influence of the solid structure to the fluid motion. Hence, this approach is used in the scope of this thesis. According investigations on Francis turbine runners have been done by Coutu et al. [15], Flores et al. [27], Guillaume et al. [37] or Seidel et al. [86].

4.7.3 Fluid Added Mass Effect

As Francis turbine runners are surrounded by water during operation, not only the pressure distribution has an influence on the structure but also the additional mass. Several investi-

gations deal with this added mass effect and extended simulation approaches using acoustic fluid finite elements have been introduced by Guillaume et al. [37], Hübner et al. [44] or Liang et al. [56]. Graf and Chen [36] and Lais et al. [51] did experimental and numerical research on the natural mode shapes and eigenfrequencies of Francis runners revealing a considerable impact of the surrounding water volume. Although they obtained an accurate agreement between measurements and simulations using acoustic fluid elements, the numerical model includes several simplifications and assumptions, which do not correspond to the physical behavior in hydraulic turbines:

- The viscosity of the fluid is neglected
- The fluid is slightly compressible - pressure variations lead to density changes
- There is no mean fluid flow
- Only small variations of the mean pressure and mean density appear

Considering those simplifications, the conservation law for the momentum can be reduced to

$$\frac{\partial(\rho c_i)}{\partial t} = -\frac{\partial p}{\partial x_i}. \quad (4.33)$$

For small variations of the pressure and density the relation $\partial p / \partial \rho = a^2$ can be defined with the fluid sound of speed a . Further, the acoustic wave equation is derived using the simplified momentum equation and the mass conservation:

$$\frac{\partial^2 p}{\partial x_i^2} = \frac{1}{a^2} \frac{\partial^2 p}{\partial t^2}. \quad (4.34)$$

The acceleration of the solid structure and the normal pressure gradient of the fluid at the interface are used to couple both domains. The discretized equations for the fluid-structure interactions can be finally described by the following matricial system:

$$\begin{pmatrix} \mathbf{M}_s & \mathbf{0} \\ \mathbf{M}_{fs} & \mathbf{M}_f \end{pmatrix} \begin{pmatrix} \ddot{\mathbf{U}} \\ \ddot{\mathbf{P}} \end{pmatrix} + \begin{pmatrix} \mathbf{C}_s & \mathbf{0} \\ \mathbf{0} & \mathbf{C}_f \end{pmatrix} \begin{pmatrix} \dot{\mathbf{U}} \\ \dot{\mathbf{P}} \end{pmatrix} + \begin{pmatrix} \mathbf{K}_s & \mathbf{K}_{fs} \\ \mathbf{0} & \mathbf{K}_f \end{pmatrix} \begin{pmatrix} \mathbf{U} \\ \mathbf{P} \end{pmatrix} = \begin{pmatrix} \mathbf{L}_s \\ \mathbf{0} \end{pmatrix} \quad (4.35)$$

Thereby, \mathbf{M}_s , \mathbf{C}_s and \mathbf{K}_s are the structural mass, damping and stiffness matrix. \mathbf{M}_f , \mathbf{C}_f and \mathbf{K}_f are the equivalent acoustic fluid mass, dissipation and stiffness matrix. \mathbf{M}_{fs} and \mathbf{K}_{fs} are the coupling mass and stiffness matrix at the interface. \mathbf{U} is the displacement vector, \mathbf{P} the pressure vector and \mathbf{L}_s is the load vector. A detailed derivation of Eq. 4.35 is described by Magnoli [61] or Liang et al. [56].

Chapter 5

Fatigue of Structures

The static and dynamic excitation of mechanical structures at a relevant number of load cycles leads to crack initiation and propagation and further to fatigue damages. To prevent such critical failure events appropriate prediction methods have to be used to obtain the structural loads and critical locations of mechanical components. The basic concepts of the fatigue theory for mechanical structures, which are used in the scope of this thesis, are described in this chapter. For a more detailed description one is referred to Haibach [39].

5.1 Influences on the Structural Fatigue

The main influence on the fatigue of mechanical structures are varying stresses σ along the time t . The characteristic values for a typical load cycle N like the mean stress σ_m , the stress amplitude σ_a , the maximum stress σ_{max} and the minimum stress σ_{min} are displayed in Fig. 5.1 left.

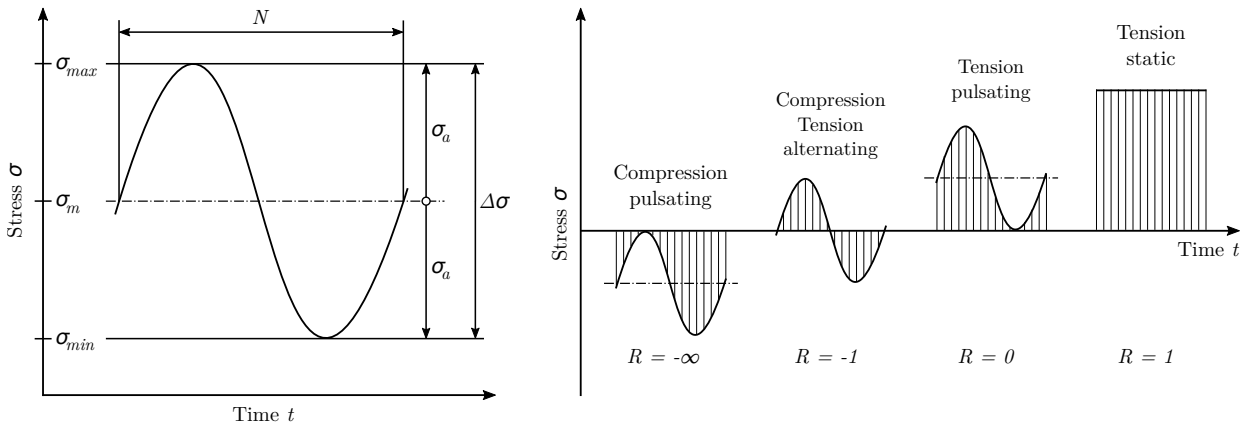


Figure 5.1: Characteristic values of alternating stresses (left) and different load cases (right). Graphics based on Haibach [39].

Depending on the stress ratio $R = \sigma_{min}/\sigma_{max}$ different load cases can be distinguished between the tensile and compressive area (see Fig. 5.1 right). For $R = 1$ the appearing stress

is static along the time and the yield strength σ_y and the ultimate tensile strength σ_u are the limiting values for linear elastic materials. The yield strength defines the transition from the linear stress-strain behavior described by Eq. 4.7 to the plastic regime with a remaining structural deformation (see Fig. 5.2 left). The ultimate tensile strength determines the maximum stress of a material before fracture occurs. For cyclic loads with a ratio of $R \neq 1$ the failure of structures usually appears at stress amplitudes below the yield strength. To obtain the relation between the number of load cycles N , which a material withstands at a certain stress ratio and level, experimental investigations are performed with defined specimens. The results lead to the so-called S-N or Wöhler curves (see Fig. 5.2 right). Those experiments usually reveal a statistically distributed failure probability and the S-N curves are therefore expected values with a defined uncertainty range. Three main areas can be distinguished for the S-N curve according to the stress level and the number of load cycles:

- The static or low cycle fatigue (LCF) range above the yield strength σ_y . In this area the macroscopic elasto-plastic deformations are mainly influencing the fatigue. According to the load cycles this area is usually defined by a number of $N < 10^4$.
- The high cycle fatigue (HCF) range below the yield strength and at $N > 10^5$. In this area no macroscopic plasticity occurs and the elastic material behavior is crucial.
- The fatigue endurance (FE) range below a certain stress level defined as the fatigue limit σ_l , where no failure appears even at very high load cycles.

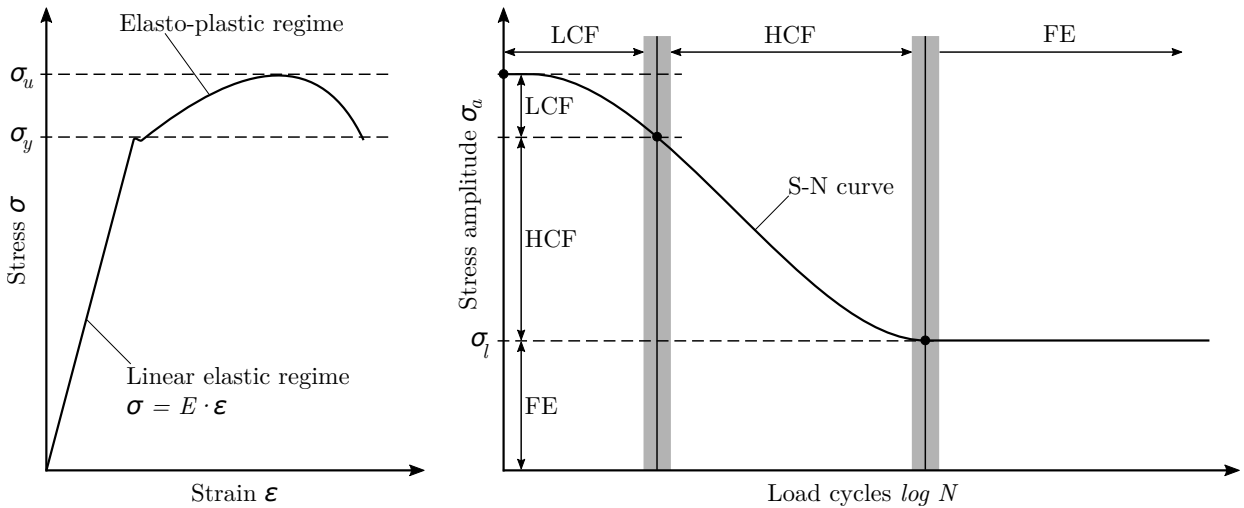


Figure 5.2: Stress-strain behavior (left) and typical S-N curve (right) of a linear-elastic material. Graphics based on Haibach [39].

The S-N curve displayed in Fig. 5.2 is typical for steel alloys. For other materials like aluminum alloys no evident fatigue limit exists and the S-N curve decreases further with increasing load cycles N . This may also be the case for steel alloys influenced by corrosion. In addition to the stress amplitude σ_a the mean stress σ_m and therefore the stress ratio R

have an impact on the fatigue life as well. This relation can be described by the so-called Haigh [40] diagram (see Fig. 5.3). It is obtained by different S-N curves at varying mean stresses σ_m . For each combination of σ_m and σ_a the related number of load cycles until failure can be assessed using the Haigh diagram. It is visible that the acceptable stress amplitude at a certain number of load cycles N is decreasing with an increasing mean stress.

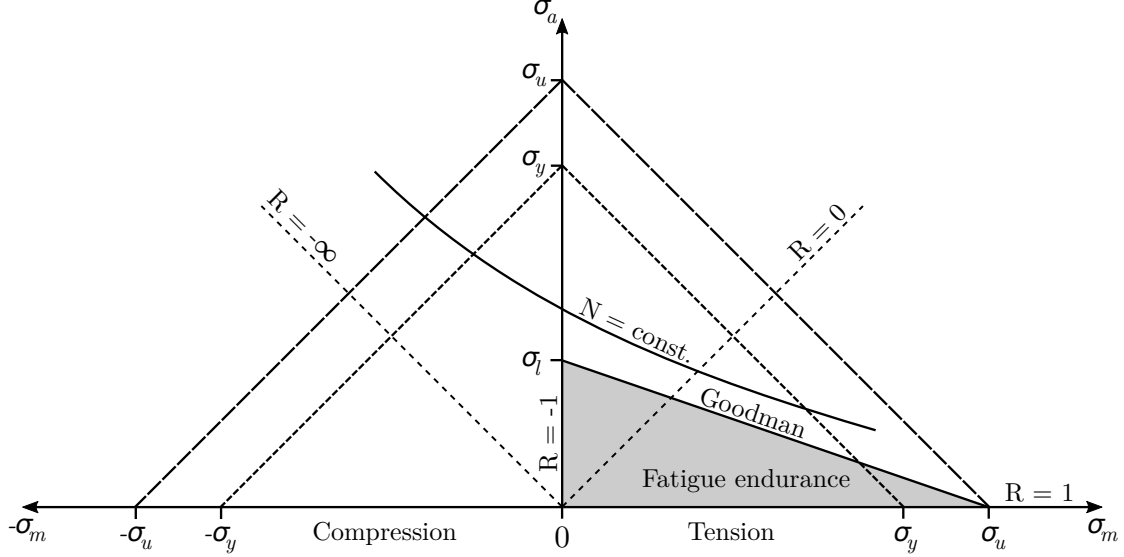


Figure 5.3: Haigh diagram for a linear-elastic material. Graphics based on Haibach [39].

A simple approach to obtain the acceptable stress amplitude in the fatigue endurance range for a mean stress in the tensile region is the approximation proposed by Goodman [35]. Thereby, the allowable stress amplitude σ_a at a certain mean stress σ_m is assumed using the fatigue limit σ_l and the ultimate tensile strength σ_u by the linear relation

$$\sigma_a = \sigma_l \left(1 - \frac{\sigma_m}{\sigma_u} \right). \quad (5.1)$$

To evaluate the fatigue life with an S-N curve obtained at the stress ratio $R = -1$, the stress amplitudes σ_a in the range of $-1 < R < 1$ with $\sigma_m > 0$ can be corrected to the according value σ_0 with $\sigma_m = 0$ by the Goodman approach:

$$\sigma_0 = \sigma_a \left(1 - \frac{\sigma_m}{\sigma_u} \right)^{-1}. \quad (5.2)$$

5.2 Complex Load Histories

In most mechanical applications, the structures are excited by complex load histories with varying mean stresses σ_m and stress amplitudes σ_a at different number of cycles N . As the S-N curves are obtained for certain values of σ_m and σ_a an appropriate method to combine the multiple loads has to be used. One approach is the concept of fatigue damage

accumulation proposed by Palmgren [78] and Miner [69]. The main idea is that a certain mean stress σ_{m_i} and stress amplitude σ_{a_i} cause a fatigue damage $D_i = n_i/N_i$ with the occurring load cycles n_i and the fatigue limit N_i . The total fatigue damage factor C can be therefore obtained by

$$C = \sum_{i=1}^m D_i = \sum_{i=1}^m \frac{n_i}{N_i}. \quad (5.3)$$

The acceptable value for C depends on the material and manufacturing process but in most cases the criterion for a structure to resist fatigue failure is $C \leq 1$.

To apply the fatigue damage accumulation defined in Eq. 5.3 the number of load cycles n_i at a certain stress amplitude σ_{a_i} must be known. For complex dynamic loads the variation of the stresses along the time do not follow simple analytical functions. In most cases the load histories belong to a stochastic behavior, which cannot be assessed directly for a fatigue analysis. In order to evaluate the impact of such complex load cycles, counting algorithms have to be used. The most common approach, which is presently used in many structural applications, is the so-called rainflow cycle counting method proposed by Matsuishi and Endo [64]. The algorithm can be explained considering a stochastic stress-time signal as displayed in Fig. 5.4: The cycles are counted using a fictitious raindrop, which flows down the sides of the signal if it is rotated clockwise 90° , like on a roof.

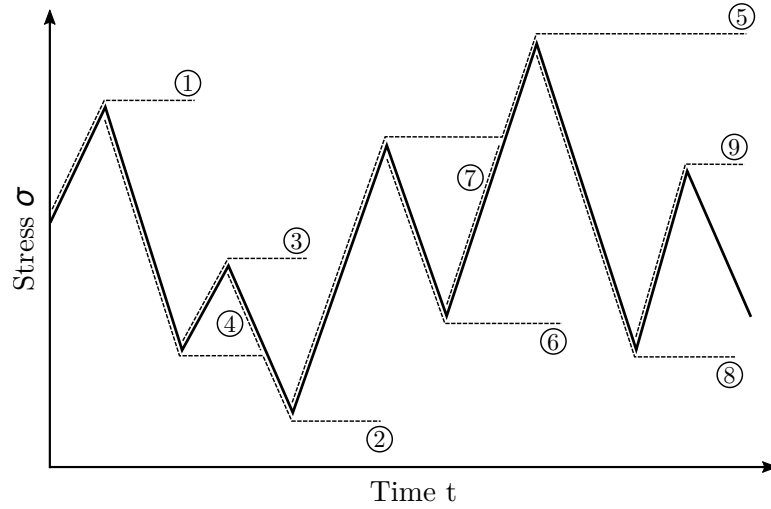


Figure 5.4: Rainflow cycle counting algorithm.

Each raindrop starts either at a tensile peak or at a compressive valley. A half cycle is counted if

- a raindrop reaches the end of the time history,
- a flow merges with an earlier flow from a bigger tensile peak or a smaller compressive valley,
- a flow merges with a following flow from a bigger tensile peak or a smaller compressive valley.

The stress difference of each half cycle determines its range and half cycles with the same range but opposite sense can be paired up to full cycles. The resulting load spectra can be further used for the fatigue analysis.

5.3 Elasto-plastic Behavior

In normal operating conditions of hydraulic turbomachines the appearing strains and stresses are in the linear elastic or HCF range and the previously described fatigue approaches are valid. During start-stop operation or high pressure loads induced by a water hammer¹ as described by Huth [45], the stresses may exceed the yield strength σ_y and the elasto-plastic or LCF behavior is essential. This may also occur for high residual stresses due to manufacturing processes (e.g. welding). In this regime even small stresses lead to large strains in the structure. Hence, modified fatigue models have to be considered like the method based on the investigations by Coffin [11], Manson [63] and Morrow [73]. Therefore, the strain amplitude in the elasto-plastic range can be derived by

$$\epsilon_a = \frac{\sigma'_f}{E}(2N_f)^b + \epsilon'_f(2N_f)^c = \epsilon_{a,e} + \epsilon_{a,p} \quad (5.4)$$

with the fatigue strength coefficient σ'_f , the fatigue strength exponent b , the fatigue ductility coefficient ϵ'_f and the fatigue ductility exponent c . Those parameters are experimentally observed material data. The elasto-plastic model is therefore the sum of the elastic deformation $\epsilon_{a,e}$ described by the first term in Eq. 5.4 and the plastic deformation $\epsilon_{a,p}$ described by the second term. This correlation is displayed as well in Fig. 5.5 (left) in relation to the fatigue life in the elasto-plastic regime N_f . During repeating deformation processes in the plastic range the stress-strain relation is usually affected by hysteretic effects, with an increase or decrease of the material strength (see Fig. 5.5 right). In order to obtain the correct stresses considering this hysteresis the following stress-strain formulation is appropriate:

$$\frac{\epsilon}{2} = \frac{\sigma}{2E} + \left(\frac{\sigma}{2K'} \right)^{\frac{1}{n'}} \quad (5.5)$$

The cyclic strength coefficient K' and the cyclic strain hardening exponent n' are material properties.

The elasto-plastic fatigue approach can be applied even if only high cycle fatigue loads with stress amplitudes below the yield strength appear. Thereby, the plastic deformations in Eq. 5.4 become negligible and the elastic term is significant.

5.4 Multiaxial Load Conditions

In most structural applications the mechanical loads do not belong to a uniform direction but usually to a combination of shear and normal stresses. An approach to consider those

¹Pressure surge induced for example by a suddenly closed valve.

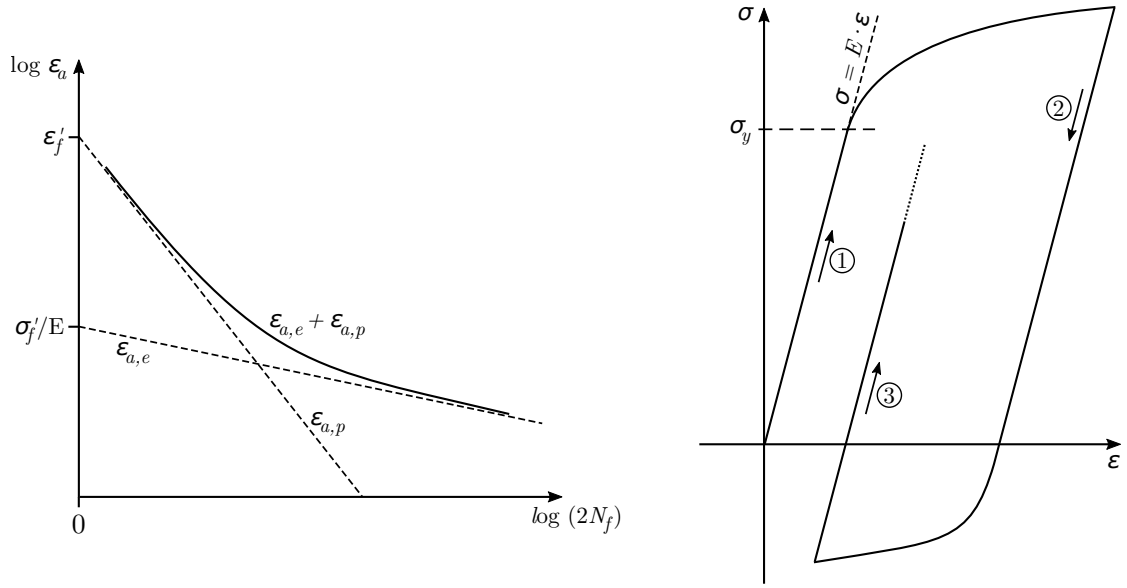


Figure 5.5: Fatigue life relation (left) and stress-strain hysteresis in the elasto-plastic regime (right). Graphics based on Magnoli [61]

multiaxial conditions for a correct fatigue analysis is the method proposed by Brown and Miller [7], [68]. Therefore, an equivalent shear strain γ_e can be derived by the cyclic shear strain γ_{max} on the maximum shear strain plane and the according normal strain ϵ_n :

$$\frac{\gamma_e}{2} = \frac{\gamma_{max}}{2} + S \epsilon_n \quad (5.6)$$

The normal strain coefficient S is a material dependent parameter. In order to consider multiaxial loads for fatigue damages the strain-based algorithm can be applied using Eq. 5.4 by

$$\frac{\gamma_e}{2} = A \frac{\sigma_f'}{E} (2N_f)^b + B \epsilon_f' (2N_f)^c \quad (5.7)$$

with the coefficients $A = (1 + \nu) + S(1 - \nu)$, $B = (1 + \nu_p) + S(1 - \nu_p)$ and the plastic Poisson ratio ν_p . The stress-based damage parameter can be further derived using an equivalent shear stress τ_e , the maximum shear stress on the critical plane τ_{max} and the normal stress σ_n :

$$\frac{\tau_e}{2} = \frac{\tau_{max}}{2} + S \sigma_n = E \left(A \frac{\sigma_f'}{E} (2N_f)^b + B \epsilon_f' (2N_f)^c \right) \quad (5.8)$$

An extended approach of the rainflow counting algorithm using the stress-based Brown-Miller approach to consider multiaxial stress states for a fatigue analysis has been proposed by Wang and Brown [102, 103].

Chapter 6

Numerical Approach

6.1 Paper 1

In the first paper (see Tab. 6.1) the numerical approach for the lifetime investigations of a high head Francis turbine is described. It deals with the overall method based on unsteady CFD simulations and different FEM computations. The prototype site measurements performed on the according Francis turbine are described and the results of the appearing stresses are discussed. Further, the numerical setup for the CFD simulations is explained considering the computational domains, the discretization and the setup for OpenFOAM. A grid independence study, performed on three different mesh densities, is used to assess the numerical error induced by the finite cell number. The setup for the static FEM simulations using Code_Aster is further described considering the cyclic sector model of the high head runner. To evaluate the natural mode shapes and the according eigenfrequencies of the turbine the modal analysis including the surrounding water volume is discussed. As the rotor-stator interaction has a major impact on the dynamic excitations of high head Francis runners, the approach for the harmonic response analysis is described. At the end, the influencing factors for a fatigue assessment of hydraulic turbomachines are discussed. The substantial contribution of this paper has been done by the co-author Markus Eichhorn, which includes the evaluation of the measurement results as well as the implementation of the numerical CFD and FEM simulations.

Table 6.1: Notes on Paper 1.

Title	An Approach to Evaluate the Lifetime of a High Head Francis Runner
Authors	E. Doujak, M. Eichhorn
Conference	International Symposium on Transport Phenomena and Dynamics of Rotating Machinery (ISROMAC 2016)
Location	Honolulu, Hawaii, USA
Date	April 10-15, 2016

An Approach to Evaluate the Lifetime of a High Head Francis Runner

Eduard Doujak^{1*}, Markus Eichhorn¹



Abstract

Nowadays, the electricity market is changing rapidly and the requirements for hydropower plant operators vary between base load electricity production and ancillary services with a high share of transient operational points. The institute for Energy Systems and Thermodynamics, together with partners from the industry, initiated a research project to investigate the effects of these new operational modes on the components of a hydraulic machine. Especially the runner is of high importance due to the long service time and unfavorable flow phenomena when operated at off design points. A method to evaluate the lifetime of a high head Francis runner should be developed to investigate the existing runner and to serve later on a possible procedure for the design stage. Therefore, prototype measurements with applied strain gauges have been carried out for validation purposes of the developed method. Unsteady Numerical flow simulations using the open-source software OpenFOAM and static as well as dynamic Finite Element calculations with Code Aster are performed to investigate the lifetime of the observed Francis runner. The research project is still ongoing but first results regarding the procedure and the methods will be shown in this paper.

Keywords

Francis Runner — Fluid-structure interaction — Strain gauge measurements — Lifetime investigation

¹Institute for Energy Systems and Thermodynamics, Research Group Fluid-Flow Machinery, TU Wien, Vienna, Austria

*Corresponding author: eduard.doujak@tuwien.ac.at

INTRODUCTION

The history of the European electricity market shows over the past twenty years a more and more changing behavior. Drivers for this changing situation are manifold. At the beginning opening and liberalization of the market caused a lot of uncertainty and an investment stop into new hardware. This change had more impact on the economical than on the technical side. One of the next important key points in the development was the implementation of the Kyoto protocol by 2005 aiming to reduce CO₂ emissions around the world. At around that time all around Europe new incentives to promote renewable energy sources like wind or solar have been established. Many countries followed the fed-in tariff system to encourage investors to build new electricity supplier by using renewable energy sources. Additionally to these increasing installations of small power production units, Germany decided to shut down their nuclear power stations within the next twenty years. These activities had a big impact on technical as well as on economical aspects. Side effect of this electricity market change was paradoxically an increased investment in Hydro power as well, because load dispatchers needed storage and grid control capabilities. And the consequences of these market changes are even today remarkable.

Today we are dealing with faster response time at the electro-mechanical units in our Hydro power plants as well as some kind of standby operation, which means that the units are running for hours at very low load conditions and far away from the design point. Some resulting effects have already been published [1], showing the general effect of

increased fluctuating sources of energy. The requirements of Hydro power plants are nowadays more and more to deliver regulating power and ancillary services to the electrical grid, which results in higher dynamic loads and stresses on turbine components. These dynamic stresses can be of the steady-state or transient type, deterministic or stochastic.

The expected flexibility of turbine operation is characterized by more unit start-stop cycles, part load operation for power regulation and less steady state operation at the nominal point. All different modes have a strong influence on the flow conditions within the machine itself and cause a known variation of flow phenomena. Francis runners at part load operation are for example dominated by rotor-stator interaction (RSI) and by draft tube instabilities (DTI) having some harmonic excitation effects. Whereas vortex shedding effects (VSE) at low load conditions show a more stochastic pattern and non harmonic behavior. At start-stop cycles the machine unit runs through all these phenomena with additional effects of speed-no-load (SNL) condition. Sometimes, the hydraulic unit also runs in synchronous condenser operational mode in air, which means that the synchronized unit has to be dewatered with compressed air causing high stochastic stresses.

In the past, computational resources haven't been high enough to investigate all these transient phenomena on the total hydraulic unit. Singular parts have been numerically computed by means of Computational Fluid Dynamics (CFD). The numerical results have been evaluated with measurements but there was still a lack of uncertainties at the boundaries.

An Approach to Evaluate the Lifetime of a High Head Francis Runner — 2/10

Most of the time the best information about the behavior of Francis runners have been gained by interpreting prototype measurements like published by [2]. Slowly, the computational resources raised to a range to calculate dynamic stresses on single parts of the hydraulic unit, mostly the Francis runner as shown in [3]. At that point, fluid-structure interaction (FSI) at the total hydraulic unit was big task. Major efforts have been made over the past five years to close this gap and to predict flow phenomena and pressure pulsations as basic for dynamic stress calculations by means of CFD. The way of investigating the impact of flexible operation on Francis runners was published at [4] but still relies on measurement basis. As prototype measurements are very expensive the goal of today is to provide basic information for a lifetime investigation of a runner by numerical simulations.

Lifetime investigation of hydraulic parts is not only dominated by calculating static mean stresses but is more and more a task of fatigue analysis. Especially dynamic loads seek for this kind of analysis as shares of low-cycle fatigue (LCF) and high-cycle fatigue (HCF) have to be managed. Some selected publications about this topic show the state of the art and problems in defining the life expectancy of a Francis runner. In 2005 a fatigue design of hydraulic turbine runners has been published by [5]. Five years later [6] determined the impact of start-up scheme on Francis runner life expectancy. Recent publications [7] or [8] show the importance of this approach for turbine runners.

The following paper gives an overview about a method to investigate the lifetime of a high head Francis runner by discussing all necessary steps and numerical tools on the one hand and processing of prototype measurements on the other hand.

1. METHOD

The following method was developed within a large research project to investigate a high head Francis turbine with a specific speed of $n_q \approx 24 \text{ min}^{-1}$ under different operating conditions. Goal of this study is the evaluation of the lifetime of the turbine runner using numerical calculations as well as site measurements. As mentioned above, the approach is nearly similar to already known procedures unless the operating point is far away from the nominal point and more or less at the region of irregular flow pattern causing stochastic dynamic stresses. Within the research project, prototype measurements using strain gauges applied to the runner have been performed to validate the numerical results.

Figure 1 shows the procedure for the runner lifetime investigation, which consists of the following numerical tasks:

- Transient CFD calculations
- Static Finite Element (FE) calculations
- Modal analysis
- Harmonic response analysis

At the measurement path the following tasks have to be considered:

- Prototype site measurements
- Stress extrapolation using FE-methods
- Rainflow counting analysis

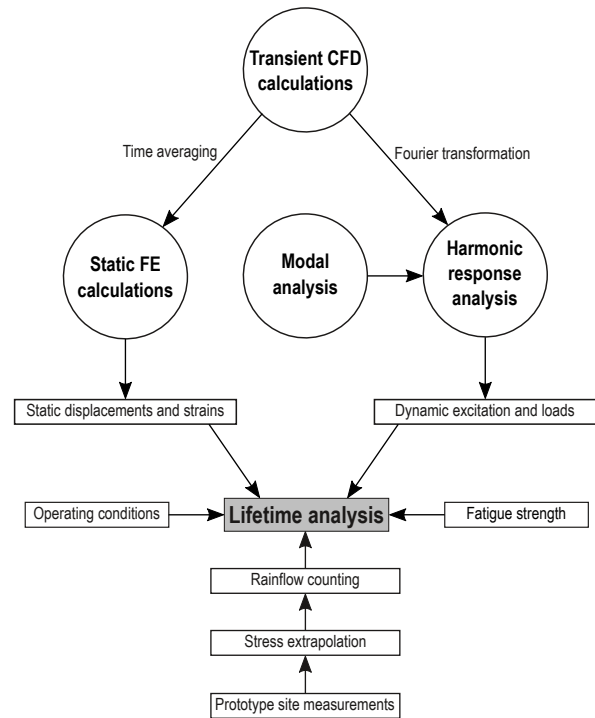


Figure 1. Numerical and measurement procedure for Francis runner lifetime investigation

As University resources are mostly limited, one additional point of investigation is the usability of open source software. In this case OpenFOAM 2.3 was selected for the transient CFD calculations and Code Aster 11.7 for the subsequent tasks of the structural Finite Element calculations.

2. PROTOTYPE SITE MEASUREMENTS

2.1 Measurement Setup

To evaluate the static and dynamic stresses appearing on the Francis runner in different operating conditions, prototype site measurements have been performed. Therefore, eight strain gauges have been attached to the suction side (SS) and pressure side (PS) of the trailing edge of one turbine blade (see figure 2 left). Due to manufacturing tolerances, geometric differences appeared among the 15 runner blades. To acquire the maximum stresses, the blade with the thinnest trailing edge has been chosen for the strain gauge measurements. The exact geometry has been measured using a 3D measurement arm to increase the accuracy of the results for the numerical calculations. Thereby also the positions of the strain gauges have been included in the Computer Aided Design (CAD) model.

An Approach to Evaluate the Lifetime of a High Head Francis Runner — 3/10

The data of the strain gauges during turbine operation has been recorded using a data logger, which has been mounted to the shaft inside the draft tube of the machine (see figure 2 right).

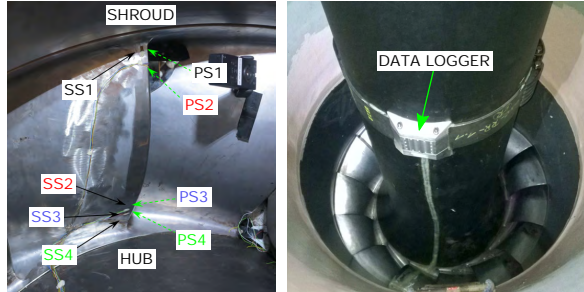


Figure 2. Positions of the strain gauges applied to one runner blade (left) and data logger (right)

Additionally, to validate the CFD simulations, the operating parameters such as head, output power, guide vane opening, pressure in the spiral casing and draft tube, have been recorded during the measurements. The vibration of the shaft as well as the acceleration of the shaft bearing in radial direction have been recorded to further investigate the overall behavior of the machine. The data of the strain gauges have been measured using a sampling rate of 1 kHz, the other parameters with a sampling rate of 2.4 kHz.

2.2 Results

The measurements were performed in different operating points from the start-up in steps of 10 MW respectively 20 MW to the maximum output power of 180 MW and back again. At the end of the normal turbine operation, the water was drained from the machine to measure the strains on the runner due to the centrifugal forces without any hydraulic pressure (Rotation). These conditions are used for an evaluation of the Finite Element calculations. The results of the strain gauge measurements on the suction side are displayed in figure 3. The strains for SS1 are nearly constant with varying operating conditions, whereas the strains for SS2 and SS3 are changing from compression in low and part load to tension in high and full load conditions. The results for the strain gauge SS4, which was located close to the radius between the blade and the hub of the runner, show an opposing behavior.

The Fourier transformation of the time signal for the strain gauge SS2 reveals a dynamic excitation of the runner at the first and second harmonic of the blade passing frequency f_{BP} in each operating point (see figure 4). This excitation is induced by the rotor-stator interaction (RSI) between the runner (RN) and the guide vane (GV) domain and is the main impact to runner fatigue for high head Francis turbines (see [9] and [10]). The blade passing frequency is described by

$$f_{BP} = Z_g \cdot f_0 \quad (1)$$

with the number of guide vanes $Z_g = 20$ and the rotating frequency f_0 of the machine. In low load conditions the strains

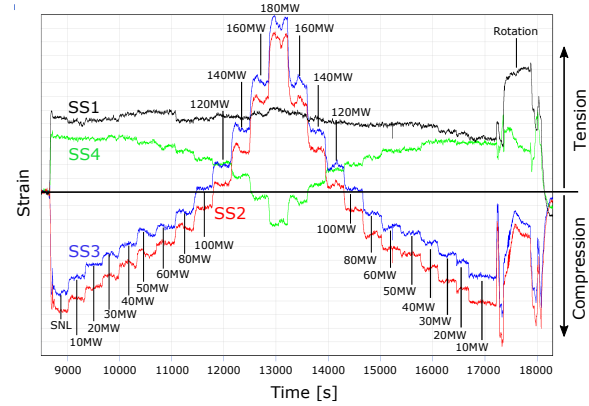


Figure 3. Results for the strain gauges applied to the suction side of one runner blade

and therefore the pressure pulsations show a more stochastic behavior, although the RSI remains the dominant dynamic influence. At the operating point with an output power of one third of the maximum power, a high peak appears in the low frequency regime which could be an indicator for different flow phenomena like draft tube vortex or trailing edge vortex shedding. The amplitudes at the rest of the signal are also even higher. This operating area will therefore be of special interest for future simulations but for the current presentation of the method of runner lifetime investigation the RSI will be discussed further.

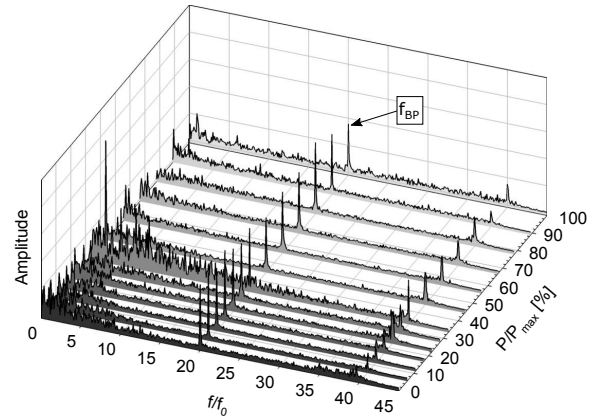


Figure 4. Frequency spectrum of strain gauge SS2 in different operating conditions

The next steps towards the runner lifetime analysis would be the stress extrapolation for the strain gauge measurement points to the location with the highest stresses and the rainfall counting analysis. These two points will not be discussed further here due to limited paper length and as they are general steps of a fatigue analysis and not specially associated with hydraulic runner fatigue assessment. The complementary parts of runner lifetime analysis will be discussed at chapter 4.

3. NUMERICAL INVESTIGATIONS

3.1 CFD calculations

3.1.1 Numerical model

To calculate the fluctuating pressure field induced by the rotor stator interaction, unsteady numerical flow simulations using the Reynolds averaged Navier-Stokes (URANS) equations are performed with OpenFOAM 2.3. This is a suitable approach for steady operating conditions with a slight amount of turbulence and vorticity (see [11]). In part load and especially no load conditions, stochastic flow phenomena like vortex shedding or draft tube instabilities are increasing (as shown in figure 4) and turbulence modeling has a large influence on the dynamic behavior (see [12] or [13]). Therefore, the application of the SAS turbulence model with OpenFOAM will be investigated in future publications for the CFD calculations in part load conditions.

The model for the CFD simulation consists of the spiral casing, 10 stay vanes, 20 guide vanes, the runner with 15 blades and the draft tube (see figure 5).

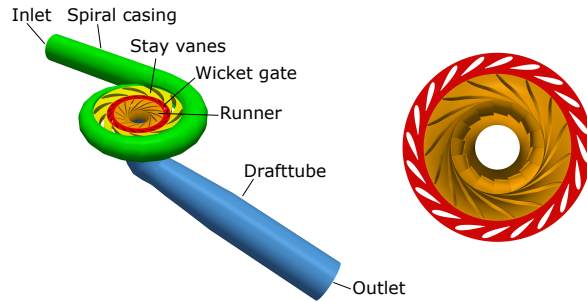


Figure 5. Computational domains for CFD simulations (left: entire machine; right: guide vanes and runner)

Table 1. Setup for the CFD calculations

Parameters	Description
Software	OpenFOAM 2.3
Analysis type	Transient rotor-stator
Time step	0.36 degrees ($1.0e^{-4}$ s)
Simulation time	10 runner rotations (1.0 s)
Inlet BC	Mass flow rate
Outlet BC	Average static pressure
Reference pressure	0 kPa
Interfaces	Arbitrary mesh interface
Turbulence model	k- ω SST
Advection scheme	Second order
Transient scheme	Second order backward Euler
Max. Courant number	≤ 15

The calculations are performed in different operating points from the maximum output power of 180 MW to low load conditions, according to the prototype site measurements described in section 2. The parameters of the hydraulic

machine (e.g. head H , runner torque T , efficiency η) are compared to evaluate the accuracy of the used setup. The simulations for full and high load conditions are done using the two-equation turbulence model k- ω SST. The time step for the CFD simulations at the different operating conditions is chosen to 0.36 degrees, which yields a maximum Courant number of $Co_{max} \leq 15$. To gain enough data for the Fourier transformation of the unsteady pressure field, at least ten runner rotations are simulated. The setup and the boundary conditions for the numerical flow simulations are summarized in table 1.

3.1.2 Discretization

The computational model is spatially discretized in a multi-block hexahedral grid using Ansys ICEM 15.0. The particular domains are meshed separately and the interfaces are connected using the arbitrary mesh interface (AMI) implemented in OpenFOAM 2.3 (see figure 6). The number of nodes and the quality of the mesh with a total number of about 5.9 million nodes are displayed in table 2.

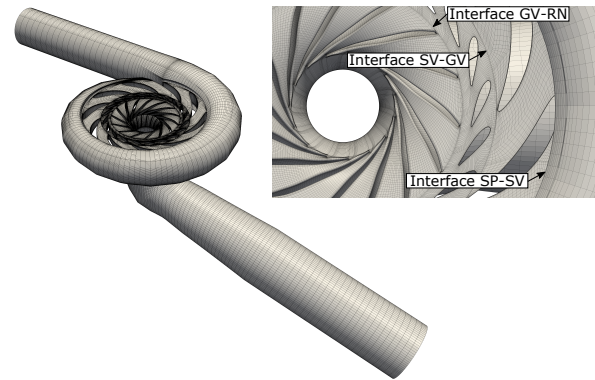


Figure 6. Discretization and interfaces between CFD domains

3.1.3 Grid independence study

In order to estimate the uncertainties due to the discretization of the CFD model, a grid independence study is performed according to the approach of [14]. Therefore, the fluid domains of the Francis turbine, including the spiral casing, the stay vanes, the wicket gate, the runner and the draft tube are considered. The mesh is refined in three different stages (coarse - G3, medium - G2, fine - G1) regarding the grid size h , which is calculated by

$$h = \left[\frac{1}{N} \sum_{i=1}^N (\Delta V_i) \right]^{1/3} \quad (2)$$

with the total number of cells N and the volume of the i th cell ΔV_i . The refinement factor $r_{21} = h_{medium}/h_{fine}$ for the fine grid respectively $r_{32} = h_{coarse}/h_{medium}$ for the medium

Table 2. Parameters for the discretization

Parameters	Spiral casing	Stay vanes	Guide vanes	Runner	Draft tube	Full mesh
Number of cells N	599,556	723,444	1,688,000	2,568,360	298,128	5,877,488
Min. determinant	0.28	0.36	0.69	0.21	0.33	-
Min. angle	11	16.1	22.5	18.6	18.9	-
Min. aspect ratio	0.001	0.001	0.002	0.002	0.015	-
y_{mean}^+	95	50	65	70	60	-

grid is therefore considered to be greater than 1.3. The mesh refinement of the structured grid is done consistent in all three directions with a constant resolution of the wall boundary layer according to $30 \leq y_{mean}^+ \leq 100$. The convergence of the grid independence study is verified by computing different parameters Φ of the Francis turbine at the operating point with maximum output power for all three meshes. These values are the head H , the runner torque T and the efficiency η . Therefore, the SIMPLE-algorithm of OpenFOAM, which calculates the steady-state pressure-velocity coupling, is used. The extrapolated values for the head, the torque and the efficiency for a mesh with grid size $h_n = 0$ are calculated by

$$\Phi_{ext}^{21} = \frac{r_{21}^p \Phi_1 - \Phi_2}{r_{21}^p - 1} \quad (3)$$

with the order of accuracy p computed according to [14]. The numerical uncertainty is considered by calculating the relative error e_a^{21} for the fine grid by

$$e_a^{21} = \left| \frac{\Phi_1 - \Phi_2}{\Phi_1} \right| \quad (4)$$

and the grid convergence index GCI by

$$GCI_{21} = \frac{1.25 \cdot e_a^{21}}{r_{21}^p - 1} \quad (5)$$

These are similarly calculated for the medium and the extrapolated grid. The description and results for the grid independence study are displayed in table 3 and figure 7.

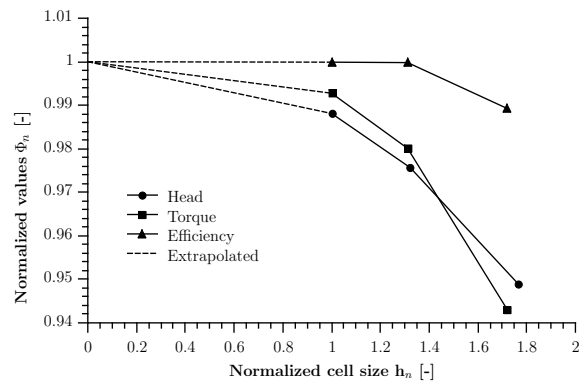
The results of the grid independence study reveal a monotonic convergence for all three parameters with a decreasing grid size h_i and small deviations for the GCI from the asymptotic value. Considering the computational costs and the accuracy for the unsteady CFD simulations, the medium grid with a normalised size of $h_{2,n} = 1.32$ (as described in 3.1.2 and table 2) is used for further investigations.

3.1.4 CFD Results

The following results are performed for the operating point with a maximum output power of 180 MW. The deviations

Table 3. Mesh refinement and discretization uncertainties

Parameters	Head H	Torque T	Efficiency η
r_{21}	1.32	1.32	1.32
r_{32}	1.34	1.34	1.34
p	2.56	3.62	13.96
$e_a^{21} [\%]$	1.26	1.28	0.02
$e_{ext}^{21} [\%]$	1.19	0.72	0.01
$GCI^{21} [\%]$	1.50	0.91	0.01

**Figure 7.** Grid convergence

of the mean values for the head H , the runner torque T and the efficiency η calculated with CFD from the measured values are less than 1% and are therefore in the range of the measurement uncertainties. Figure 8 shows the unsteady pressure distribution for the converged calculation.

The evaluation of the pressure signal of the monitor point in the rotating domain between the runner and guide vane blades reveals the blade passing frequency f_{BP} as the dominant excitation (see figure 9). This corresponds to the frequency analysis of the strain gauge measurements, although the sensors therefore have been attached to the trailing edge of the runner. Thus, the impact of the rotor-stator interaction on the dynamic pressure field is acquired sufficiently with the used CFD methods. Two further amplitude peaks are revealed at frequency ratios of $f/f_0 = 10$ and $f/f_0 = 30$ which could be indicated by the pressure wakes of the stay vanes with a number of 10 blades. The time depending fluctuation of the pressure distribution is further transformed into the frequency

An Approach to Evaluate the Lifetime of a High Head Francis Runner — 6/10

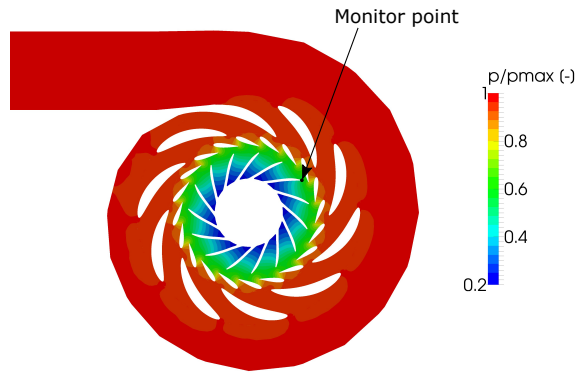


Figure 8. Unsteady pressure distribution at maximum output power

domain using the Fast Fourier method (see 3.2.3).

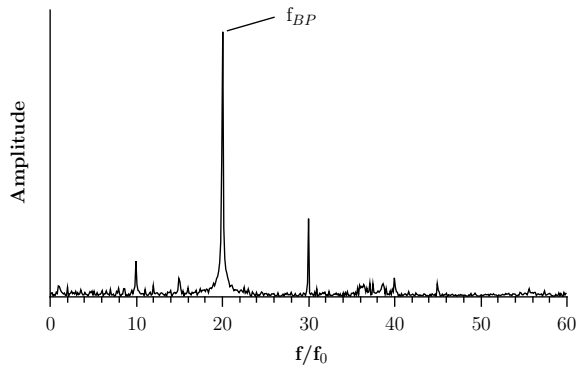


Figure 9. Frequency spectrum of the pressure signal at monitor point

3.2 Structural analysis

3.2.1 Steady calculations

To evaluate the overall load and the points with the highest stresses on the Francis runner, steady Finite Element analysis are performed using the open-source program Code Aster. Therefore, a cyclic sector consisting of one runner blade and the appropriate hub and shroud regions is considered in order to reduce simulation time and costs. The unstructured tetrahedral mesh with quadratic elements consists of about 200,000 nodes (see figure 10). The results from the unsteady CFD simulations are averaged over time and the pressure distribution is then applied to the FE model by an interpolation between the meshes of the fluid and the structural domain. Cyclic symmetry boundary conditions are used for the connection between the sectors of the runner, which is fixed at the bolt circle. The centrifugal forces induced by the rotation and the influence of gravitation are also considered. The pressure distributions in the side chambers of the runner are calculated and applied by an analytical approach using the pressure values at the inlet

and outlet of the runner or by an axial thrust calculation. The material for the Francis runner is a steel of type X5CrNi13-4 with an E-modulus of $E = 216 \text{ kN/mm}^2$, a Poisson ratio of $\nu = 0.30$ and a density of $\rho_R = 7.700 \text{ kg/m}^3$.

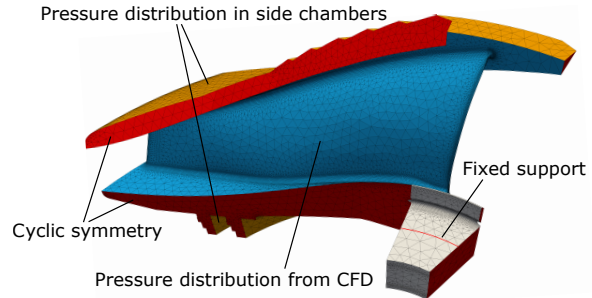


Figure 10. Mesh and boundary conditions for steady structural analysis

Figure 11 shows the Mises stress results of the static FE analysis for the operating point at 180 MW output power. The hot spot with the maximum load is at the trailing edge close to the hub of the runner. The method for the static structural investigation is validated in future publications by comparing the mean stresses at the positions of the strain gauges applied on the prototype Francis runner.

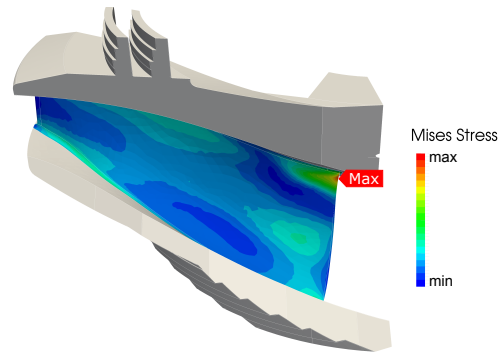


Figure 11. Mises stress at maximum power output

3.2.2 Modal analysis

At the whole procedure of runner lifetime prediction the question about the natural frequencies and mode shapes of the structure is evident. The following chapter will describe in brief the basics and challenges by performing these calculations.

It is common sense that the dynamic structure could be described by the following equation:

$$[M_S] \{\ddot{u}\} + [C_S] \{\dot{u}\} + [K_S] \{u\} = \{F_S\} \quad (6)$$

where $[M_S]$ is the structural mass matrix, $[C_S]$ the structural damping matrix, $[K_S]$ the structural stiffness matrix, $\{F_S\}$ the applied load vector and $\{u\}$ the nodal displacement vector.

An Approach to Evaluate the Lifetime of a High Head Francis Runner — 7/10

As Francis runners operate in surrounding water the fluid-structure interaction has to be taken into account. The mathematical description of this problem including a comparison of some results between calculation and measurements is well described by [7]. It gets clear, that the natural frequencies differ between investigations in air and water, which were also described by [15] and [16]. Still unsolved is the question about the influence of the attached fluid part to the numerical model. Francis runners will never run in this big amount of surrounded water like shown at several publications. This question is part of our research project and will be published later on.

As a first step, the natural frequencies and mode shapes are investigated following the description mentioned above by using the model shown in figure 12. For the runner itself a mesh with about 1.2 million nodes consisting of tetrahedral quadratic solid elements is used. The added mass of the water around the runner for the coupled investigation is simulated by using acoustic fluid elements sharing the same node group at the interface with the structural elements. As Code Aster 11.7 provides no cyclic symmetry option regarding acoustic elements for sectoral investigations the total runner has to be modeled. The water properties under environmental temperature and atmospheric pressure are: Density $\rho_w = 1000 \text{ kg/m}^3$ and speed of sound in water $c = 1483 \text{ m/s}$. The complete runner model is fixed at the bolt circle, whereas the outside of the surrounding water is fixed by a wall definition.

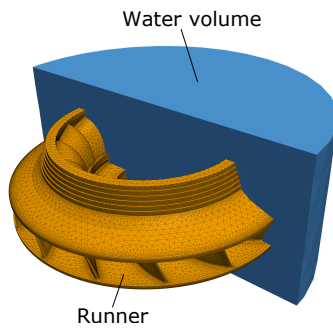


Figure 12. Boundary conditions for modal analysis

The results of the numerical simulation for the coupled system are shown in figure 13 with a mode shape of two nodal diameters (ND) at $f/f_0 = 19.8$ and a mode shape with three ND at $f/f_0 = 37.6$ for the investigated runner. Simulations have been performed up to $f/f_0 = 40$, which is twice the frequency of the rotor-stator interaction (compare figure 9) and therefore sufficient to evaluate, if there are natural modes in the range of the RSI frequency. Although the mode shape with two nodal diameters is very close to the blade passing frequency at $f_{BP} = 20.0$, the runner can only be excited by the rotor-stator interaction, if the nodal diameter of the pressure field k matches the natural mode shape (see equation 7).

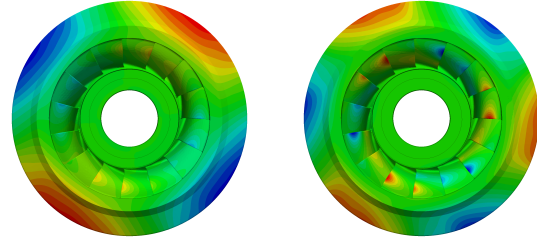


Figure 13. Mode with ND 2 $f/f_0 = 19.8$ (left) and ND 3 at $f/f_0 = 37.6$ (right)

3.2.3 Harmonic response analysis

The dynamic pressure field excited by the rotor-stator interaction can be described by

$$m \cdot Z_r - n \cdot Z_g = k \quad (7)$$

with the number of runner blades Z_r and the associated harmonic index m , the number of guide vanes Z_g with its harmonic index n and the corresponding nodal diameter of the pressure field k (see [11]). The temporal pressure field observed in the rotor frame for any point M in a meridian section and any azimuth θ can be described in the Fourier domain by

$$p_{m,n}(M, \theta, t) = p_{m,n}(M, \theta) e^{-2i\pi \cdot n \cdot Z_g \cdot f_0 \cdot t} \quad (8)$$

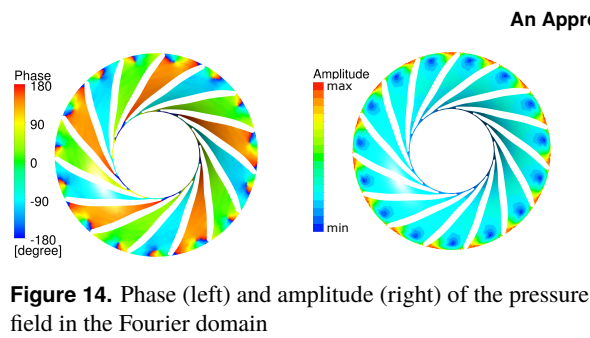
The Fourier transformation at the blade passing frequency f_{BP} of all discrete points in the runner domain is sufficient to describe the dynamic behavior due to the rotor stator interaction.

The critical nodal diameter of the pressure field for the investigated Francis turbine is $k = 5$ as described in table 4.

Table 4. Nodal diameter k of the dynamic pressure field

		Harmonic index n of the guide vanes		
		0	1	2
Harmonic index m of the runner	0	0	-20	-40
	1	15	-5	-25
	2	30	10	-10

The Fourier transformation of the pressure field obtained by the CFD simulations is displayed in figure 14. The nodal diameter $k = 5$ is clearly visible. The results for the different operating conditions are then applied to the entire runner structure for the harmonic response analysis using Code Aster, to evaluate the dynamic loads and further the lifetime of the turbine. The boundary conditions for the harmonic response analysis are the same as for the modal analysis described in the previous section.



4. RUNNER FATIGUE ANALYSIS AND LIFETIME EXPECTATIONS

The last section of this paper is devoted to the big part of runner fatigue analysis. The aim today is the determination of an exact lifetime of a hydraulic runner at the design stage. At the present the hydropower community deals with either numerical or experimental investigations. Some single flow phenomena, like for example RSI behavior (see [10], [9], [17]), machine startup (see [6]) or off design operation (see [12]), are already researched and the impact onto the structure is extrapolated to the runner life time. Common to all of these investigations is the numerical background and starting point, whereas structural belongings, like for example pre-stressed material or residual stresses at the runner itself, are again investigated separately, see [18]. To include all phenomena into one bigger method is the challenge of today and the future. An interdisciplinary approach is therefore of high importance and suppliers, operators and universities are invited to work together on this exciting topic. And one of the biggest question at this stage is still the portability to other Francis runners as each prototype layout of a turbine is more or less unique.

4.1 Operating conditions - Load spectrum

An important role to estimate the lifetime of a runner is the load spectrum as it should give some kind of real usage over a given time history of the component. Questions about the operational conditions, operation duration at off design point, start-up and shut down of the machine, load rejection and so on have to be taken into account. Each of these questions have to be investigated afterward in terms of load samples either by numerical investigation or better by measurement setup. Separating this huge amount of data into single segments will deliver a data pool for the operating profile. Subsequently, the combination of this data pool with the sequence of operational conditions should deliver a load spectrum or load-time history of the hydraulic runner. Figure 15 shows a general approach for the generation of a load spectrum and was adapted from [19]. The importance and correct prediction of this load-time history was also recognized by [20]. Therefore, it is mandatory that operators are involved in these tasks as they can provide the appropriate basic data.

An Approach to Evaluate the Lifetime of a High Head Francis Runner — 8/10

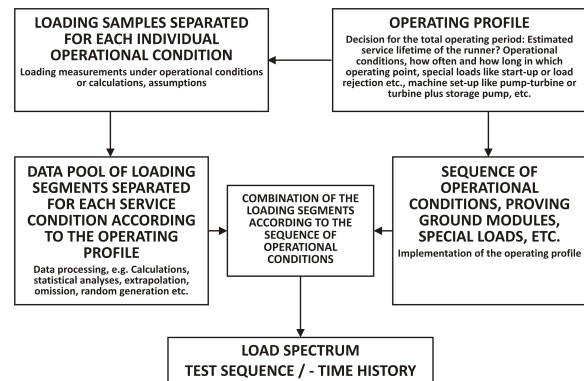


Figure 15. General approach for the generation of standardized load-time histories (adapted from [19])

4.2 Runner fatigue analysis

The most important part of this method is dedicated to the runner fatigue analysis itself as the output of this investigation should be the expected or, in terms of already operating runners, the residual lifetime.

Normally the points with the highest stresses in Francis turbines are at the trailing edge near the band and crown, which is the result of the FSI calculations before. The subsequent runner fatigue calculations rely on the based fatigue model (see for example [21] or [5]) due to the appearance of multi-axial stress state or not. This would impose that more sophisticated fatigue models should be used like for example the critical plane principle or the micro-crack approach. And as hydraulic runners are designed for a long service life the excitations from different flow phenomena result in a high number of fatigue cycles. Therefore, a high-cycle fatigue (HCF) approach is recommended. Material properties, manufacturing processes (welding) and stress state have to be combined together to resolve this part of the described method.

The applied method revealed for the investigated runner at the worst case a residual life time of about 60 years.

5. CONCLUSION AND OUTLOOK

At the presented paper we have described a method to evaluate the lifetime of a high head Francis runner. Single steps have been discussed and two approaches, numerical and experimental, have been shown. Goal of this research project is a lifetime calculation at the design process of a Francis runner prototype. Therefore, strain gauge measurements at an existing runner have been performed to gain validation parameters for the numerical methods.

Nevertheless, some special tasks still have to be discussed as an outlook for the future of this method and the research project. These are:

1. Comparison of open-source and commercial software for this kind of investigation regarding resources and calculation time.

An Approach to Evaluate the Lifetime of a High Head Francis Runner — 9/10

2. Check the applicability of recently given turbulence models for special stochastic flow phenomena. Are the turbulence models able to solve these problems realistically?
3. Suitability of the harmonic response analysis approach for non-harmonic flow phenomena. Some of them can be considered like the rotor-stator interaction as shown but stochastic ones need a transient response analysis as shown for example by [22]. How can we perform any kind of signal decomposition?
4. Sensitivity analysis of the influence of modeling the added mass of water at the calculation of the natural frequencies. How much surrounding water is necessary and what is a realistic approach. This task could be combined with the question of appropriate system modeling and fixation of the runner.
5. Generation of the load-time history for the investigated runner to obtain a realistic load spectrum. What is the correct prediction and validation of the necessary assumptions?

ACKNOWLEDGMENTS

The K-Project GSG-GreenStorageGrid is funded in the framework of COMET - Competence Centers for Excellent Technologies by the Federal Ministry of Transport, Innovation and Technology, the Federal Ministry of Science, Research and Economy, the Vienna Business Agency, the Federal Province of Lower Austria and by the Federal Province of Upper Austria. The program line COMET is administered by the Austrian Research Promotion Agency (FFG). The authors would like to thank all project partners for their contribution to the research project.

The computational results presented have been achieved (in part) using the Vienna Scientific Cluster (VSC).

REFERENCES

- [1] Eduard Doujak. Effects of increased solar and wind energy on hydro plant operation. *HRW*, 22:28–31, 2014.
- [2] André Coutu, Hans Aunemo, Bruce Badding, and Omprakash Velagandula. Dynamic behaviour of high head francis turbines. In *Hydropower & Dams*, editor, *Conference Proceedings of HYDRO 2005*. Aqua Media International, 2005.
- [3] André Coutu, Christine Monette, and Omprakash Velagandula. Francis runner dynamic stress calculations. In *Hydropower & Dams*, editor, *Conference Proceedings of HYDRO 2007*. Aqua Media International, 2007.
- [4] André Coutu and Joel Chamberland-Lauzon. The impact of flexible operation on francis runners. *International Journal on Hydropower & Dams*, Issue Two:90–93, 2015.
- [5] Hans-Jörg Huth. *Fatigue Design of Hydraulic Turbine Runners*. PhD thesis, Norwegian University of Science and Technology (NTNU), Trondheim, February 2005.
- [6] M. Gagnon, S. A. Tahan, P. Bocher, and D. Thibault. Impact of startup scheme on francis runner life expectancy. *IOP Conference Series: Earth and Environmental Science*, 12:012107, 2010.
- [7] Miriam Flores, Gustavo Urquiza, and José María Rodríguez. A fatigue analysis of a hydraulic francis turbine runner. *World Journal of Mechanics*, 02(01):28–34, 2012.
- [8] Andrea Carpinteri, Cristian Bagni, Daniela Scorza, and Sabrina Vantadori. High-cycle fatigue in a hydraulic turbine runner. In Andrea Carpinteri, Francesco Iacoviello, Les P. Pook, and Luca Susmel, editors, *Proceedings of Crack Paths (CP 2012)*, Gaeta, Italy 2012, pages 287–294. IGF-Gruppo Italiano Frattura, 2012.
- [9] R. Guilleme and J. Deniau. Rotor-stator interaction in high head pump turbines: dynamic response of the structure. *Hydro 2011 (Prague, Czech Republic)*, 2011.
- [10] U. Seidel, B. Hübner, J. Löfflad, and P. Faigle. Evaluation of rsi-induced stresses in francis runners. *26th IAHR Symposium on Hydraulic Machinery and Systems (Beijing, China)*, 2012.
- [11] R. Guillaume, J. L. Deniau, D. Scolaro, and C. Colombet. Influence of the rotor-stator interaction on the dynamic stresses of francis runners. *IOP Conference Series: Earth and Environmental Science*, 15(5):052011, 2012.
- [12] B. Nennemann, J. F. Morissette, J. Chamberland-Lauzon, C. Monette, O. Braun, M. Melot, A. Coutu, J. Nicolle, and A. M. Giroux. Challenges in dynamic pressure and stress predictions at no-load operation in hydraulic turbines. *IOP Conference Series: Earth and Environmental Science*, 22(3):032055, 2014.
- [13] Marcelo Vinicius Magnoli. *Numerical simulation of pressure oscillations in large Francis turbines at partial and full load operating conditions and their effects on the runner structural behaviour and fatigue life*. PhD thesis, Technische Universität München, München, 10.06.2015.
- [14] B. Celik, U. Ghia, P. Roache, Ch Freitas, H. Coleman, and P. Raad. Procedure for estimation and reporting of uncertainty due to discretization in cfd applications. *Journal of Fluids Engineering*, 130(7):078001, 2008.
- [15] Q. W. Liang, Cristian G. Rodriguez, Eduard Egusquiza, Xavier Escaler, Mohamed Farhat, and François Avellan. Numerical simulation of fluid added mass effect on a francis turbine runner. *Computers & Fluids*, 36(6):1106–1118, 2007.
- [16] C. G. Rodriguez, E. Egusquiza, X. Escaler, Q. W. Liang, and F. Avellan. Experimental investigation of added mass effects on a francis turbine runner in still water. *Journal of Fluids and Structures*, 22(5):699–712, 2006.
- [17] B. Hübner, U. Seidel, and S. Roth. Application of fluid-structure coupling to predict the dynamic behavior of turbine components. *IOP Conference Series: Earth and Environmental Science*, 12:012009, 2010.

An Approach to Evaluate the Lifetime of a High Head Francis Runner — 10/10

- [18] M. Sabourin, D. Thibault, D. A. Bouffard, and M. Lévesque. New parameters influencing hydraulic runner lifetime. *IOP Conference Series: Earth and Environmental Science*, 12:012050, 2010.
- [19] P. Heuler and H. Klätschke. Generation and use of standardised load spectra and load–time histories. *International Journal of Fatigue*, 27(8):974–990, 2005.
- [20] Martin Gagnon, Antoine Tahan, Philippe Bocher, and Denis Thibault. Influence of load spectrum assumptions on the expected reliability of hydroelectric turbines: A case study. *Structural Safety*, 50:1–8, 2014.
- [21] Lixia Zhang, Fuzhou Feng, Xinhai Fan, and Pengcheng Jiang. Reliability analysis of francis turbine blade against fatigue failure under stochastic loading. In Hong-Zhong Huang, Ming J. Zuo, and Yu Liu, editors, *The Proceedings of 2012 International Conference on Quality, Reliability, Risk, Maintenance, and Safety Engineering: ICQR2MSE 2012*, pages 987–990, Piscataway and NJ, ©2012. IEEE.
- [22] Martin Gagnon, Antoine Tahan, Philippe Bocher, and Denis Thibault. On the stochastic simulation of hydroelectric turbine blades transient response. *Mechanical Systems and Signal Processing*, 32:178–187, 2012.

Chapter 7

Static Structural Investigations

7.1 Paper 2

In the second paper (see Tab. 7.1) the results of the fluid-structure simulations of the investigated high head Francis turbine are discussed. Therefore, unsteady CFD simulations are performed with OpenFOAM in several operating points from full-load to low-load operation. The global parameters like the head, the runner torque and the efficiency are compared to the prototype site measurements to validate the numerical flow simulations. Two different models for the CFD computations are used to investigate the influence of the inlet boundary condition on the flow behavior and the structural loads: A full model considering the spiral casing, the stay vanes and guide vanes, the runner and the draft tube. And a reduced model without the spiral casing and a cyclic inlet boundary condition. The averaged pressure distributions of the unsteady CFD simulations are further used to compute the mean stresses of the high head runner in different operating points. Hence, static FEM simulations are performed with Code_Aster using the cyclic sector model described previously.

Table 7.1: Notes on Paper 2.

Title	Investigation of the Fluid-Structure Interaction of a High Head Francis Turbine Using OpenFOAM and Code_Aster
Authors	M. Eichhorn, E. Doujak, L. Waldner
Conference	28th IAHR Symposium on Hydraulic Machinery and Systems (IAHR 2016)
Location	Grenoble, France
Date	July 4-8, 2016
Published in	IOP Conference Series: Earth and Environmental Science, Volume 49/7: 072005, 2016

Investigation of the fluid-structure interaction of a high head Francis turbine using OpenFOAM and Code_Aster

M. Eichhorn, E. Doujak, L. Waldner

TU Wien, Institute for Energy Systems and Thermodynamics, Getreidemarkt 9/302, 1060 Vienna, Austria

E-mail: markus.eichhorn@tuwien.ac.at

Abstract. The increasing energy consumption and highly stressed power grids influence the operating conditions of turbines and pump turbines in the present situation. To provide or use energy as quick as possible, hydraulic turbines are operated more frequent and over longer periods of time in lower part load at off-design conditions. This leads to a more turbulent behavior and to higher requirements of the strength of stressed components (e.g. runner, guide or stay vanes). The modern advantages of computational capabilities regarding numerical investigations allow a precise prediction of appearing flow conditions and thereby induced strains in hydraulic machines. This paper focuses on the calculation of the unsteady pressure field of a high head Francis turbine with a specific speed of $n_q \approx 24 \text{ min}^{-1}$ and its impact on the structure at different operating conditions. In the first step, unsteady numerical flow simulations are performed with the open-source CFD software OpenFOAM. To obtain the appearing dynamic flow phenomena, the entire machine, consisting of the spiral casing, the stay vanes, the wicket gate, the runner and the draft tube, is taken into account. Additionally, a reduced model without the spiral casing and with a simplified inlet boundary is used. To evaluate the accuracy of the CFD simulations, operating parameters such as head and torque are compared with the results of site measurements carried out on the corresponding prototype machine. In the second part, the obtained pressure fields are used for a fluid-structure analysis with the open-source Finite Element software Code_Aster, to predict the static loads on the runner.

1. Introduction

The transition of the energy system all over Europe of nation states has broken up an old history of electricity supply and grid control. New suppliers based on renewable energy sources have appeared and made the electricity production more flexible. Forecasts about the gap between supply and demand became even more uncertain and future trends about energy storage technologies and their role in the energy system are under investigation and research. Different studies with various approaches cannot deliver satisfying answers to the needs of our energy system within the next 20 years and beyond. The crucial topic of energy storage is common to all studies: without short-term and long-term storage possibilities as well as decentralized storage capabilities no transition of the energy system is possible. Short-term storage possibilities are characterized by their short charging and discharging characteristic and are therefore ideal for a quick demand response and grid stabilization. In 2008 the study of the Energy Storage Task Force [1] predicted a new era of increased importance and usage for the battery technology.

Today we see that these predictions are behind the expectations of 2008. Reality showed that especially the new storage technologies could not be successful due to the deterioration of the market sales price after 2009. In 2013 the roadmap of the EASE/EERA Core Working Group [2] assumed that the short term electricity balancing market will be there, where energy storage is based on commercial business cases. This means more research and development activities for recent technologies but also new challenges for the established ones. The need for research and adaption of existing hydropower plants as well as the development of decentralized pumped storage technologies are summarized in the Hydro Equipment Association roadmap [3]. The increasing amount of volatile energy sources (e.g. wind and solar) forces the operators of large pumped storage plants to deliver more regulating power to the electric grid and to decrease the response time of the hydraulic machines. Francis turbines, which can be used within a wide range of discharge and head, are therefore operated over longer periods of time at off-design conditions. This involves the appearance of unstable flow phenomena, depending on the specific speed and the operating point of the machine (see Magnoli et al. [4]). The dynamic flow effects have an important influence on the expected lifetime of the Francis turbine. In full load and higher part load operation, the rotor-stator interaction is mainly important, especially for high head machines. In lower part load, draft tube vortex ropes and interblade vortices appear, which leads to pressure pulsations in the turbine. Start-stop cycles and speed-no-load operations have a more stochastic influence on the runner and a significant impact on the life expectancy, as Coutu et al. [5] or Gagnon et al. [6] showed. Several studies have been published to examine the influence of the static and dynamic pressure effects on the structural behavior of the Francis runner by using fluid-structure interaction (FSI) (see [7–11]). In order to investigate the lifetime of a high head Francis turbine, an approach has been applied by Doujak et al. [12] within a large research project, using numerical flow simulations and Finite Element computations compared with prototype site measurements (see figure 1).

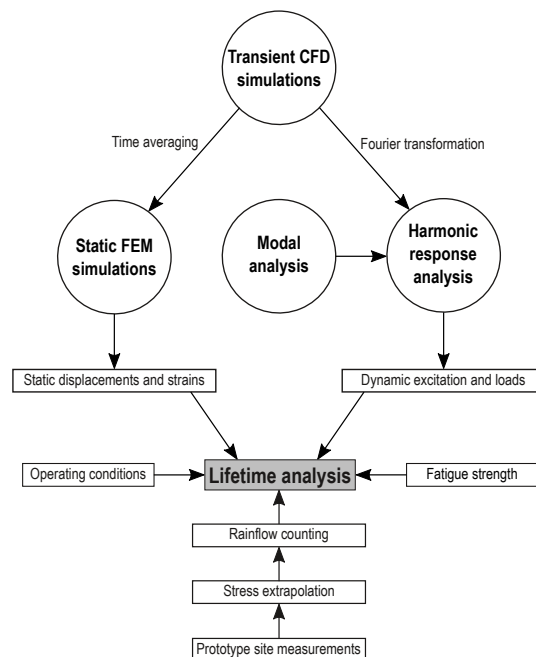


Figure 1: Approach for the lifetime investigation of a Francis runner

Within the numerical path static and dynamic computations are performed to evaluate the appearing stresses at the investigated Francis runner. This paper focuses on the CFD and

static FEM simulations with particular emphasis on the usage of open-source software and its capabilities.

2. Prototype site measurements

In order to evaluate the accuracy of the numerical approach used for the fluid-structure interaction, measurements on a prototype Francis turbine with a specific speed of $n_q \approx 24 \text{ min}^{-1}$ were performed. They were done in different operating points at nearly constant head in steps of 10 MW or 20 MW from the machine start-up to the maximum power of 180 MW and back again. The Francis machine consists of the spiral casing, 10 stay vanes, the wicket gate with 20 guide vanes, the runner with 15 blades and the draft tube. The operating parameters such as head, output power, guide vane opening, the pressure in front of the spiral casing and at the draft tube outlet were recorded during the measurements. The stresses on the runner were obtained by eight strain gauges attached to the suction and pressure side of one runner blade (see figure 2 left). This blade's trailing edge region was measured with a 3D measurement arm and the geometry of the original CAD model has been adapted to increase the accuracy of the FEM simulations. The data of the strain gauge measurements were recorded with a sampling rate of 1 kHz using a data logger, which was mounted in a casing on the rotating shaft inside the draft tube (see figure 2 right).

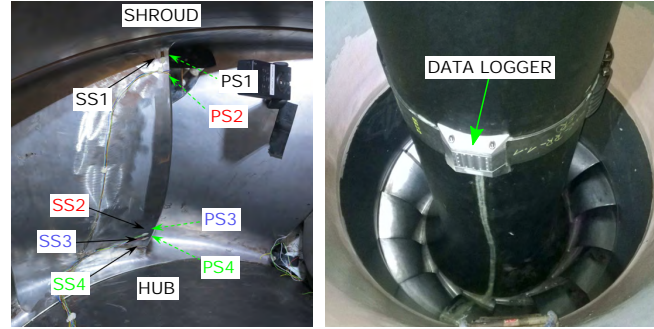


Figure 2: Positions of the strain gauges applied to the runner blade (left) and data logger casing (right)

3. CFD simulations

3.1. Numerical setup and discretization

The numerical flow simulations are performed with the open-source CFD software OpenFOAM 2.3 using unsteady Reynolds averaged Navier-Stokes equations (URANS). The capabilities of OpenFOAM regarding unsteady simulations for a high head Francis turbine at off-design conditions have been shown by Aakti et al. [13] and Lenarcic et al. [14]. Two different types of physical models are used for the CFD calculations: A full model adjusted according to the prototype machine, including the spiral casing (SC), the stay vanes (SV) and guide vanes (GV), the runner (RN) and the draft tube (DT). In comparison, a reduced model with a cyclic domain for the stay vanes excluding the spiral casing is used. The inlet region is therefore extended in radial direction to avoid impacts from these boundary conditions. A similar approach has been performed by Lenarcic et al. [15]. The particular domains of both models are spatially discretized in multiblock hexahedral grids using Ansys ICEM 15.0. The non-conformal domains are connected at the interfaces (IF) using the arbitrary mesh interface (AMI) implemented in OpenFOAM (see figure 3). The whole mesh consists of about 5.9 million cells for the full model and 5.6 million cells for the reduced model. The quality of the meshes are evaluated regarding the minimum determinant, angle and aspect ratio. The number of cells and the quality of the meshes are summarized in table 1.

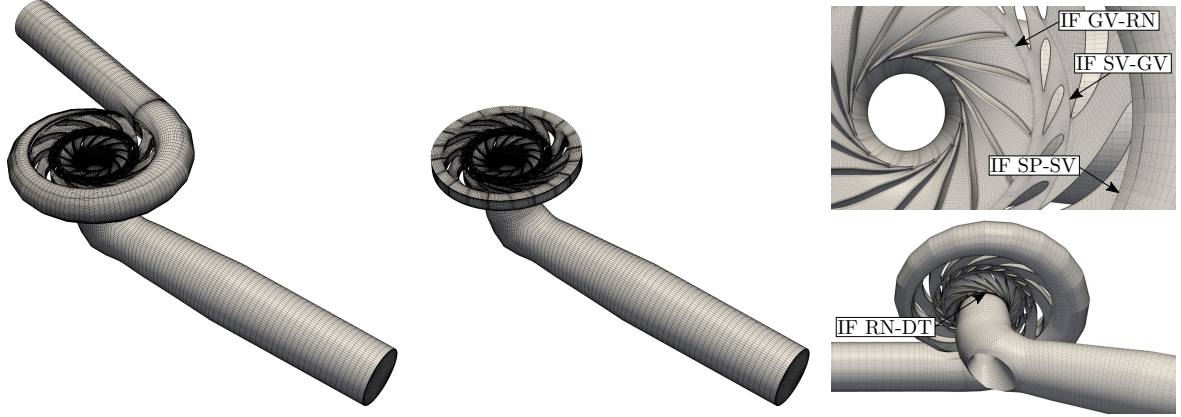


Figure 3: CFD models and discretization for the full model (left) and the reduced model (middle); Interfaces between the CFD domains (right)

Table 1: Mesh size and quality for the CFD discretization

Parameters	SC	SV		GV	RN	DT
		full	reduced			
Number of cells (Mio.)	0.60	0.72	1.05	1.69	2.57	0.30
Minimum determinant (-)	0.28	0.36	0.42	0.69	0.21	0.33
Minimum angle (°)	11.0	16.1	26.0	22.5	18.6	18.9
Minimum aspect ratio (-)	0.001	0.001	0.001	0.002	0.002	0.015
y_{mean}^+ (-)	95	50	50	65	70	60

In order to estimate the uncertainties due to the discretization of the CFD model, a grid independence study has been performed with the full model according to the approach of Celik et al. [16]. The procedure for the mesh refinement and the evaluation of the results have been already published by Doujak et al. [12]. The results reveal a monotonic convergence for the three global parameters head, runner torque and efficiency with a decreasing grid size h_i (see figure 4). Considering the computational costs and the accuracy of the CFD simulations, the medium grid (as described in table 1) with a normalized size of $h_{2,n} = 1.32$ is used for the further investigations.

The unsteady CFD simulations are performed in seven operating points with varying output power P , guide vane angles Φ and discharge Q from full load at 180 MW to low load at 20 MW. The meshes for the wicket gate domain are adjusted to the according positions of the site measurements. The operating parameters for the CFD simulations are listed in table 2. Due to unsteady flow conditions at off-design points, a transient rotor-stator analysis with a rotating runner domain is used. To improve the convergence, the unsteady simulations are initialized using the results of steady-state calculations. These are performed with the multiple frame of reference (MRF) solver, which couples the rotating and stationary interfaces with the frozen-rotor approach. The pressure-velocity coupling is done with the SIMPLE algorithm using moderate under-relaxation factors. The unsteady simulations are performed with the PIMPLE algorithm, which couples the SIMPLE and PISO procedure. Therefore, a stable solution can be reached even at increased physical time steps and higher Courant numbers due to the advantage of inner iteration loops together with under-relaxation. The time step is chosen according to a runner rotation of 0.36° per time step, which yields a maximum Courant number of $Co_{max} = 15$.

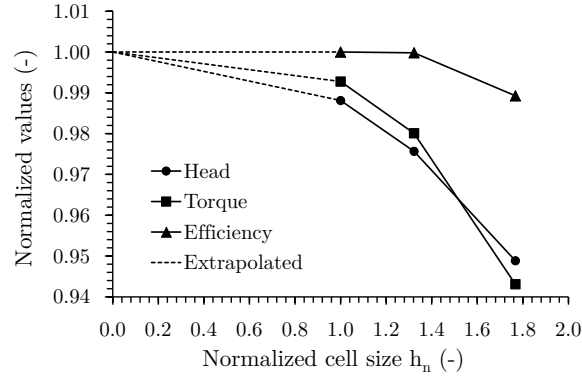


Figure 4: Grid convergence

For the low load operating points from 60 MW to 20 MW power, the time step is decreased to 0.18° runner rotations and the number of inner iteration loops is increased to ensure accurate results. The convective term is discretized by a second-order scheme and the single-phase fluid is considered to be incompressible. A constant discharge is set at the spiral casing inlet for the full model. For the reduced model a corresponding velocity distribution with an incidence angle of $\alpha = 14.5^\circ$ is defined at the stay vane inlet. The simulations are done using the two-equation turbulence model $k-\omega$ SST. The turbulent quantities k and ω correspond to a turbulent mixing length $l_t = 0.125\text{ m}$ and a turbulent intensity $I = 0.1$ at the inlet. At the outlet an averaged pressure condition is defined. After the simulation is converged, at least ten runner rotations are performed. To evaluate the accuracy of the used setup the parameters of the hydraulic machine such as the head, the runner torque and the efficiency are averaged over multiple runner rotations and compared with the site measurements. The setup and the boundary conditions for the numerical flow simulations are summarized in table 3.

Power P (MW)	Rel. GV angle ϕ/ϕ_{max} (-)	Rel. discharge Q/Q_{max} (-)
180	1.000	1.000
140	0.772	0.783
100	0.576	0.582
80	0.479	0.481
60	0.382	0.378
40	0.282	0.273
20	0.173	0.164

Table 2: Operating parameters for the CFD simulations

Parameters	Description
Software	OpenFOAM 2.3
Analysis type	Transient rotor-stator
Time step	$0.36^\circ / 0.18^\circ$
Simulation time	10 runner rotations
Inlet BC	Discharge / Velocity
Outlet BC	Static pressure
Interface coupling	AMI
Turbulence model	$k-\omega$ SST
Advection scheme	Second order
Max. Courant number	15

Table 3: Setup for the CFD simulations

3.2. CFD Results

The results of the relative efficiency, compared to the best measured efficiency, at the different operating points for the two physical models are displayed in figure 5 on the left side. The characteristics show a good agreement between the site measurements and the CFD simulations. At full load operation the relative values for the efficiency are slightly lower than the measured ones, even the full model reveals more accurate results. At part load operation, the values are also in a good agreement to the site measurements due to the adjusted CFD setup. The relative

deviations for the head and the runner torque show a good agreement as well (see figure 5 right). The values differ by less than 5% for all operating points and both physical models, only the deviations for the runner torque at 20 MW are bigger with approximately 9%. The influence of the spiral casing to the global parameters is very low and therefore a reduced model would be sufficient.

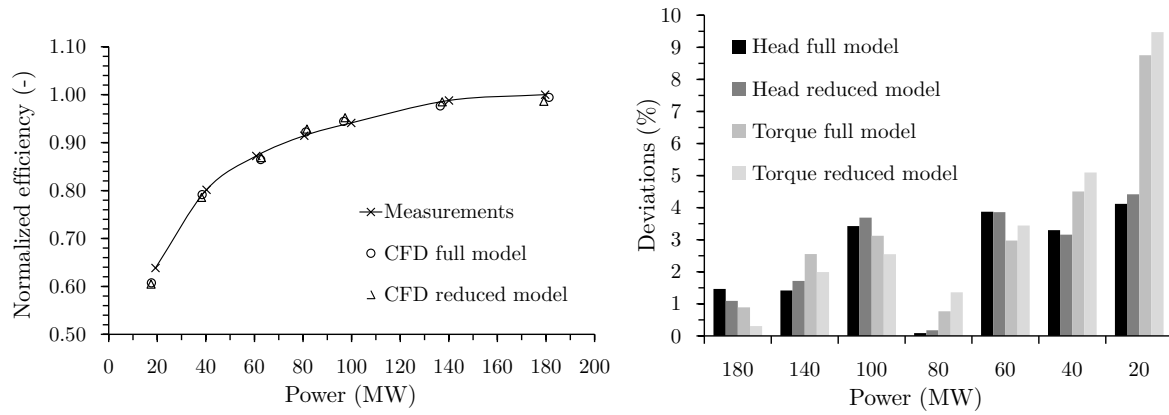


Figure 5: Normalized efficiencies (left) and deviations for the head and runner torque (right)

In figure 6 the streamlines in the runner and draft tube domain for the operating points at 180 MW and at 60 MW are illustrated. The displayed velocity is calculated in the relative frame of reference. At full load there are hardly any vortices visible in the runner and draft tube. In part load operation flow separation appears at the inlet of the runner due to the smaller discharge and the inadequate incident flow. The circumferential velocity at the draft tube inlet is also higher than at full load, which decreases the efficiency of the turbine.

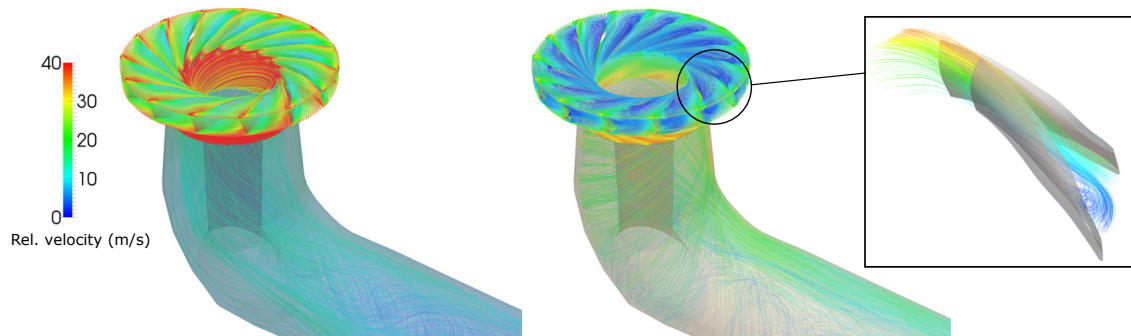


Figure 6: Streamlines at 180 MW (left) and 60 MW (right)

For the structural analysis the pressure distribution on the runner surfaces is necessary to define the boundary conditions in the different operating points. Therefore, the static pressure on one runner blade and the according hub and shroud region is recorded during the unsteady CFD simulations and averaged afterwards over ten runner rotations, to obtain a steady distribution. The normalized pressure regimes on the blade for two operating points at full load (180 MW) and part load (60 MW) are displayed in figure 7.

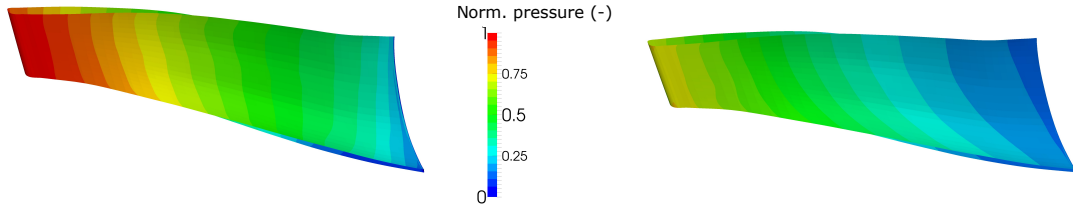


Figure 7: Pressure distribution at the blade pressure side at 180 MW (left) and 60 MW (right)

4. Structural analysis

4.1. Numerical setup and discretization

Another purpose beside the flow simulations is the investigation of the structural behavior of the high head Francis runner at different operating conditions. The results from the CFD analysis are used to examine the overall loads and stresses with static FEM simulations. Similar to the numerical flow investigation, the focus lies on the usage of open-source software for the structural analysis. Thus, the FEM calculations are performed with Code_Aster 11.7. The strain gauge measurements, mentioned in section 2, are used to evaluate the accuracy of the setup considering the appearing strains and stresses on the prototype runner. The structural model consists of a cyclic sector with one runner blade and the appropriate hub and shroud regions in order to reduce simulation time and costs. The discretization is done with the pre-and post-processing platform SALOME. Due to the complex geometry including the hub and shroud of the runner, an unstructured tetrahedral mesh with about 230,000 nodes is used (see figure 8).

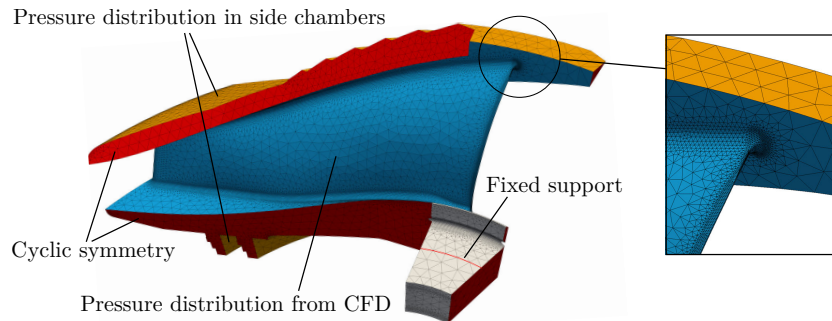


Figure 8: Mesh and boundary conditions for the static FEM simulations

In order to increase the accuracy of the numerical simulations, second order elements with a quadratic interpolation function are used. The mesh is refined in critical regions like the fillet between the blade and the hub respectively shroud or at the trailing edge of the blade, where the strain gauges have been applied. The sector model is connected at the interfaces using cyclic symmetry conditions. The runner is fixed at the bolt circle, centrifugal and gravitational forces are considered too. The flow in the side chambers of the runner has not been considered in the CFD simulations, but the pressure distribution is calculated analytically and applied to the appropriate FE surfaces, in order to increase the accuracy of the model. On the blade, hub and shroud surfaces, the pressure distribution from the CFD simulations is interpolated between the fluid and structural meshes and applied to the FEM model. The material of the runner is a stainless steel with an E-modulus of $E = 216 \text{ kN/mm}^2$, a Poisson ratio of $\nu = 0.30$ and a density of $\rho_R = 7.700 \text{ kg/m}^3$. The setup for the FEM simulations is summarized in table 4.

Table 4: Setup for the FEM simulations

Parameters	Description
Software	Code_Aster 11.7
Analysis type	Static FEM
Model	Sector with 1 runner blade
Mesh size	230,000 nodes
Mesh type	Quadratic tetrahedral
Material	Stainless steel

4.2. FEM Results

Figure 9 shows the mean stresses σ_m from the site measurements and the FEM simulations for the strain gauge positions PS4 (left) and SS4 (right). The values are normalized to the yield strength σ_y of the runner material. According to the CFD analysis, there is hardly any difference visible for the two physical models (full and cyclic). The stress curve at the strain gauge location PS4 reveals a larger gradient along the power curve compared to the measurements. At full load conditions, the stresses are higher, whereas at part and low load operation the values are below the measured ones. For the strain gauge location SS4 the results for the simulations are uniformly higher along the load conditions but the tendencies are in a good agreement.

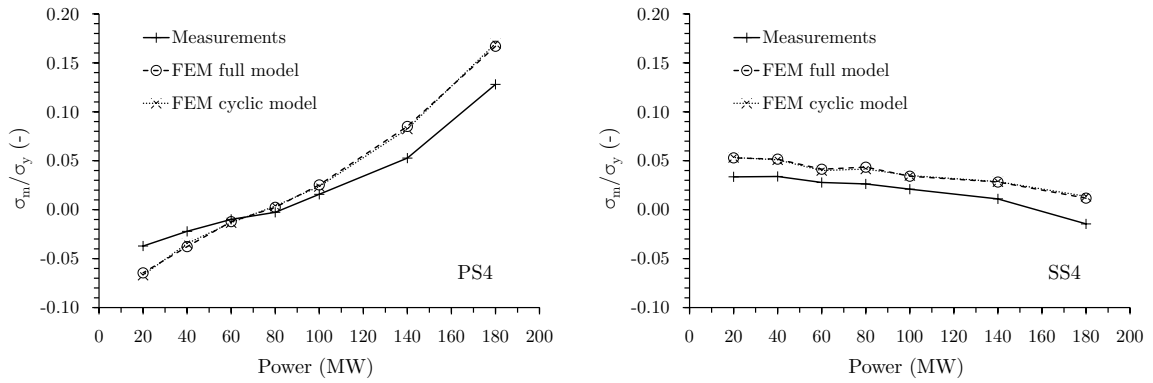


Figure 9: Comparison of the measured and computed mean stresses at the strain gauge positions PS4 (left) and SS4 (right)

In figure 10 a linear regression analysis is used to determine the accuracy between the measurements and the simulations. The comparison for all operating points and strain gauges (left) shows a good agreement, even if the slope of about 1.27 is higher than 1. At 180 MW power (middle) there is a shift in the vertical direction but the gradient is close to 1. At 60 MW part load (right) there is also an accurate agreement. The equivalent von Mises stresses σ_e on the Francis runner in two operating points for 180 MW and 60 MW are displayed in figure 11. The maximum values at 180 MW (left picture) appear with about 20 % of the yield strength σ_y at the trailing edge close to the hub of the runner. At 60 MW (right picture) the maximum stresses are lower than at full load and occur in the middle of the blade at the fillet to the hub. However, the yield strength for the runner material is not reached in any operating point and the appearing stresses are all in the elastic regime of the stress-strain curve.

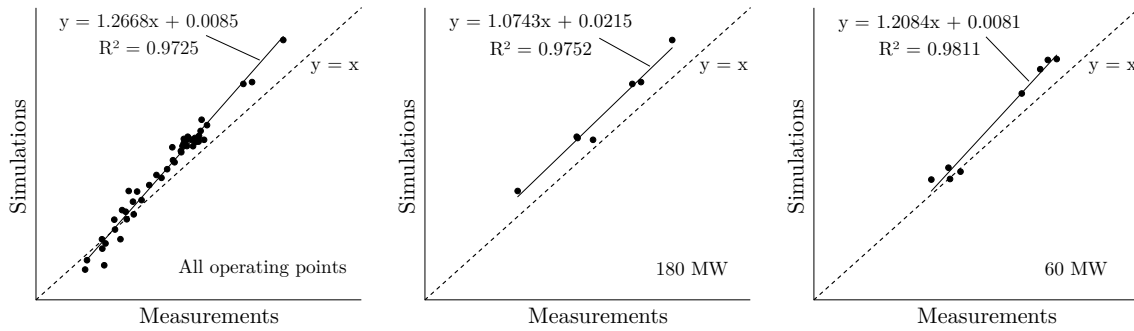


Figure 10: Linear regression analysis for the measured and computed mean stresses at all strain gauge positions for different operating points

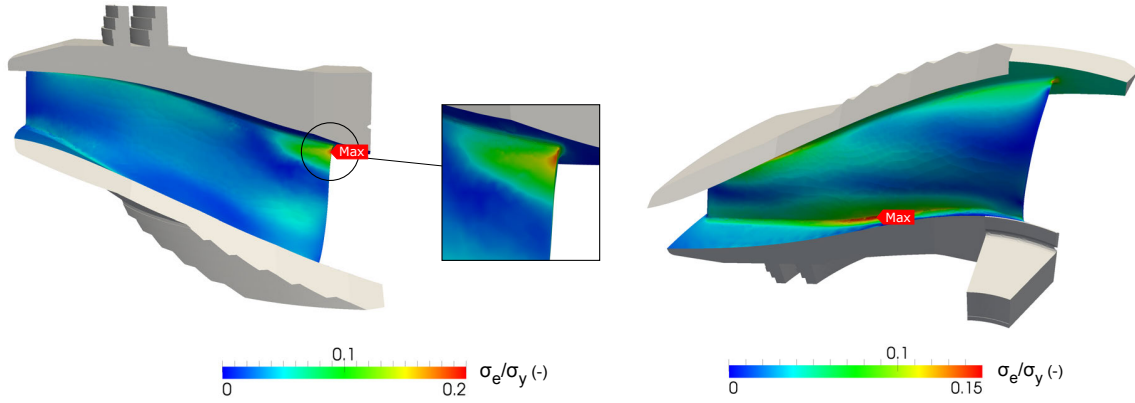


Figure 11: Equivalent von Mises stress at 180 MW (left) and 60 MW (right)

5. Conclusion

Unsteady CFD simulations and static FEM simulations have been performed for a high head prototype Francis turbine in different operating points from full load to part load conditions according to site measurements. The numerical flow analysis have been carried out using a full model including the spiral casing and a reduced model with a cyclic inlet boundary condition. Further, a grid convergence study has been performed to estimate the numerical uncertainties due to the discretization and to reduce the computational costs. The CFD results reveal a good agreement for the global parameters and small deviations from the measured head, torque and efficiency with the used OpenFOAM setup and both physical models. In order to determine the strains on the Francis runner at different operating conditions, static FEM simulations have been performed with the open-source software Code_Aster using a cyclic sector model. The results reveal a varying behavior regarding the magnitude and location of the maximum stresses due to different pressure distributions in the corresponding operating points. The accuracy of the static FEM simulations has been determined by a comparison with strain gauge measurements performed on the related prototype machine, revealing an appropriate agreement. The achieved results of the numerical investigation are further used to assess the lifetime of the Francis runner due to unsteady pressure effects like the rotor-stator interaction or draft tube instabilities, which will be discussed in future publications.

Acknowledgments

The K-Project GSG-GreenStorageGrid is funded in the framework of COMET - Competence Centers for Excellent Technologies by the Federal Ministry of Transport, Innovation and Technology, the Federal Ministry of Science, Research and Economy, the Vienna Business Agency, the Federal Province of Lower Austria and by the Federal Province of Upper Austria. The program line COMET is administered by the Austrian Research Promotion Agency (FFG). The authors would like to thank all project partners for their contribution to the research project.

The computational results presented have been achieved (in part) using the Vienna Scientific Cluster (VSC).

- [1] ETG Energy Storage Task Force. Energy storage in power supply systems with a high share of renewable energy sources: Significance, state of the art, need for action, 2008.
- [2] EASE/EERA Core Working Group. European Energy Storage Technology Development Roadmap towards 2030, 2013.
- [3] Hydro Equipment Association. Hydro Equipment Technology Roadmap, 2013.
- [4] M. V. Magnoli and M. Maiwald. Influence of Hydraulic Design on Stability and on Pressure Pulsations in Francis Turbines at Overload, Part Load and Deep Part Load based on Numerical Simulations and Experimental Model Test Results. *IOP Conference Series: Earth and Environmental Science*, 22(3):032013, 2014.
- [5] A. Coutu and J. Chamberland-Lauzon. The Impact of flexible operation on Francis runners. *International Journal on Hydropower & Dams*, Issue Two:90–93, 2015.
- [6] M. Gagnon, S. A. Tahan, P. Bocher, and D. Thibault. Impact of startup scheme on Francis runner life expectancy. *IOP Conference Series: Earth and Environmental Science*, 12:012107, 2010.
- [7] X. Huang, J. Chamberland-Lauzon, C. Oram, A. Klopfer, and N. Ruchonnet. Fatigue analyses of the prototype Francis runners based on site measurements and simulations. *IOP Conference Series: Earth and Environmental Science*, 22(1):012014, 2014.
- [8] X. Huang, C. Oram, and M. Sick. Static and dynamic stress analyses of the prototype high head Francis runner based on site measurement. *IOP Conference Series: Earth and Environmental Science*, 22(3):032052, 2014.
- [9] Q. W. Liang, S. Lais, C. Gentner, and O. Braun. Efficient runner safety assessment during early design phase and root cause analysis. *IOP Conference Series: Earth and Environmental Science*, 15(5):052009, 2012.
- [10] M. Melot, C. Monette, A. Coutu, and B. Nennemann. A new Francis runner design procedure to predict static stresses at speed-no-load. *Hydropower & Dams Issue One*, 2014.
- [11] X. F. Wang, H. L. Li, and F. W. Zhu. The calculation of fluid-structure interaction and fatigue analysis for Francis turbine runner. *IOP Conference Series: Earth and Environmental Science*, 15(5):052014, 2012.
- [12] E. Doujak and M. Eichhorn. An Approach to Evaluate the Lifetime of a High Head Francis runner. *16th International Symposium on Transport Phenomena and Dynamics of Rotating Machinery*, 2016.
- [13] B. Aakti, O. Amstutz, E. Casartelli, G. Romanelli, and L. Mangani. On the performance of a high head Francis turbine at design and off-design conditions. *Journal of Physics: Conference Series*, 579:012010, 2015.
- [14] M. Lenarcic, M. Eichhorn, S. J. Schoder, and Ch Bauer. Numerical investigation of a high head Francis turbine under steady operating conditions using foam-extend. *Journal of Physics: Conference Series*, 579:012008, 2015.
- [15] M. Lenarcic and Ch. Bauer. Numerical Investigations of the unsteady Flow in a high-head Francis Turbine using FOAM-extend. *WasserWirtschaft Extra*, 2015.
- [16] B. Celik, U. Ghia, P. Roache, Ch Freitas, H. Coleman, and P. Raad. Procedure for Estimation and Reporting of Uncertainty Due to Discretization in CFD Applications. *Journal of Fluids Engineering*, 130(7):078001, 2008.

Chapter 8

Dynamic Structural Investigations

8.1 Paper 3

In the third paper (see Tab. 8.1) the impact of different operating conditions on the dynamic excitation of a high head Francis turbine is discussed. The approach for the lifetime analysis of a Francis runner described in Chap. 6 is extended by transient FEM simulations to obtain the dynamic response induced by stochastic loads in low-load operation. The natural mode shapes and eigenfrequencies of the turbine are computed using a modal analysis. Therefore, the influence of the added mass effect of the surrounding water volume is considered and discussed. Further, a harmonic response simulation is performed in different operating points to evaluate the impact of the rotor-stator interaction on the runner. The influence of damping on the frequency response is investigated additionally. In the critical low-load operating point a transient FEM simulation is used to assess the impact of appearing draft tube vortex ropes on the dynamic excitation of the high head runner. Therefore, a simplified damping approach is considered based on the method proposed by Rayleigh. The results of the dynamic FEM simulations are compared to the prototype site measurements.

Table 8.1: Notes on Paper 3.

Title	Impact of Different Operating Conditions on the Dynamic Excitation of a High Head Francis Turbine
Authors	M. Eichhorn, E. Doujak
Conference	ASME 2016 International Mechanical Engineering Congress & Exposition (IMECE 2016)
Location	Phoenix, Arizona, USA
Date	November 11-17, 2016
Published in	Proceedings of the ASME 2016 International Mechanical Engineering Congress & Exposition

Proceedings of the ASME 2016 International Mechanical Engineering Congress & Exposition
IMECE 2016
November 11-17, 2016, Phoenix, Arizona, USA

IMECE2016-65625

IMPACT OF DIFFERENT OPERATING CONDITIONS ON THE DYNAMIC EXCITATION OF A HIGH HEAD FRANCIS TURBINE

Markus Eichhorn*

Institute for Energy Systems and Thermodynamics
TU Wien
Getreidemarkt 9/302, 1060 Vienna
Austria
Email: markus.eichhorn@tuwien.ac.at

Eduard Doujak

Institute for Energy Systems and Thermodynamics
TU Wien
Getreidemarkt 9/302, 1060 Vienna
Austria
Email: eduard.doujak@tuwien.ac.at

ABSTRACT

Fatigue analysis becomes more important in the design phase of Francis turbine runners due to the changing requirements on hydropower plants, affected by the increasing amount of volatile energy sources. Francis turbines are operated more often and over longer periods of time at off-design conditions to provide regulating power to the electric grid. The lifetime of a Francis runner depends mainly on the dynamic excitation induced by unsteady pressure pulsations like the rotor-stator interaction or draft tube vortex ropes. An approach using one-way coupled fluid-structure interactions has been developed and is now extended using unsteady CFD simulations as well as harmonic and transient FEM computations. The results are compared to strain gauge measurements on the according high head Francis turbine to validate the overall procedure. The investigations should be further used to perform a fatigue analysis and to examine the applicability for lifetime investigations on Francis machines with different specific speeds.

NOMENCLATURE

c	Speed of sound for water.
f_{BP}	Blade passing frequency.
f_0	Rotating frequency.
f_i	Eigenfrequencies.
H	Head.
k	Nodal diameter.

p	Static pressure.
p_a	Pressure amplitude.
P	Power.
PS	Pressure side.
Q	Discharge.
SS	Suction side.
z_g	Number of guide vane blades.
z_r	Number of runner blades.
$[C]$	Damping matrix.
$[K]$	Stiffness matrix.
$[M]$	Mass matrix.
α	Mass proportional Rayleigh damping coefficient.
β	Stiffness proportional Rayleigh damping coefficient.
ξ	Damping ratio.
ϕ	Guide vane angle.
ρ	Density.
σ	Stress.
σ_a	Stress amplitude.
σ_e	Equivalent von Mises stress.
σ_m	Mean stress.
σ_y	Yield strength.
ω_i	Angular eigenfrequencies.

INTRODUCTION

Fatigue analysis becomes more important even in the design phase of Francis runners due to different influences. On the one

*Address all correspondence to this author.

hand, the turbine efficiency has been gradually increased in recent years, resulting in high-end designs with a decreasing blade thickness and therefore a higher risk of crack initiation. On the other hand, the increasing amount of volatile energy sources (e.g. solar and wind) are causing significant changes in the electricity market, especially in Europe. The ability of energy storage and the provision of regulating power in a faster way becomes more important for the operators of hydropower plants. As Francis turbines can be used in a wide range of power and head, the duration and rate at off-design operation are gradually increasing. The dynamic excitation of Francis runners depends on the flow conditions inside the machine, which vary with the specific speed but also with the operating point. The stationary wicket gate causes pressure wakes, that excite the rotating runner in a harmonic way, depending on the number of guide vanes and runner blades. The so-called rotor-stator interaction (RSI) is more significant for high head Francis turbines with a lower specific speed due to the smaller gap between guide vane and turbine blades and also at full and higher part load operation (see Guillaume et al. [1] and Seidel et al. [2]). In lower part load more unstable and stochastic effects like vortex ropes or flow separation occur and increase the dynamic excitation and the influence on the lifetime of the machine. To determine the impact of the operating conditions on the runner fatigue an approach for a high head Francis turbine has been published by Doujak et al. [3]. Therefore, one-way coupled fluid-structure interactions are performed with the open-source CFD software OpenFOAM and the open-source FEM tool Code_Aster. The results are compared with strain gauge data from prototype site measurements to validate the overall procedure. According to this method the mean stresses are calculated by static FEM simulations using the time-averaged pressure from the unsteady CFD simulations. The dynamic excitations are computed using a harmonic response analysis (HRA), which is an adequate procedure to estimate the effect of the RSI, but not to consider stochastic effects. Therefore, this approach is now extended by transient FEM simulations, using the time-dependent pressure signal from the flow simulations for several runner rotations. The enhanced approach is displayed in Fig. 1. The results of the CFD analysis and the static FEM simulations have been already mentioned by Eichhorn et al. [4] but will be discussed in this paper as well. The prototype site measurements, the investigations of the harmonic response analysis and the transient structural simulations are shown in the further sections. The results of the fatigue analysis using the strain gauge data will be discussed in future publications.

PROTOTYPE SITE MEASUREMENTS

In order to evaluate the static and dynamic impact of different operating conditions on a Francis turbine, prototype site measurements have been performed using eight strain gauges on different runner positions. The investigated machine is a high

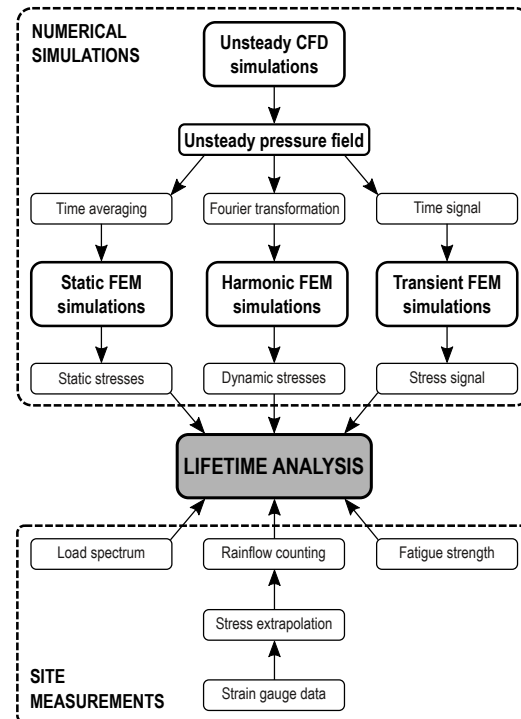


FIGURE 1: APPROACH FOR THE LIFETIME ANALYSIS OF FRANCIS RUNNERS.

head Francis turbine with a specific speed of $n_q \approx 24 \text{ rpm}$, consisting of the spiral casing, 10 stay vanes, 20 guide vanes, 15 runner blades and the draft tube. The strain gauges have been attached to one runner blade on the suction and pressure side close to the trailing edge (see Fig. 2 left). One characteristic of the hydraulic machine is the continuous shaft going through the draft tube cone, so the strain gauge data had to be stored in a casing inside the machine, which has been mounted to the rotating shaft (see Fig. 2 right). The measurements have been performed in several operating points in steps of 10 MW respectively 20 MW from the start of the machine to the maximum power of 180 MW and back again. The according operating parameters, such as the head and the output power, have been recorded as well. Additionally, the machine has been dewatered at the end of the measurements, to evaluate the stresses for the runner just rotating in air and to validate the fluid-structure investigations.

In Fig. 3 the dynamic stresses for the strain gauges SS1 and PS4 close to the shroud respectively the hub of the runner are displayed versus the power, normalized by the yield strength σ_y . To evaluate the overall dynamic excitation of the runner, the RMS

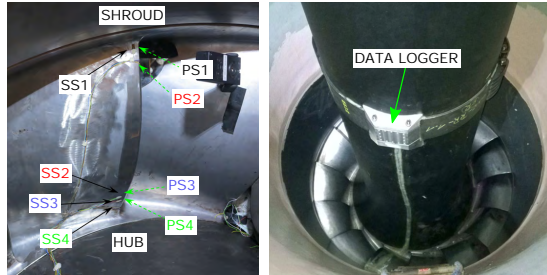


FIGURE 2: STRAIN GAUGES APPLIED TO THE FRANCIS RUNNER (LEFT) AND DATA LOGGER CASING MOUNTED ON THE SHAFT (RIGHT).

values for the stress signals are calculated over the full frequency range from $f/f_0 = 0$ to $f/f_0 = 42$, with the rotating frequency of the runner f_0 . To determine the influence of the rotor-stator interaction the RMS values at the blade passing frequency

$$f_{BP} = z_g \cdot f_0 \quad (1)$$

with the number of guide vanes z_g are calculated. Even the dynamic stresses are in a low range compared to the yield strength, there is a significant peak appearing at 60 MW for the strain gauge PS4, indicating higher dynamic excitations at the hub of the runner due to inconvenient flow conditions. The strain gauge SS1 reveals also higher peaks but these are lower compared to strain gauge PS4. The influence of the RSI is approximately equal in all operating points and smaller than the overall dynamic stresses. The values of the machine rotating in air are displayed at -5 MW power, which are quite low as expected.

The Fourier transformation of the stresses for the strain gauge PS4 reveals a nearly constant dynamic excitation of the first and the second harmonic of the blade passing frequency at $f/f_0 = 20$ and $f/f_0 = 40$ in each operating condition (see Fig. 4). At 60 MW a more stochastic behavior with higher amplitudes along the low frequency range can be observed. This operating point is therefore of special interest and will be discussed in the results of the numerical CFD and FEM simulations.

CFD SIMULATIONS

The numerical flow simulations are performed with the open-source CFD tool OpenFOAM 2.3 using the unsteady Reynolds averaged Navier-Stokes (URANS) equations. The approach and the discretization, including the grid convergence study, have been already published by Eichhorn et al. [4]. The dynamic FEM simulations described in the further sections are

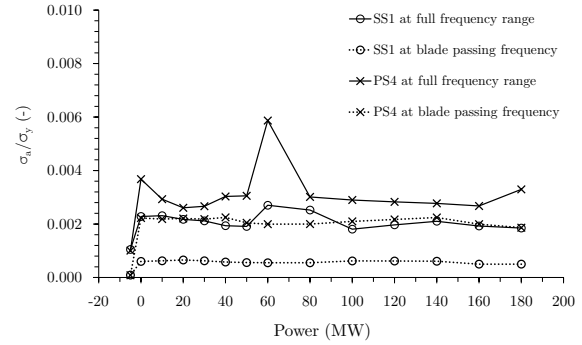


FIGURE 3: DYNAMIC STRESSES AT THE STRAIN GAUGE POSITIONS SS1 AND PS4.

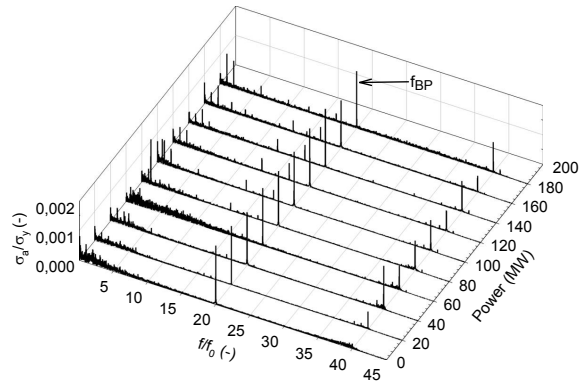


FIGURE 4: FREQUENCY SPECTRUM OF THE STRAIN GAUGE PS4 IN DIFFERENT OPERATING POINTS.

performed using the unsteady pressure field computed on the entire Francis machine. The full model consists of the spiral casing, the stay and guide vanes, the runner and the draft tube (see Fig. 5 left). The block-structured hexahedral mesh, discretized with ANSYS ICEM CFD, consists of about 5.9 million cells. The mesh for the runner and the wicket gate is displayed in Fig. 5 right. The CFD simulations are separately performed in different operating points from the maximum power output at 180 MW to low load operation at 20 MW. The parameters for the discharge Q and the guide vane angles ϕ are adjusted according to the site measurements and the mesh of the wicket gate is adapted for each operating point as well (see Tab. 1). The simulations are performed with the two-equation turbulence model $k-\omega$ SST using standard wall functions. Hence, the distance of the first wall cells in each domain is adjusted to a corresponding averaged di-

dimensionless wall distance of $y_{mean}^+ \leq 100$. The time step for the transient rotor-stator analysis is adjusted to a maximum Courant number of $Co_{max} = 15$. In low load operating points from 60 MW to 20 MW the time step is reduced to increase the accuracy of the results due to a more stochastic behavior of the flow conditions.

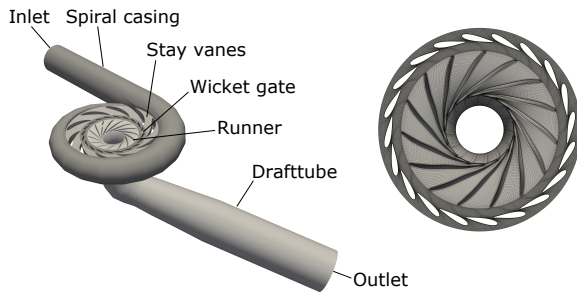


FIGURE 5: MODEL FOR THE CFD SIMULATIONS (LEFT) AND MESH FOR THE GUIDE VANES AND THE RUNNER (RIGHT).

TABLE 1: PARAMETERS FOR THE SIMULATED OPERATING POINTS WITH CFD.

Power	Rel. GV angle	Rel. discharge
P (MW)	ϕ/ϕ_{max} (-)	Q/Q_{max} (-)
180	1.000	1.000
140	0.772	0.783
100	0.576	0.582
80	0.479	0.481
60	0.382	0.378
40	0.282	0.273
20	0.173	0.164

As in the previous section discussed, the operating point at 60 MW is of special interest due to higher appearing stress amplitudes in the low frequency range. As already mentioned, the shaft of this Francis machine is going through the draft tube and therefore the behavior is slightly different compared to usual Francis machines. The analysis of the flow conditions revealed three occurring draft tube vortex ropes starting from the hub surface close to the trailing edge of the runner blades. In Fig. 6 these vortices are displayed by iso-pressure surfaces normalized by the pres-

sure of the head $\rho g H$. The vortex ropes are rotating in the runner direction with a lower rotational speed at $f/f_0 \approx 0.6$ and are fluctuating with time. The measurements revealed higher stress amplitudes especially in the hub region at lower frequencies. The slice through the draft tube cone shows an uneven pressure distribution caused by the draft tube vortices, which are the main reason for the dynamic excitation of the runner.

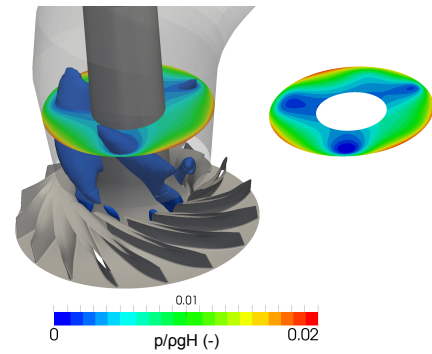


FIGURE 6: DRAFT TUBE VORTEX ROPES AT 60 MW.

The Fourier analysis of the pressure signal at a monitor point close to the strain gauge position PS4 reveals high amplitudes in the low frequency range as well (see Fig. 7). To evaluate the dynamic pressure excitation on the runner surfaces caused by different flow phenomena, the RMS values are calculated on the one hand at the blade passing frequency and on the other hand in the low frequency range from $f/f_0 = 0$ to $f/f_0 = 5$ (see Fig. 8). At the blade passing frequency the highest amplitudes are occurring at the runner inlet due to the interaction of the guide vanes and the runner blades. In the low frequency range higher excitations appear at the hub region of the runner outlet due to the draft tube vortex ropes. The impact on the dynamic stresses of the structure will be discussed in the further sections.

STRUCTURAL ANALYSIS

Static FEM simulations

To validate the approach for the fluid-structure interaction a static FEM analysis is performed with Code_Aster 11.7 to evaluate the mean stresses and the points with the highest loads. To reduce simulation time and costs, only one runner blade is considered with a cyclic boundary condition. The structure is discretized using an unstructured tetrahedral mesh with quadratic elements and about 230.000 nodes (see Fig. 9). The pressure distribution on the blade, hub and shroud surfaces from the unsteady CFD simulation is averaged over several runner rotations and ap-

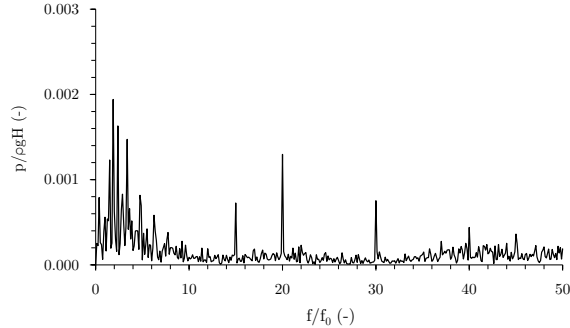


FIGURE 7: FFT ANALYSIS OF THE PRESSURE FLUCTUATIONS AT THE STRAIN GAUGE POSITION PS4.

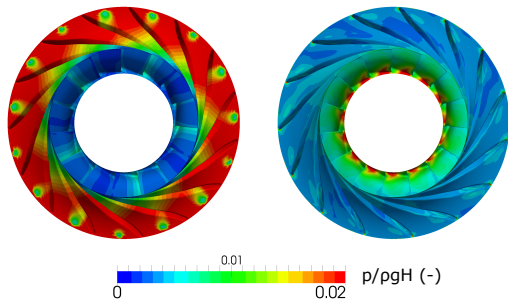


FIGURE 8: RMS VALUES OF THE PRESSURE FLUCTUATIONS ON THE RUNNER SURFACES AT THE BLADE PASSING FREQUENCY (LEFT) AND IN THE LOW FREQUENCY RANGE (RIGHT) AT 60 MW.

plied to the FEM surfaces. The pressure in the side chambers is computed analytically using the results from the CFD simulations according to the approach applied by Wachauer [5]. The runner is fixed at the upper and lower bolt circle. The E-modulus of $E = 216 \text{ kN/mm}^2$, the Poisson ratio of $\nu = 0.3$ and the density of $\rho_R = 7.700 \text{ kg/m}^3$ are used for the runner material.

The comparison of the mean stresses for the measurements and the static FEM simulations at the strain gauge positions SS1 and PS4 is displayed in Fig. 10. The stress tensors from the simulations are extracted at the nearest node for strain gauge points and transformed in their local coordinate system according to the measurements. The values for the rotation of the runner in air are displayed at -5 MW. Therefore, only the centrifugal and gravitational forces are applied on the structural model of the FEM simulations. The deviations to the measured stresses are very low and the model and the discretization are therefore accurate enough. The simulations including the CFD pressure distribution from 180 MW to 20 MW show higher stresses for

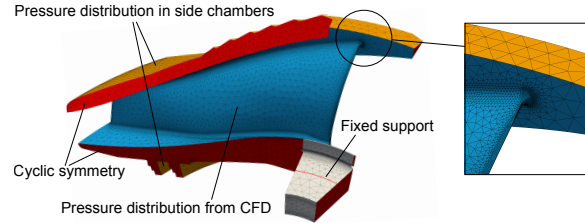


FIGURE 9: MESH AND BOUNDARY CONDITIONS FOR THE STATIC FEM SIMULATIONS.

the strain gauge SS1 in all operating points. The curve for the PS4 sensor shows higher values in full load and lower stresses in low load conditions. The deviations may result from differences in the pressure distribution computed by CFD compared to the real ones. Another possibility might be based on the analytical approach of the side chamber pressure calculation, which reveals a major influence on the mean stress values as well. The pressure distribution on the runner surfaces can only be validated by direct measurements on the prototype machine, but those are hardly realizable.

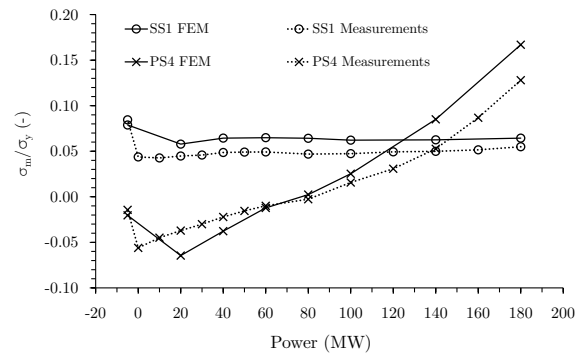


FIGURE 10: COMPARISON OF THE MEASURED AND COMPUTED MEAN STRESSES.

Figure 11 shows the equivalent von Mises stress for the operating point at 180 MW. The spot with the maximum load appears at the trailing edge close to the hub of the runner. Due to the relatively thick blade of this high head machine the values are in a low range compared to the yield strength of the material.

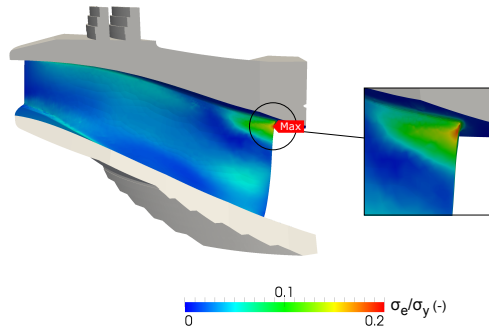


FIGURE 11: EQUIVALENT VON MISES STRESS AT 180 MW.

Natural frequencies and mode shapes

To obtain a dynamic analysis of a structure the knowledge of the natural frequencies and mode shapes is of major importance. Therefore, a modal analysis is performed using the full geometry of the Francis runner. One main impact on the mode natural frequencies is the added mass effect due to the surrounding water volume. The modes are shifted to lower frequencies compared to the runner surrounded by air as Rodriguez et al. [6] described. The shape of the considered water volume has also an influence on the natural frequencies. Comparisons between simplified rectangular or cylindrical geometries to the exact gap sizes in the runner side chambers during operation revealed only significant influences for lower modes. For high order modes with their more complex deformation shapes the impact is negligible (see Graf et al. [7]). For the harmonic response analysis only higher modes are relevant for the investigated runner, as described in the next section. Therefore, a simplified cylinder geometry is chosen for the water volume for both the modal and harmonic analysis. The mesh consists of about 500.000 nodes for the runner structure and about 300.000 for the fluid, which is modeled by acoustic elements with only one degree of freedom (DOF). At the interface between the fluid and the solid geometry the mesh is consistent. The upper and lower bolt circle and the outer surfaces of the fluid are fixed (see Fig. 12). The water properties are defined with the density $\rho_w = 1000 \text{ kg/m}^3$ and the speed of sound in water $c = 1483 \text{ m/s}$. The influence of damping is not considered for the modal analysis. Additionally, to evaluate the difference to the natural frequencies of the runner in air, a modal analysis is performed without any surrounding water volume. The modal analysis is performed up to $f/f_0 = 100$, which is five times the frequency of the RSI.

The mode shapes of the runner in water and air with the number of nodal diameters k and the according natural frequencies are displayed in the diagram in Fig. 13. It is obvious, that the water volume shifts the frequencies to lower values, especially

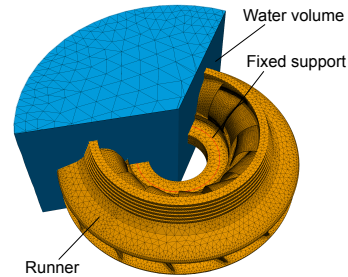


FIGURE 12: DISCRETIZATION AND BOUNDARY CONDITIONS FOR THE MODAL ANALYSIS WITH THE WATER VOLUME.

for higher order modes. The mode shapes with nodal diameters of $k = 1$ and $k = 2$ are in the range of the RSI but the critical nodal diameter of $k = 5$ is much higher at $f/f_0 \approx 80$, as it will be discussed in the next section. The modal displacements of the natural mode shapes with $k = 3$ and $k = 5$ are displayed in Fig. 13 bottom.

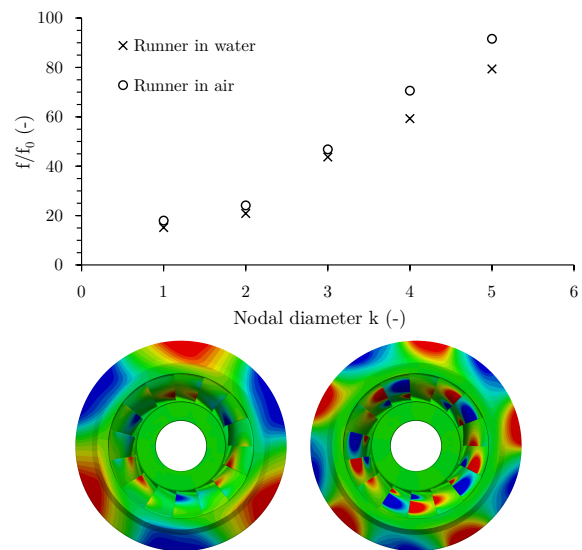


FIGURE 13: NATURAL FREQUENCIES WITH NODAL DIAMETERS k OF THE FRANCIS RUNNER IN WATER AND AIR (TOP); MODE SHAPES OF $k = 3$ (BOTTOM LEFT) AND $k = 5$ (BOTTOM RIGHT).

Harmonic response analysis

Guillaume et al. [8] showed, that the dynamic pressure field excited by the rotor-stator interaction can be described by

$$m \cdot z_r - n \cdot z_g = k \quad (2)$$

with the number of runner blades z_r and the associated harmonic index m , the number of guide vanes z_g with its harmonic index n and the corresponding nodal diameter of the pressure field k . The temporal pressure field observed in the rotor frame for any point M in a meridian section and any azimuth θ can be described in the Fourier domain by

$$p_{m,n}(M, \theta, t) = p_{m,n}(M, \theta) e^{-2i\pi \cdot n \cdot z_g \cdot f_0 \cdot t}. \quad (3)$$

The Fourier transformation at the blade passing frequency f_{BP} of all discrete points on the runner surfaces is therefore sufficient to describe the dynamic behavior excited by the RSI. The critical nodal diameter of the pressure field for the investigated Francis turbine obtained by Eqn. 2 is $k = 5$ as described in Tab. 2. The modal analysis revealed, that this natural mode shape is not in the range of the blade passing frequency and there should be no critical excitation.

TABLE 2: NODAL DIAMETER k OF THE DYNAMIC PRESSURE FIELD.

		Harmonic index n of the guide vanes		
		0	1	2
Harmonic	0	0	-20	-40
index m of	1	15	-5	-25
the runner	2	30	10	-10

The time-dependent pressure distribution on the runner surfaces obtained by the CFD simulations is transformed for each discrete point to the frequency domain using a Fourier transformation (see Fig. 14). The highest amplitudes appearing at the runner inlet and the phase shift with a nodal diameter $k = 5$ are visible.

The damping for the harmonic response analysis cannot be neglected in advance because it could have a major influence on the results of the stresses. Therefore, a frequency response analysis with the Fourier transformed pressure distribution of the RSI at 180 MW is performed. The response curves without damping

and for the low damped system, with a realistic damping ratio for Francis runners of $\xi = 0.01$ are displayed in Fig. 15. There are differences visible at two natural modes but at the blade passing frequency $f/f_0 = 20$ only marginal deviations appear. The harmonic response analysis for different operating points are further performed with the damping ratio of $\xi = 0.01$.

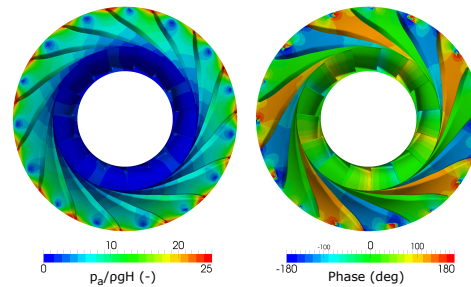


FIGURE 14: AMPLITUDE (LEFT) AND PHASE (RIGHT) OF THE FOURIER TRANSFORMED PRESSURE SIGNAL AT 180 MW.

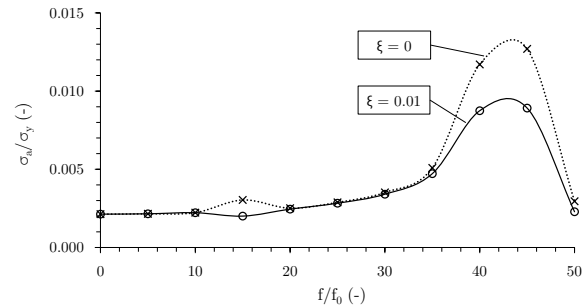


FIGURE 15: FREQUENCY RESPONSE CURVES FOR THE DAMPED AND UNDAMPED SYSTEM AT 180 MW.

The model and the boundary conditions of the harmonic response analysis are the same as for the modal simulations. Additionally, the real and imaginary part of the pressure distribution from the Fourier transformation are applied to the blade, hub and shroud surfaces. One runner blade is refined similar to the static analysis to accurately evaluate the appearing stresses. The comparison of the dynamic stresses for the strain gauges SS1 and PS4 in Fig. 16 shows higher dynamic amplitudes for both sensors for each operating point, but regarding the yield strength the amplitudes are quite low. The maximum stresses are appearing with $\sigma_a/\sigma_y \approx 0.01$ at the notch between the blade and the shroud at

the leading edge of the runner, as expected for the RSI (see Fig. 17).

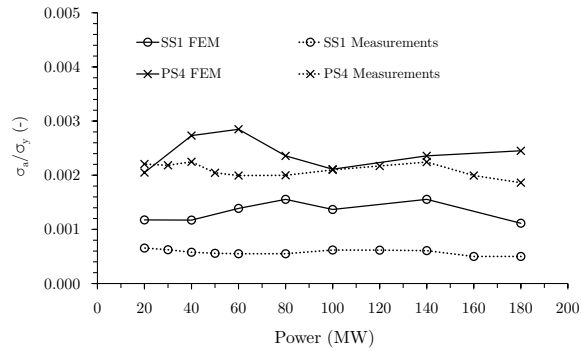


FIGURE 16: COMPARISON OF THE MEASURED AND COMPUTED DYNAMIC STRESSES AT THE STRAIN GAUGES SS1 AND PS4.

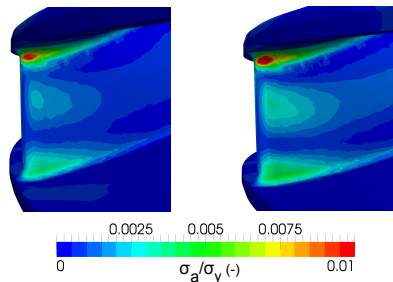


FIGURE 17: STRESS AMPLITUDES COMPUTED BY THE HRA AT 180 MW (LEFT) AND 60 MW (RIGHT).

Transient FEM simulations

To investigate the dynamic behavior of the Francis runner not only regarding the impact of the rotor-stator interaction but also in the full frequency range, a transient FEM analysis is performed for the critical operating point at 60 MW. Due to the appearing draft tube vortex ropes, the pressure distribution in the circumferential direction cannot be assumed to be uniform. Therefore, the full model of the runner has to be considered. In order to decrease the size of the mesh, only one runner blade is refined in the notches and at the trailing edge, similar to the HRA analysis. The mesh with a number of approximately 500,000

nodes and the boundary conditions are displayed in Fig. 18. The water volume around the runner is not regarded for the transient analysis to simplify the model. Similar to the static FEM analysis, the pressure distribution in the side chambers is considered instead. The runner is fixed at the nodes for the upper and lower bolt circle. At the blade, hub and shroud region, the pressure from the CFD analysis is mapped for each time step to the structural mesh.

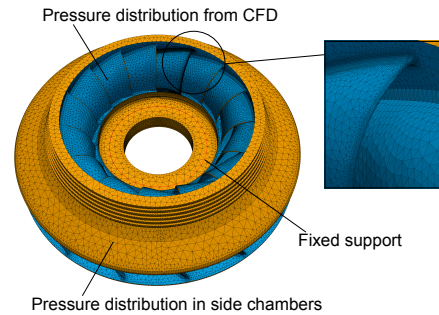


FIGURE 18: MESH AND BOUNDARY CONDITIONS FOR THE TRANSIENT FEM ANALYSIS.

The time step is chosen to 3.6° of runner rotations and the simulation is performed for 10 rotations, which yields a total number of 1000 time steps. The direct time integration method proposed by Newmark [9] together with an iterative solver is used for the transient simulations, yielding a moderate required amount of time and memory. The advantage of the transient FEM simulations is, that the time-dependent pressure distribution of any operating point can be used without any simplifications. Even speed-no-load or start-up calculations could be performed. In contrast to the harmonic response analysis the consideration of an accurate damping is of major importance for the transient calculations due to the complex behavior of the structure depending on the frequency range. As the knowledge about the damping of Francis runners in water is still limited a simplified approach using an equivalent Rayleigh damping in the form of

$$[C] = \alpha [M] + \beta [K] \quad (4)$$

is used, with the damping matrix $[C]$, the mass matrix $[M]$, the stiffness matrix $[K]$ and the Rayleigh coefficients α and β . Considering the damping ratio ξ the Rayleigh coefficients can be also described by

$$2\xi_i = \frac{\alpha}{\omega_i} + \beta\omega_i \quad (5)$$

for each value of the angular eigenfrequency $\omega_i = 2\pi f_i$. Clough et al. [10] proposed an approach to calculate the Rayleigh coefficients between two frequencies by

$$\begin{Bmatrix} \alpha \\ \beta \end{Bmatrix} = 2 \frac{\omega_1 \omega_2}{\omega_2^2 - \omega_1^2} \begin{bmatrix} \omega_2 & -\omega_1 \\ -\frac{1}{\omega_2} & \frac{1}{\omega_1} \end{bmatrix} \begin{Bmatrix} \xi_1 \\ \xi_2 \end{Bmatrix}. \quad (6)$$

Chowdhury et al. [11] suggested to determine the fundamental frequencies ω_1 and ω_2 by considering the mass participation of the low frequency modes. According to this, the Rayleigh coefficients are calculated regarding the eigenfrequencies and the cumulative mass participation from the modal analysis to $\alpha = 0.625$ and $\beta = 0.8e^{-5}$. This yields a damping ratio of $\xi \leq 0.02$ in a frequency range of $2 \leq f/f_0 \leq 40$ and higher damping ratios outside this range.

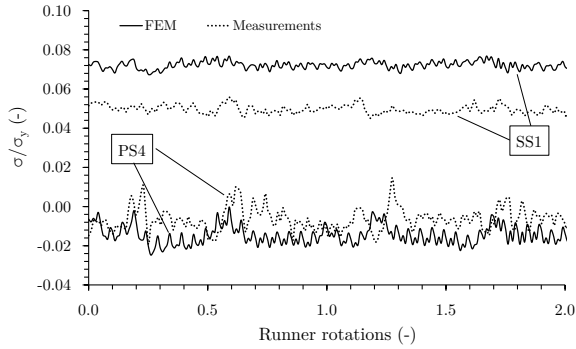


FIGURE 19: COMPARISON OF THE MEASURED AND COMPUTED STRESSES AT THE STRAIN GAUGE POSITIONS SS1 AND PS4 AT 60 MW.

In Fig. 19 the stresses at the strain gauge positions SS1 and PS4 at 60 MW are displayed for the site measurements and the transient FEM simulation for two runner rotations. Similar to the static FEM analysis a shift of the signals is visible but the characteristics of the calculated stress-time curves are well predicted. The stress amplitudes at the strain gauge PS4 are higher than for the strain gauge SS1 (as already mentioned in the previous sections) due to the draft tube vortices appearing at the hub

of the runner. The FFT analysis of the stress signals (see Fig. 20) reveals the first and the second harmonic of the blade passing frequency for both strain gauges. Higher amplitudes are appearing as well in the low frequency regime, especially at the sensor position PS4, excited by the pressure oscillations in the draft tube cone. It is obvious that the FEM simulations are overestimating the stresses compared to the measurements. One reason could be the influence of the water volume around the runner, which has been neglected for the transient computations in order to reduce the amount of required resources. Additional investigations will be performed in the future to evaluate this impact. The results of the transient FEM simulations are further used for a fatigue analysis to determine the influence of different operating conditions on the lifetime of this high head Francis runner and to evaluate the applicability of the developed approach for other Francis turbines.

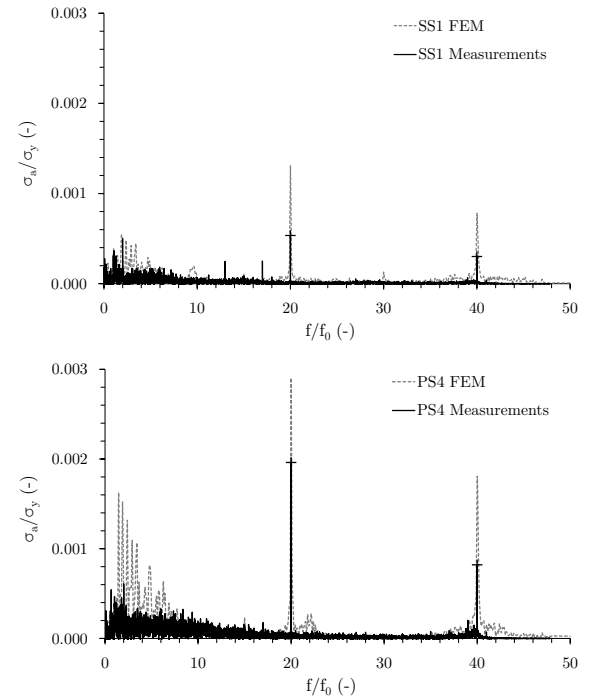


FIGURE 20: FFT ANALYSIS OF THE COMPUTED AND MEASURED STRESSES AT THE STRAIN GAUGES SS1 (TOP) AND PS4 (BOTTOM) AT 60 MW.

CONCLUSION

An approach for the lifetime analysis of Francis runners has been developed and extended. Therefore, prototype site measurements on a high head Francis turbine using strain gauges on different blade positions have been performed. The results reveal a noticeable operating point with higher dynamic excitations at about 30 % of the full power output. Unsteady CFD simulations at this low-load operation show vortex ropes appearing in the draft tube cone inducing pressure pulsations on the runner surfaces. Static FEM simulations in several operating points have been used to validate the method for the applied fluid-structure interaction showing accurate results according to the measurements. The natural frequencies and mode shapes of the runner have been obtained by a modal analysis considering the influence of the added mass effect due to the surrounding water volume. The results reveal a shift to lower frequencies compared for the runner surrounded by air, especially for higher order modes. The influence of the rotor-stator interaction has been investigated by a harmonic response analysis using the Fourier transformed pressure distribution from the CFD simulations. The FEM computations show accurate results with a similar behavior for different operating conditions. The appearing stress amplitudes are at about 1 % of the yield strength of the runner material and are therefore in a non-critical range. To investigate the lifetime of the Francis turbine considering not only the RSI but also more stochastic effects, a transient FEM analysis in the low-load operating point has been performed using the direct time integration method. The influence of damping has been regarded using Rayleigh coefficients calculated by the results of the modal analysis. The comparison of the computed and measured stress signals at the strain gauge positions shows an accurate accordance. Further investigations will deal with the fatigue analysis using the results of the transient FEM simulations, to evaluate the applicability for the lifetime calculations of this and other Francis turbines. The impact of more advanced turbulence models in low-load operation and the sensitivity of the whole approach considering further influences (e.g. geometrical deviations or model simplifications) will be discussed in future publications as well.

ACKNOWLEDGMENT

The K-Project GSG-GreenStorageGrid is funded in the framework of COMET - Competence Centers for Excellent Technologies by the Federal Ministry of Transport, Innovation and Technology, the Federal Ministry of Science, Research and Economy, the Vienna Business Agency, the Federal Province of Lower Austria and by the Federal Province of Upper Austria. The program line COMET is administered by the Austrian Research Promotion Agency (FFG).

The authors would like to thank the project partners Andritz Hydro, Verbund Hydro Power, ZT Hirtenlehner, TIWAG Tiroler Wasserkraft AG and Vorarlberger Illwerke AG for their contri-

bution in the course of the sub-project PSP-LowLoad. Special thanks goes to Andritz Hydro for their support regarding the application of Code_Aster. The computational results presented have been achieved in part using the Vienna Scientific Cluster (VSC).

REFERENCES

- [1] Guillaume, R., and Deniau, J., 2011. "Rotor-stator interaction in high head pump turbines: dynamic response of the structure". *Hydro 2011 (Prague, Czech Republic)*.
- [2] Seidel, U., Hübner, B., Löfflad, J., and Faigle, P., 2012. "Evaluation of RSI-induced stresses in Francis runners". *IOP Conference Series: Earth and Environmental Science*, **15**(5), p. 052010.
- [3] Doujak, E., and Eichhorn, M., 2016. "An Approach to Evaluate the Lifetime of a High Head Francis runner". *16th International Symposium on Transport Phenomena and Dynamics of Rotating Machinery*.
- [4] Eichhorn, M., and Doujak, E., 2016. "Investigation of the fluid-structure interaction of a high head Francis turbine using OpenFOAM and Code_Aster". *28th IAHR symposium on Hydraulic Machinery and Systems*.
- [5] Wachauer, M., 2014. "Unidirektionale Fluid-Struktur-Kopplung am Beispiel eines Pumpturbinenlaufrades mit besonderer Betrachtung unterschiedlicher Radseitenraummodelle". *Bachelor Thesis, TU Wien, Institute for Energy Systems and Thermodynamics*.
- [6] Rodriguez, C. G., Egusquiza, E., Escaler, X., Liang, Q. W., and Avellan, F., 2006. "Experimental investigation of added mass effects on a Francis turbine runner in still water". *Journal of Fluids and Structures*, **22**(5), pp. 699–712.
- [7] Graf, B., and Chen, L., 2010. "Correlation of Acoustic Fluid-Structural Interaction Method for Modal Analysis with experimental results of a Hydraulic Prototype Turbine Runner in Water". *Proceedings of ISMA2010 including USD2010*.
- [8] Guillaume, R., Deniau, J. L., Scolaro, D., and Colombet, C., 2012. "Influence of the rotor-stator interaction on the dynamic stresses of Francis runners". *IOP Conference Series: Earth and Environmental Science*, **15**(5), p. 052011.
- [9] Newmark, N. M., 1959. "A Method of Computation for Structural Dynamics". *ASCE Journal of Engineering Mechanics Division*, **85**, pp. 67–94.
- [10] Clough, R. W., and Penzien, J., 1995. *Dynamics of Structures*, 3 ed. Computers & Structures, Inc., Berkeley, USA.
- [11] Chowdhury, I., and Dasgupta, S. P., 2003. "Computation of Rayleigh Damping Coefficients for Large Systems". *Electronic Journal of Geotechnical Engineering*.

Chapter 9

Fatigue Analysis

9.1 Paper 4

In the fourth paper (see Tab. 9.1) the influence of low-load operation on the structural impact of a medium head prototype Francis turbine is investigated. Therefore, unsteady CFD simulations are performed with OpenFOAM using two different turbulence models: The $k-\omega$ SST model and the hybrid RANS-LES turbulence model SAS. The influence on the global parameters but also on the mean pressure distribution and the dynamic pressure fluctuations at the runner are obtained. The results are used for static FEM simulations in different operating conditions performed with Code_Aster and compared to strain gauge measurements on the according prototype machine. Further, the dynamic excitations of the Francis runner in low-load operation are assessed using transient FEM simulations with the CFD results of both turbulence models. To investigate the fatigue impact on the structure a rainflow counting analysis is performed for the measured and computed stresses to evaluate the accuracy of the fluid-structure simulations.

Table 9.1: Notes on Paper 4.

Title	Fatigue Analysis of a Medium Head Francis Runner at Low-Load Operation Using Numerical Investigations
Authors	M. Eichhorn, L. Waldner, C. Bauer
Conference	19th International Seminar on Hydropower Plants (Vienna Hydro 2016)
Location	Vienna, Austria
Date	November 9-11, 2016
Published in	Proceedings of the 19th International Seminar on Hydropower Plants

FATIGUE ANALYSIS OF A MEDIUM HEAD FRANCIS RUNNER AT LOW-LOAD OPERATION USING NUMERICAL INVESTIGATIONS

M. Eichhorn, L. Waldner, C. Bauer

Abstract: The changing requirements on hydropower plants due to an increasing amount of volatile energy sources are forcing the operators to deliver regulating power in a faster way. Hence, especially Francis turbines are operated more often at off-design conditions, which involve the appearance of unsteady flow phenomena. This leads to an increasing excitation of the runner structure and to a distinct impact on the lifetime of the turbine. Therefore, a fatigue analysis on a medium head Francis runner, using CFD and FEM simulations, is performed and compared to prototype site measurements, to investigate the capabilities of the numerical computations.

1 Introduction

The lifetime assumption of Francis turbine runners is becoming more important, even in the design phase of the hydraulic machine. Power plant operators are forced to deliver an increasing amount of regulating power in a faster way, to compensate the volatility of solar and wind power. Hence, the requirements on the machine components, especially for the runner, are getting more complex due to varying dynamic excitations of the structure at off-design conditions. To estimate the influence of different operating conditions on the lifetime of a turbine runner, an approach has already been published using numerical fluid-structure investigations combined with site measurements on a high head Francis machine (see [1]). This approach is now used for a medium head Francis runner with a specific speed of $n_q \approx 52 \text{ rpm}$, to determine the overall applicability. The results of the numerical simulations presented in this paper are compared to prototype site measurements, which have been published in [2]. The unidirectional fluid-structure interaction consists of unsteady CFD simulations, to compute the pressure distribution and oscillation in the Francis turbine and of static and transient FEM simulations, to evaluate the stresses appearing on the runner.

2 CFD Simulations

2.1 Numerical setup and discretization

The CFD simulations are performed using the URANS (unsteady Reynolds averaged Navier-Stokes) equations with the open-source code OpenFOAM. The turbulence is modelled with the $k-\omega$ SST model for all investigated operating points, ranging from low-load at 6 MW to full load at 20 MW. Additionally, to determine the influence of the turbulence model on the unsteady pressure fluctuations, the $k-\omega$ SST based Scale

Adaptive Simulation (SAS) approach is used for the best efficiency operating point (BEP) at 16 MW and at low-load operation at 6 MW. Several authors like Magnoli [3] or Nennemann et al. [4] showed the applicability of the SAS approach in the field of the simulation of Francis turbines. The computational domain, a full Francis turbine geometry containing the spiral casing (SC), the stay vanes (SV) and guide vanes (GV), the runner (RN) and the draft tube (DT), is discretized using ANSYS ICEM CFD and TurboGrid (see Fig. 1 left). To keep the mesh size in a low range, standard wall functions are used. Therefore, the first wall cell distance is set to a corresponding averaged dimensionless wall distance of $y^+_{mean} \leq 300$. Table 1 shows an overview about the mesh size and the quality of each CFD domain (the required values are stated as well). The full mesh consists of about 9 Mio. cells. The domains are coupled at the non-conformal interfaces (IF) using the arbitrary mesh interface (AMI) approach implemented in OpenFOAM (see Fig. 1 right).

Table 1: CFD mesh size and quality

	SC	SV	GV	RN	DT	required
Number of cells (Mio.)	0.74	0.96	3.19	3.32	0.51	-
Minimum determinant (-)	0.22	0.40	0.44	0.46	0.55	≥ 0.2
Minimum angle (°)	11.2	21.0	17.2	21.6	30.5	≥ 10
Minimum aspect ratio (-)	0.001	0.005	0.002	0.001	0.001	≥ 0.001

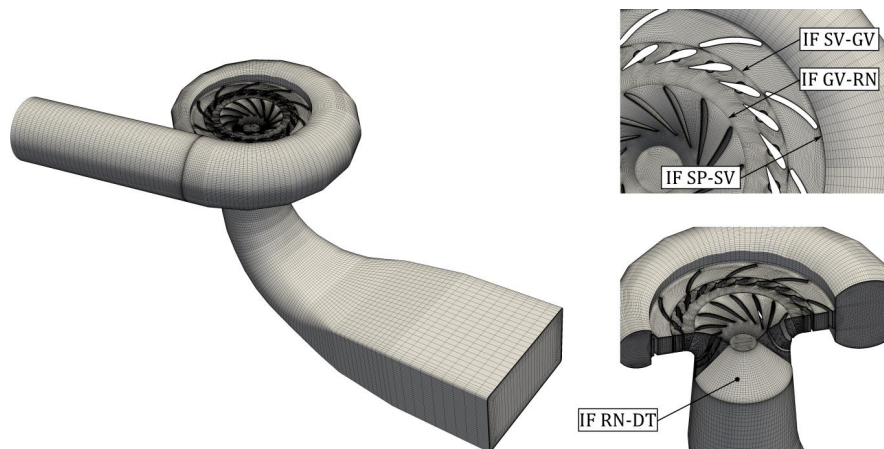


Fig. 1: Discretization of the CFD model (left) and interfaces between the mesh domains (right)

The simulations are performed in several operating points using the PIMPLE solver in combination with a second order Euler temporal discretization. The discharge Q at the inlet and the guide vane blade angle ϕ are adapted for each operating point (see Table 2). The time step size is chosen to a corresponding runner rotation of 0.6° resulting in a maximum Courant number of $Co_{max} \approx 52$ for all operating points. A fixed number of 12 inner iteration loops per time step is used to reach a sufficient convergence rate. The advection scheme is chosen to be of second order accuracy. A converged stationary solution is used as an initial condition for each operating point. The simulations are performed for at least ten runner rotations to guarantee

convergence of the mean values of interest and to obtain reliable results for the further structural analysis. The fluid is considered to be incompressible and of single phase type.

Table 2: Boundary conditions for the CFD simulations

Nominal Power P (MW)	Rel. GV angle ϕ/ϕ_{BEP} (-)	Rel. discharge Q/Q_{BEP} (-)
6	0.48	0.47
8	0.56	0.56
12	0.79	0.79
16	1.00	1.00
20	1.31	1.23

To define the inlet turbulence, values for k and ω according to a turbulent intensity of $I = 10\%$ and a turbulent mixing length of $l_m = 0.125\text{ m}$ are set at the spiral inlet. An averaged static pressure condition is defined at the outlet. The setup and the boundary conditions for the CFD simulations are summarized in Table 3.

Table 3: Numerical setup for the CFD simulations

Parameters	Description
Software	OpenFOAM 2.3
Analysis type	Transient rotor-stator
Turbulence models	$k-\omega$ SST / SAS
Mesh Size	≈ 9 Mio. cells
Wall treatment	Standard wall functions
Time step	0.6° runner rotations
Max. Courant number	$Co_{\max} \approx 52$
Advection scheme	Second order
Simulation time	≥ 10 runner rotations
Inlet BC	Discharge, turbulence quantities
Outlet BC	Averaged static pressure

2.2 Results of the CFD simulations

In order to evaluate the accuracy of the CFD model and setup, the integral quantities head, power and efficiency are compared to the measured results at the BEP (see Fig. 2 left). The deviations from the measured values are below 5% for both turbulence models. Fig. 2 right shows the computed efficiencies normalized to the measured efficiency at the BEP obtained by the $k-\omega$ SST model in all operating points and by the SAS model at 16 MW and 6 MW. All quantities are averaged over a period of several runner rotations.

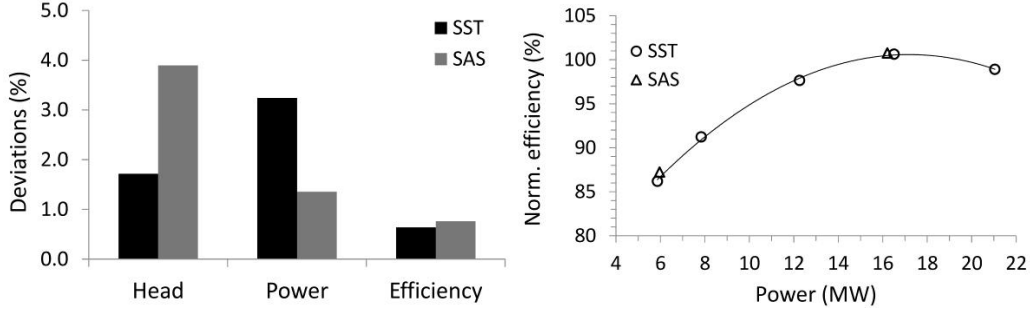


Fig. 2: Deviations of the computed quantities head, power and efficiency from the measured values at the BEP (left) and normalized efficiency curve of the CFD simulations (right)

To assess the capability of the two mentioned turbulence models, the unsteady behaviour of the pressure field on the runner blade surface, which is essentially for the stress integrity study in the following section, is evaluated. Therefore, the mean pressure distribution p_{mean} and the pressure fluctuation Δp defined by

$$\Delta p = \sqrt{p'^2} = \sqrt{[(p(t) - p_{mean})^2]}$$

are obtained along the blade profile at 6 MW low-load operation. The results indicate that the distribution of the mean pressure p_{mean} is almost similar for both, the $k-\omega$ SST and the SAS turbulence model, from the leading edge at the normalized chord length $c_x/s = 1$ to the trailing edge at $c_x/s = 0$ (see Fig. 3 left). In contrast, the distribution of the pressure fluctuation Δp behaves very different for the two turbulence models (see Fig. 3 right). The SAS model reveals higher amplitudes especially at the suction side of the runner blade, with values of nearly 30 times of the amplitudes computed with the SST model.

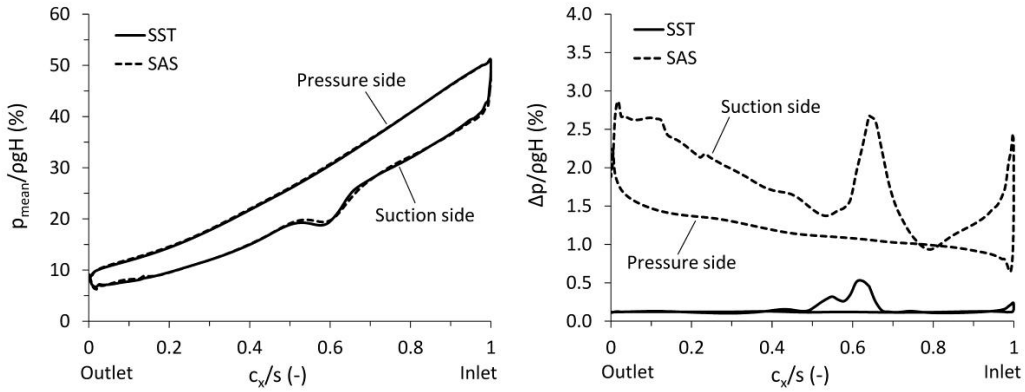


Fig. 3: Normalized mean pressure distribution p_{mean} (left) and pressure fluctuations Δp (right) along the normalized runner blade chord length c_x/s computed with the SST and SAS turbulence model at 6 MW

Both simulations show a peak of the pressure fluctuation at the mid range of the profile, which is caused by the presence of a runner channel vortex at this operating point. Very high peaks of the pressure fluctuation are also located near the leading

edge due to the rotor-stator interaction and at the trailing edge region generated by draft tube vortices. The impact of the CFD results of both turbulence models on the runner structure is investigated in the following sections.

3 Structural analysis

To investigate the influence of the fluid flow on the runner structure in different operating conditions, static and transient FEM simulations are performed. The results of the mean stresses and the stress amplitudes are further used for a fatigue analysis in the critical operating point at 6 MW, which has been determined by the prototype site measurements (see [2]).

3.1 Static FEM Simulations

3.1.1 Numerical setup and discretization

To evaluate the overall load and the mean stresses on the runner, static FEM computations are performed with the open-source tool Code_Aster. Therefore, a cyclic sector model consisting of one runner blade and the hub and shroud regions is used, to reduce the simulation time (see Fig. 4).

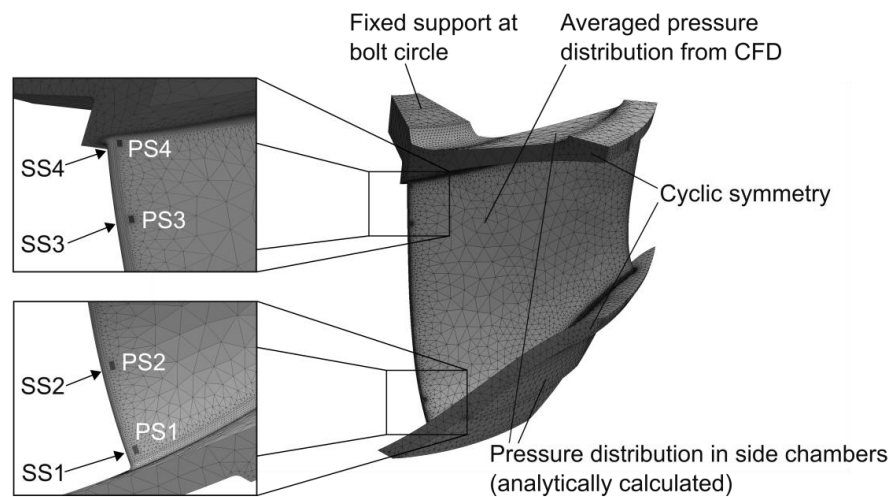


Fig. 4: Mesh and boundary conditions for the static FEM simulations and position of the strain gauges

The unstructured tetrahedral mesh consists of about 160 thousand nodes with second order elements and a quadratic interpolation function, to increase the accuracy. The pressure distribution from the CFD simulations is averaged over several runner rotations and applied to the nodes of the blade, hub and shroud surfaces. The pressure in the side chambers is analytically calculated. The runner is fixed at the upper and lower bolt circles and a cyclic symmetry boundary condition is applied at the sector interfaces. The centrifugal forces are considered as well. To validate the results of the FEM simulations, the stress values at several nodes close to the strain gauge positions are averaged and compared to the measurements.

3.1.2 Results

The results of the static FEM simulations using the mean pressure distribution of the SST and SAS turbulence model and the measurements at the two strain gauge positions PS4 and SS4 are displayed in Fig. 5. The computed mean stresses σ_m normalized to the yield strength of the runner material σ_y show an accurate correlation compared to the measured values. Only at full-load operation the stress values of the FEM analysis reveal slightly higher deviations for both turbulence models.

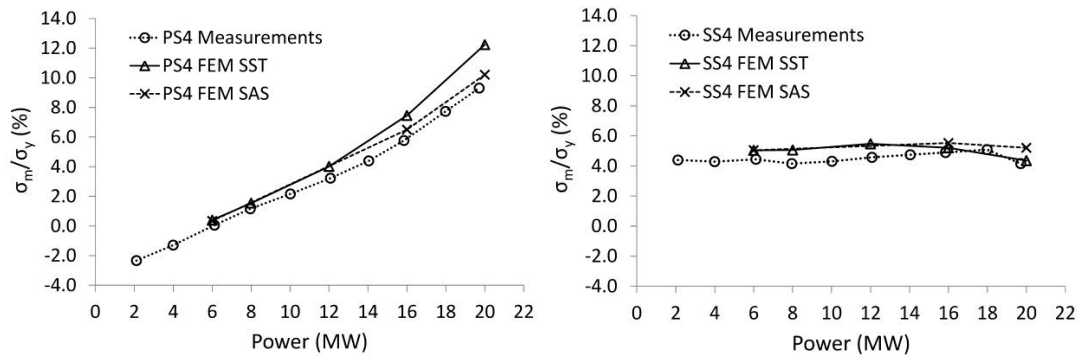


Fig. 5: Comparison of measured and computed mean stresses at strain gauge positions PS4 (left) and SS4 (right)

3.2 Transient FEM Simulations

3.2.1 Numerical setup and discretization

To evaluate the dynamic stress amplitudes and the highest excitations of the runner, transient FEM simulations are performed at the critical low-load operating point at 6 MW. Therefore, the full runner geometry is used (see Fig. 6) as the pressure distribution cannot be assumed to be uniform in the circumferential direction.

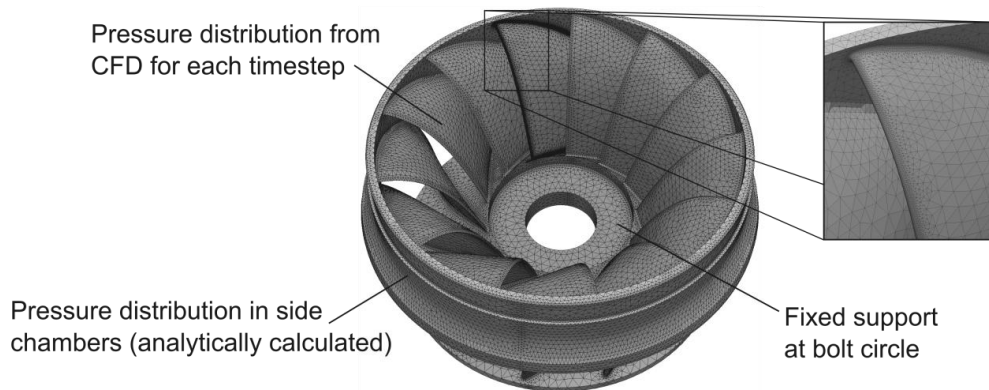


Fig. 6: Mesh and boundary conditions for the transient FEM simulations

To reduce the simulation time and the needed resources, only one runner blade is refined at the notches and the leading and trailing edge regions. The mesh consists of about 0.6 million nodes. The pressure distribution from the unsteady CFD simulations is applied for each timestep to the blade, hub and shroud surfaces. The computation is performed for five rotations and the time step is chosen to a corresponding runner rotation of 3.0° . Similar to the static simulations, the runner is fixed at the bolt circles. The pressure distribution in the side chambers is analytically calculated and the centrifugal forces are considered as well. To validate the results of the computations the stress values at the strain gauge positions are compared to the measurements.

3.2.2 Results

As the CFD simulations revealed significant differences regarding the pressure fluctuations due to the turbulence modelling, the transient FEM simulations are performed using the results of the SST and the SAS model as well. The comparison of the measured and computed stress amplitudes, obtained by the RMS values of the stress signals, at 6 MW at all strain gauge positions is displayed in Fig. 7 left. The pressure distribution from the SAS model delivers much more accurate results than the one from the SST model, which is underpredicting each measured value. The FFT analysis of the most critical position PS4 (see Fig. 7 right) shows, that the signal obtained by the SST model only contains an excitation at the rotating frequency $f/f_0 = 1$. The measurements and also the results of the SAS model indicate a high peak at $f/f_0 \approx 0.8$ due to pressure fluctuations induced by draft tube vortices.

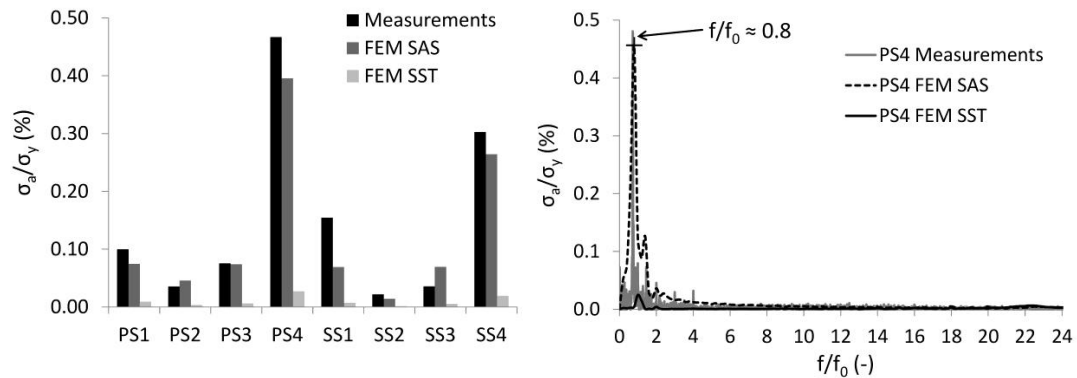


Fig. 7: Comparison of measured and computed dynamic stress amplitudes (left) and FFT analysis at strain gauge position PS4 (right) at 6 MW

4 Fatigue analysis

The dynamic stress amplitudes at one runner blade normalized to the yield strength are displayed in Fig. 8 left. The highest values are appearing at the notch to the hub at the trailing edge region with $\sigma_a/\sigma_y = 1.1$ %. To determine the impact on the lifetime of the runner a fatigue analysis using the rainflow counting algorithm is performed.

Therefore, the measured and computed stresses at the strain gauge position PS4 and the multiaxial stress signal at the critical notch are used. As the time scale length of the computed signals is much lower than the measured ones and to obtain more reliable results, an extrapolation method based on the extreme value theory described in [5] is used. This approach has been successfully applied for a fatigue analysis on a Francis runner at no-load operation (see [6]). The signals of the measurements and the simulations are therefore extrapolated to a time duration of 1000 s. For the fatigue analysis of the multiaxial stress state in the notch, the stress-based Brown Miller algorithm is used, which considers the damage by a combination of the shear and normal stresses (see [7]). The influence of the mean stress on the fatigue lifetime is regarded by the Goodman model. The results of the fatigue analysis are displayed in Fig. 8 right. The stress-cycle curve for the computed stresses at the strain gauge location PS4 is underestimating the measured results, but the tendency shows an accurate correlation. The results at the critical location in the notch reveal higher values than the measured curve, as expected. In comparison to the S-N curve of the runner material, the measured and computed stresses are below the fatigue limit.

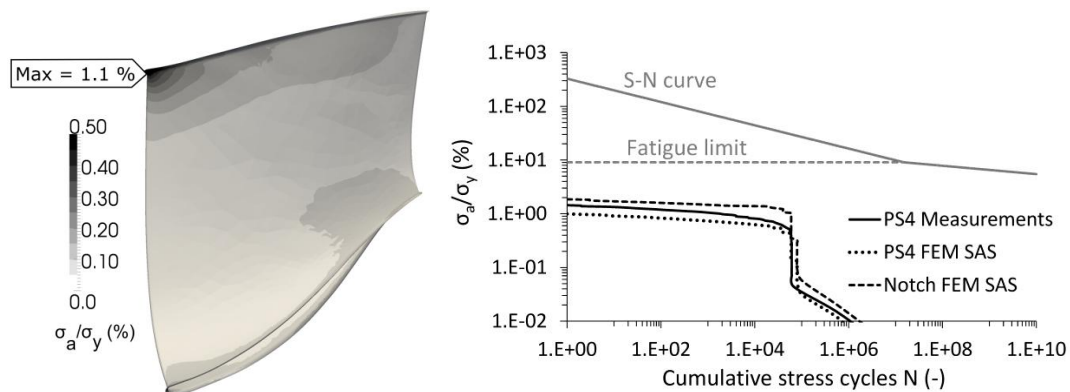


Fig. 8: Stress amplitudes at one runner blade at 6 MW computed with the SAS model (left) and stress-life curves of the measured and computed signals at 6 MW (right)

5 Conclusions

To investigate the fatigue lifetime of a medium head Francis runner, fluid-structure investigations have been performed using unsteady CFD simulations on the entire hydraulic machine as well as static and transient FEM simulations. To evaluate the influence of the turbulence models, the $k-\omega$ SST and the SAS model have been used for the flow simulations. The results show marginal influence on the mean pressure distribution along the runner blade profile, but distinct impact on the pressure fluctuation due to channel and draft tube vortices. The comparison with strain gauge measurements on the according prototype machine reveal an accurate agreement with the computed mean stresses at different runner locations in several operating points for both turbulence models. Considering the transient FEM simulations at the critical operating point at 6 MW, the SAS model shows a much more precise prediction of the stress amplitudes and the FFT analysis. The computed and measured stress signals were further applied for a fatigue analysis using the rainflow

counting algorithm together with an extrapolation method based on the extreme value theory. Further, the multiaxial stresses at the critical runner location have been obtained for the lifetime analysis. The results show an accurate agreement with the measurements delivering stress-life curves below the fatigue limit of the runner material. Although the investigations proof the applicability of the used approach for a fatigue analysis, the remaining uncertainties (e.g. material inhomogeneity, numerical simplifications and limitations, turbulence modelling, geometrical discrepancies,...) must be considered for a reliable lifetime assessment.

Acknowledgments

The K-Project GSG-GreenStorageGrid is funded in the framework of COMET – Competence Centers for Excellent Technologies by the Federal Ministry of Transport, Innovation and Technology, the Federal Ministry of Science, Research and Economy, the Vienna Business Agency, the Federal Province of Lower Austria and by the Federal Province of Upper Austria. The program line COMET is administered by the Austrian Research Promotion Agency (FFG). The authors would like to thank the project partners Andritz Hydro, Verbund Hydro Power, ZT Hirtenlehner, TIWAG Tiroler Wasserkraft AG and Vorarlberger Illwerke AG for their contribution in the course of the sub-project PSP-LowLoad. Special thanks goes to Andritz Hydro for their support regarding the application of Code Aster. The authors would also like to thank Dr. Eduard Doujak for his support in the course of the project. The computational results presented have been achieved in part using the Vienna Scientific Cluster (VSC).

References

- [1] M. Eichhorn, E. Doujak: "Impact of different operating conditions on the dynamic excitation of a high head Francis turbine". Proceedings of the ASME 2016 International Mechanical Engineering Congress & Exposition. Phoenix, 2016.
- [2] J. Unterluggauer, M. Eichhorn, E. Doujak: "Fatigue analysis of Francis turbines with different specific speeds using site measurements". Proceedings of the 19th International Seminar on Hydropower Plants. Vienna, 2016.
- [3] M. V. Magnoli: "Numerical simulation of pressure oscillations in large Francis turbines at partial and full load operating conditions and their effects on the runner structural behaviour and fatigue life". PhD-Thesis, Technische Universität München, 2014.
- [4] B. Nennemann et al.: "Challenges in Dynamic Pressure and Stress Predictions at No-Load Operation in Hydraulic Turbines". IOP Conference Series: Earth and Environmental Science; 22(3):032055, 2014.
- [5] P. Johannesson: "Extrapolation of load histories and spectra". Fatigue & Fracture of Engineering Materials & Structures. Volume 29, Issue 3, pp. 209 – 217, March 2006.

- [6] J. F. Morissette, J. Chamberland-Lauzon, J. F. Morissette, J. Chamberland-Lauzon, B. Nennemann, C. Monette, A. M. Giroux, A. Coutu and J. Nicolle: "Stress predictions in a Francis turbine at no-load operation". 28th IAHR Symposium on Hydraulic Machinery and Systems. Grenoble 2016
- [7] M. W. Brown and K. J. Miller, "A theory of fatigue under multiaxial strain conditions," Proceedings of the Institution of Mechanical Engineers, vol. 187, pp. 745-755, 1973.

Authors

Markus EICHHORN
Vienna University of Technology
Institute for Energy Systems and Thermodynamics
Getreidemarkt 9/302, A-1060 Vienna, AUSTRIA
Phone: +43-1-58801-302357,
E-mail: markus.eichhorn@tuwien.ac.at

Lukas WALDNER
Vienna University of Technology
Institute for Energy Systems and Thermodynamics
Getreidemarkt 9/302, A-1060 Vienna, AUSTRIA

Christian BAUER
Vienna University of Technology
Institute for Energy Systems and Thermodynamics
Getreidemarkt 9/302, A-1060 Vienna, AUSTRIA
Phone: +43-1-58801-302401,
E-mail: cbauer@mail.tuwien.ac.at

Markus Eichhorn graduated in Mechanical Engineering at the TU Wien in 2013. Currently he is working as project assistant at the Institute for Energy Systems and Thermodynamics at the TU Wien.

Lukas Waldner graduated in Mechanical Engineering at the TU Wien in 2015. He worked as project assistant at the Institute for Energy Systems and Thermodynamics at the TU Wien until 2016.

Christian Bauer Christian Bauer graduated 1991 in Mechanical Engineering from the University of Stuttgart. In 2000 he finished his PhD in the field of Hydraulic Fluid Flow Machinery. After several years in the industry Mr. Bauer changed to the TU Wien in 2008. Since 2016 he is the head of the Institute for Energy Systems and Thermodynamics.

9.2 Paper 5

In the fifth paper (see Tab. 9.2) the expected load spectra of the two prototype Francis turbines in the critical low-load operating points are investigated. Therefore, the unsteady CFD simulations using the SAS turbulence model are applied as well to the high head machine to evaluate the differences to the previously used standard k - ω SST model. The pressure fluctuations in the draft tube diffuser of both Francis turbines, induced by appearing draft tube vortex ropes, are compared to measurements on the according prototype machines to obtain the influence and accuracy of the turbulence models. Further, the results of the transient FEM simulations are discussed related to the amplitudes and the power spectral densities of the computed and measured stresses at the strain gauge positions. The influence on the fatigue of both Francis runners is obtained by the rainflow cycle counting algorithm. Therefore, the uniaxial stress signals at the strain gauge positions and the multiaxial stress states at the highest excited notches are used. For a more convincing comparison between the long measurement signals and the relative short simulation duration, a stress extrapolation approach is applied.

Table 9.2: Notes on Paper 5.

Title	Expected Load Spectra of Prototype Francis Turbines in Low-Load Operation Using Numerical Simulations and Site Measurements
Authors	M. Eichhorn, A. Taruffi, C. Bauer
Conference	7th IAHR Meeting of the Working Group on Cavitation and Dynamic Problems (IAHRWG 2017)
Location	Porto, Portugal
Date	February 1-3, 2017
Published in	Journal of Physics: Conference Series, Volume 813/1: 012052, 2017

Expected load spectra of prototype Francis turbines in low-load operation using numerical simulations and site measurements

M Eichhorn¹, A Taruffi² and C Bauer¹

¹ TU Wien, Institute for Energy Systems and Thermodynamics, Getreidemarkt 9/302, 1060 Vienna, Austria

² Andritz Hydro, Rue des Deux Gares 6, 1800 Vevey, Switzerland

E-mail: markus.eichhorn@tuwien.ac.at

Abstract.

The operators of hydropower plants are forced to extend the existing operating ranges of their hydraulic machines to remain competitive on the energy market due to the rising amount of wind and solar power. Faster response times and a higher flexibility towards part- and low-load conditions enable a better electric grid control and assure therefore an economic operation of the power plant. The occurring disadvantage is a higher dynamic excitation of affected machine components, especially Francis turbine runners, due to pressure pulsations induced by unsteady flow phenomena (e.g. draft tube vortex ropes). Therefore, fatigue analysis becomes more important even in the design phase of the hydraulic machines to evaluate the static and dynamic load in different operating conditions and to reduce maintenance costs. An approach including a one-way coupled fluid-structure interaction has been already developed using unsteady CFD simulations and transient FEM computations. This is now applied on two Francis turbines with different specific speeds and power ranges, to obtain the load spectra of both machines. The results are compared to strain gauge measurements on the according Francis turbines to validate the overall procedure.

1. Introduction

As solar and wind power generation is growing steadily, their volatility rises the necessity of large and also flexible energy storage. Even other systems like compressed-air or battery solutions will become more advanced in the future [1], pumped hydro energy storage will remain the most competitive technology in the next years [2]. The pending challenge for manufacturer and operators of pumped storage power plants (PSP) will be an increase of operating flexibility towards off-design operation with a simultaneously prevention of lifetime reduction. Due to unsteady flow phenomena in part-load, low-load and overload conditions of especially Francis and pump turbines, higher pressure fluctuations may appear inducing an increasing dynamic excitation of affected structures like the runner [3]. Therefore, the prediction of critical operating conditions and the fatigue analysis in the design phase of Francis and pump turbines is becoming more significant. The increasing capabilities of numerical computations enable their application for such investigations. To evaluate their accuracy as well, unsteady CFD and transient FEM simulations are performed on two prototype Francis turbines in low-load operating conditions: a high head runner with a specific speed of $n_q \approx 24 \text{ min}^{-1}$ (PSP-HH) and a medium head

runner with a specific speed of $n_q \approx 52 \text{ min}^{-1}$ (PSP-MH). The results are used to compute the expected load spectra with the rainflow counting algorithm. Prototype site measurements should help to validate the whole approach, which has been partially published already (see [4] and [5]). Therefore, several single strain gauges (SG) have been applied on one runner blade at the pressure side (PS) and suction side (SS) close to the trailing edge (see figure 1). The position and orientation of the sensors have been recorded for the comparison with the numerical results.

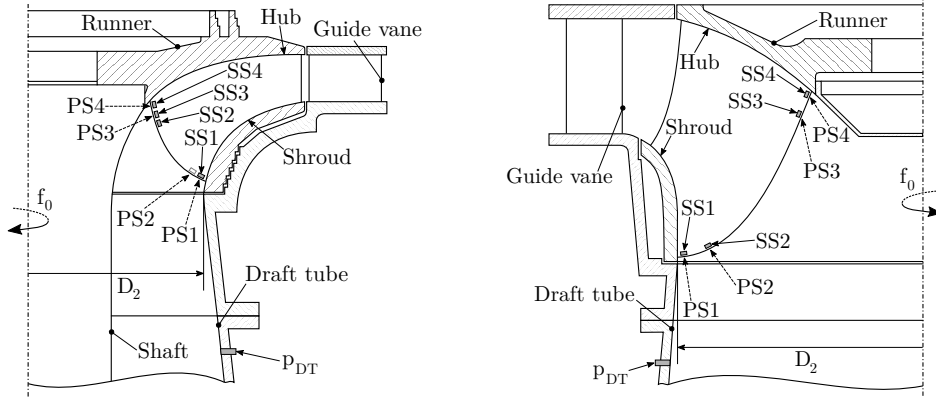


Figure 1: Schematic contour of the meridional section including the positions of the strain gauges on the runner blades and the pressure measurements in the draft tube for PSP-HH (left) and PSP-MH (right).

Further, pressure measurements have been done in the draft tube cone (p_{DT}) of both machines to validate the appearing pressure oscillations in the CFD simulations. One main difference between the two investigated Francis turbines, beside the specific speed, is the shaft going through the draft tube cone at PSP-HH, which has also a major impact on the flow behavior. The measured stress amplitudes σ_a , normalized by the yield strength of the runner material σ_y are displayed in figure 2.

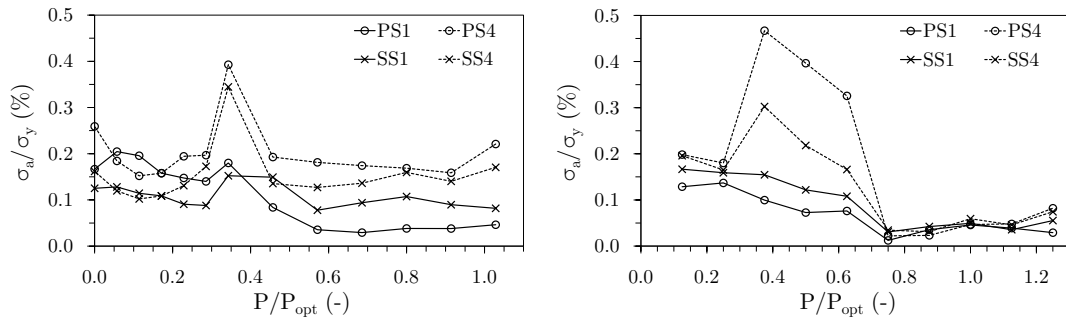


Figure 2: Measured dynamic stress amplitudes at different strain gauge positions and operating points for PSP-HH (left) and PSP-MH (right).

At PSP-HH a relative high stress amplitude level can be observed in all operating points due to the influence of the rotor-stator interaction (RSI). At low-load operation, with a normalized power of $P/P_{opt} \approx 0.34$, the stress amplitudes are obviously increasing with the highest values appearing close to the hub of the runner (SG PS4 and SS4). A similar behavior can be observed for the medium head Francis runner. Due to the higher gap size between the wicket gate and the runner and therefore a lower impact of the RSI, the dynamic stresses are lower in high-

and full-load operation. In part- and low-load operation, the stress amplitudes are dramatically increasing, especially at the runner hub region (SG PS4 and SS4), with the highest values appearing also at $P/P_{opt} \approx 0.37$. Hence, these two low-load operating points are of special interest and will be therefore used for the numerical simulations described in the following sections.

2. Unsteady CFD simulations

As the dynamic excitation of the Francis runners is mainly depending on the pressure oscillation inside the machine, unsteady CFD simulations are performed with OpenFOAM, to investigate the flow phenomena in the critical operating points. Therefore, the relevant components of the two hydraulic machines are considered, including the spiral casing, the stay vanes, the guide vanes the runner and the draft tube. The different domains are discretized separately with hexahedral meshes using ANSYS ICEM CFD and ANSYS Turbogrid (see figure 3). The mesh of PSP-HH consists of about 6 million cells and the one for PSP-MH of about 9 million cells. To accurately predict the pressure fluctuations inside the runner, the discretization is refined in this domain with about 2.6 million cells for PSP-HH and about 3.3 million cells for PSP-MH. The guide vane opening position is adjusted according to the measurements. The unsteady CFD simulations are performed for several runner rotations using a transient rotor-stator analysis. A frozen-rotor simulation is used as initial solution to improve and speed-up the convergence. The discharge is defined as boundary condition at the spiral inlet according to the measurements. At the draft tube outlet the static pressure is set to an averaged value. The time step size is fixed to an according runner rotation of 0.36° for PSP-HH and 0.6° for PSP-MH resulting in a maximum Courant number of $Co_{max} = 25$. The CFD simulations are performed using the two-equation turbulence model $k-\omega$ SST as well as the Scale Adaptive Simulation (SAS) approach, to evaluate the influence of the turbulence modeling.

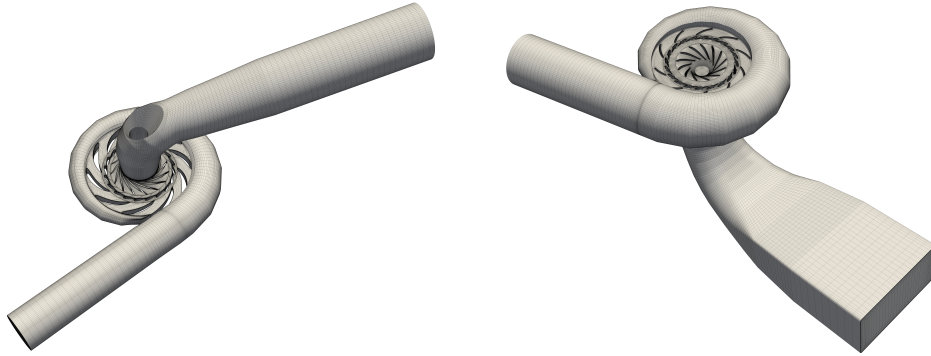


Figure 3: Discretization of the hydraulic components for the CFD simulations of PSP-HH (left) and PSP-MH (right).

In figure 4 the spectral power density of the measured and computed pressure signals in the draft tube cone p_{DT} at low-load operation for PSP-HH ($P/P_{opt} \approx 0.34$) and PSP-MH ($P/P_{opt} \approx 0.37$) are displayed. The pressure fluctuations Δp are normalized by the energy corresponding to the rotational speed $p_E = \rho u_2^2/2$ with the circumferential velocity at the runner outlet $u_2 = D_2 f_0 \pi$ and the rotational frequency of the runner f_0 , as proposed in [6]. For a more convincing comparison between the long measurement duration (120 s) and the short CFD simulations, the measured pressure signal is split into several windows according to the computations. Afterward, the mean values (EXP mean) and the standard deviations (EXP range) are evaluated to express the range of the measurements. The measured results of PSP-HH reveal higher dynamic pressure fluctuations in the normalized frequency range of $0 \leq f/f_0 \leq 5$.

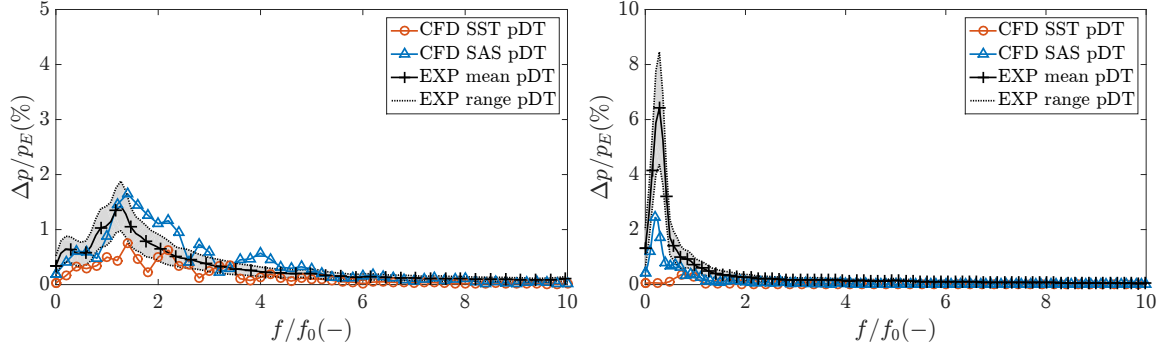


Figure 4: Comparison of the spectral power density between the measured and computed pressure fluctuations in the draft tube cone p_{DT} at low-load conditions for PSP-HH (left) and PSP-MH (right).

The CFD simulations of both turbulence models show also higher values in this range with a slightly underestimation of the SST model. At PSP-MH a more distinct peak is appearing at $f / f_0 \approx 0.8$. The k- ω SST model reveals only a small peak at the rotational frequency $f / f_0 = 1$. The SAS model on the other hand shows more accurate results even the amplitude is underestimated. In figure 5 the numerically computed pressure amplitudes with the SAS model at the runner surfaces of both machines are shown together with appearing draft tube vortices, which are displayed by iso-pressure surfaces.

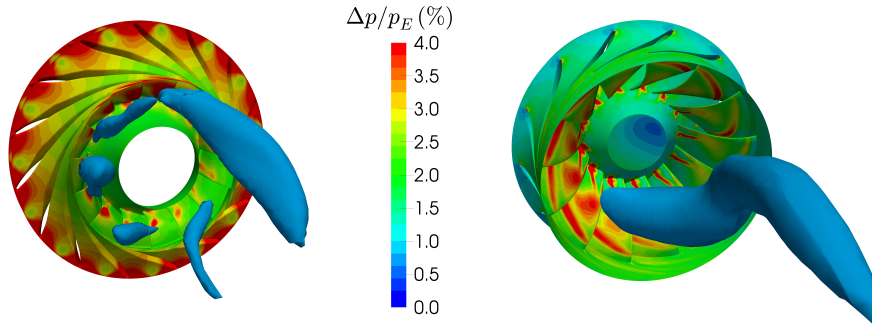


Figure 5: Pressure amplitudes on the Francis runner surfaces computed with the SAS turbulence model and appearing draft tube vortices at PSP-HH (left) and PSP-MH (right).

At PSP-HH high pressure fluctuations are appearing at the runner inlet due to the RSI. At the outlet the rotating draft tube vortices are inducing pressure oscillations as well, especially in the hub region of the runner. One characteristic of PSP-HH is the shaft going through the draft tube. Hence, multiple smaller and bigger vortices are appearing and collapsing again along the time, inducing a broadband excitation as visible in figure 4. At PSP-MH one bigger draft tube vortex rope is appearing and rotating more stable in the runner direction. Therefore, the highest pressure amplitudes are appearing at the runner outlet. Only small excitations are visible at the leading edges due to a less impact of the RSI at PSP-MH.

3. Transient FEM simulations

The results of the unsteady CFD simulations are used to evaluate the structural behavior and the dynamic stresses of the Francis runners by transient FEM simulations with the open-source tool Code_Aster. The model and the discretization of the investigated turbines are displayed

in figure 6. The tetrahedral mesh of each runner geometry consists of about 0.5 million nodes. This relative small size is achieved by refining only one runner blade in the critical zones, which is also used for the stress evaluation. A grid convergence study has been performed as well to assure reliable results.

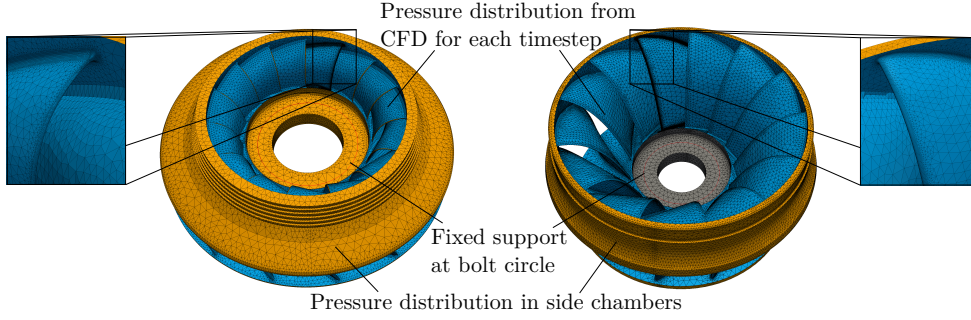


Figure 6: Discretization and boundary conditions for the transient FEM simulations for PSP-HH (left) and PSP-MH (right).

The time-dependent pressure distributions from the CFD computations are applied to the surfaces of the blade channels for each time step. The pressure distributions in the runner side chambers are assumed to be static and are computed by an analytical model as described in [7]. The Francis turbines are fixed at the bolt circles and the circumferential and gravitational forces are considered as well. The transient FEM simulations are performed for several runner rotations with an according time step size of 3.6° for PSP-HH and 3.0° for PSP-MH. The damping of the structure is considered by an equivalent Rayleigh damping as described in [5]. Monitoring points at the refined runner blade are used to compare the stresses with the measured data at the strain gauge positions. The overall dynamic stress amplitudes of the FEM simulations and the measurements at the strain gauge positions for PSP-HH and PSP-MH at the investigated low-load operation points are displayed in figure 7.

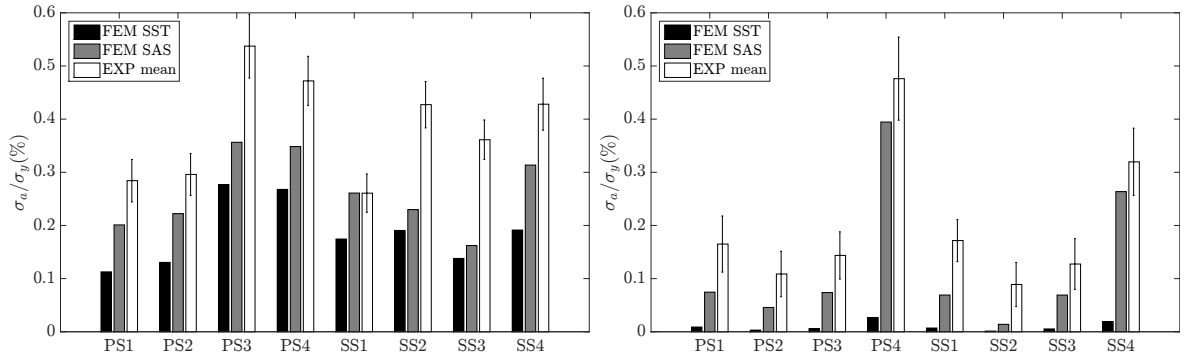


Figure 7: Comparison of the dynamic stress amplitudes calculated by the RMS values between the measured data and the transient FEM simulations at low-load operation for PSP-HH (left) and PSP-MH (right).

The measured stress signal, with a length of 120 s, is separated in smaller windows according to the FEM simulations to calculate the mean values (EXP mean) and the measurement range. To determine the influence of the turbulence model on the structural response, the pressure distributions of the SST and the SAS model are used. The results show an accurate agreement with the measurement tendencies, even the computed values underestimate the measured peaks.

Due to the higher accuracy of the SAS model regarding the pressure fluctuations in the draft tube, the overall stress amplitudes are predicted more precise as well, with the highest values appearing close to the hub of the runner. According to the numerical flow simulations, the results for PSP-MH reveal much bigger differences between the turbulence models, with a total underestimation of the stress amplitudes by the SST model. The SAS model shows the highest amplitudes also close to the hub at SG PS4 and SS4. The spectral power densities of the measured and simulated stress signals at the strain gauge PS4 for PSP-HH reveal higher stress amplitudes in the low frequency range due to the pressure fluctuations in the draft tube (see figure 8). At the first and second harmonic of the blade passing frequency ($f/f_0 = 20$ and $f/f_0 = 40$) higher stress amplitudes are visible, even the SAS turbulence model overestimates the measured values. For PSP-MH a high peak is visible at the normalized frequency $f/f_0 \approx 0.8$ induced by the appearing vortex rope according to figure 4. In contrast to the SST model, the curve of the SAS model is in a good agreement with the measurements.

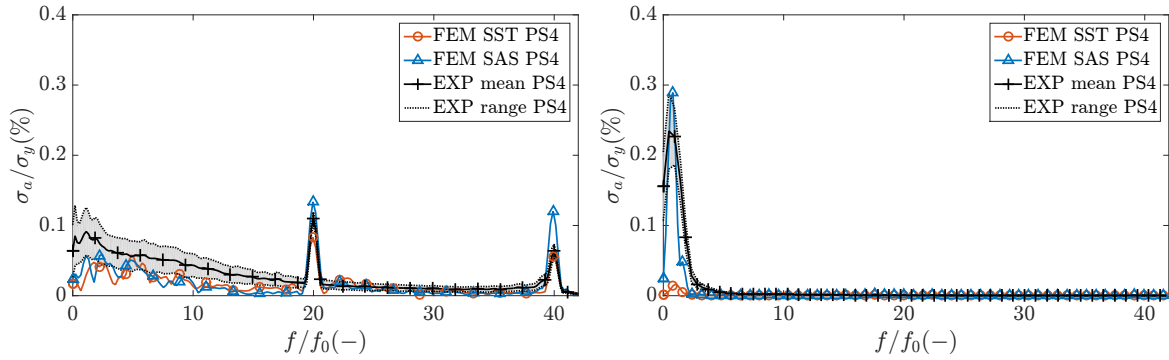


Figure 8: Comparison of the spectral power density between the measurements and the computed stresses at low-load operation for PSP-HH (left) and PSP-MH (right).

4. Expected load spectra

The results of the transient FEM simulations performed with the SAS turbulence model are used for a rainflow counting analysis at the strain gauge positions and at the critical locations of both Francis runners. In figure 9 the dynamic stress amplitudes, calculated by the standard deviation of the time signals, in low-load operation at the refined runner blades are displayed.

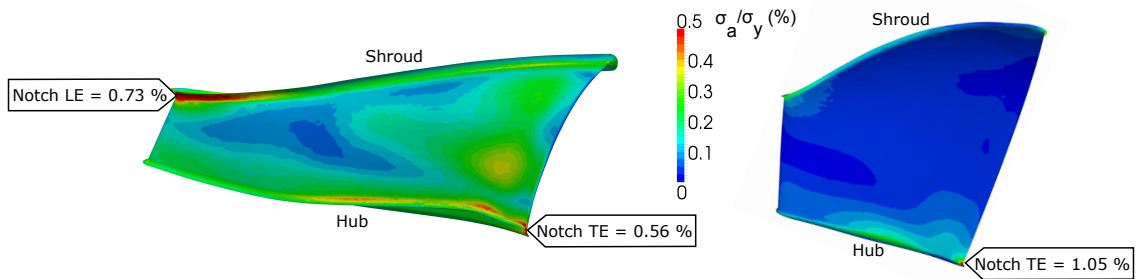


Figure 9: Stress amplitudes at the Francis runner blades at low-load operation for PSP-HH (left) and PSP-MH (right) computed with the SAS turbulence model.

At PSP-HH the highest values are appearing in the notch at the leading edge (LE) of the runner due to the rotor-stator interaction but also at the trailing edge (TE) due to the pressure

fluctuations in the draft tube. For PSP-MH the dynamic stresses at the leading edge are lower due to the less impact of the RSI. The critical location with the maximum excitation, induced by the draft tube vortex rope, is appearing at the trailing edge close to the hub of the runner. To determine the impact of the dynamic excitation of the high and medium head runner in low-load operation a rainflow counting analysis is performed. Therefore, the measured and computed uni-axial stress signals at the strain gauge positions and the multi-axial stresses at the critical runner locations, obtained by the FEM simulations, are used. To evaluate the measurement range the signals are again divided into several windows according to the computations. To gain a more convincing comparison between the measurements and the simulations a stress extrapolation, based on the extreme value theory described in [8], is performed. This approach has been already applied for a fatigue analysis of a Francis runner at speed-no-load operation (see [9]). For the evaluation of the damage by the three-dimensional stress state in the notches, the algorithm of Brown and Miller [10] is used, considering the influence of the shear and normal strains. The obtained load spectra of both Francis turbines are displayed in figure 10 including the corresponding stress-cycle (S-N) curve of the runner material for a 99 % survival probability. The measured and computed stress signals are extrapolated up to a time length of 1000 s. The rainflow counting analysis reveals an accurate agreement between the results of the measurements and the FEM simulations at the strain gauge positions for both turbines. The evaluation of the multi-axial stresses at the critical locations shows slightly higher amplitudes compared to the strain gauges as expected. The rainflow curves of both Francis turbines are below the fatigue limit of the runner material, even considering the measurement range.

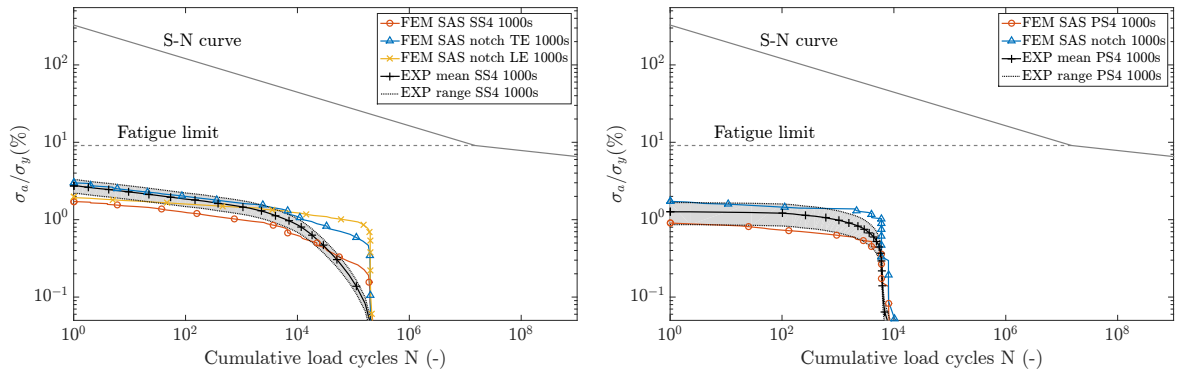


Figure 10: Load spectra of the measured and computed stresses with the SAS turbulence model at low-load operation for PSP-HH (left) and PSP-MH (right).

5. Conclusion

The strain gauge measurements on a high head and a medium head prototype Francis runner revealed increased dynamic excitations in low-load operating conditions at about one third of the rated output power. Additional pressure measurements in the draft tube cone showed higher amplitudes in the lower frequency range for both machines at the same operation points. To investigate the reason for the high stress peaks and to obtain the load spectra of the turbines, numerical computations consisting of unsteady CFD and FEM simulations were performed. Therefore, two different turbulence models - the $k-\omega$ SST and the Scale Adaptive Simulation (SAS) model - were used. The flow simulations revealed increased pressure fluctuations at the leading edge of the high head runner due to the major impact of the rotor-stator interaction. At the turbine outlet higher pressure amplitudes occurred as well for both

hydraulic machines due to the influence of appearing draft tube vortex ropes. Compared to the pressure measurements, the SAS turbulence model seems to better predict the impact of the vortices on the pressure oscillations. The transient FEM simulations in the low-load operating points revealed an accurate determination of the overall stress amplitudes. The application of the time dependent pressure distributions computed by the SAS turbulence model lead to more precise results, especially for the medium head turbine. The transient FEM simulations exposed different locations with higher dynamic excitations for both turbines: At the leading edge for the high head runner induced by the rotor-stator interaction and at the trailing edge due to the draft tube vortex ropes for both machines. The measured and computed stresses at the strain gauge positions and at the critical notches were further used for a rainflow counting analysis together with a stress extrapolation approach. The results revealed an appropriate agreement between the simulations and the site measurements with stress-cycle curves below the fatigue limit of the runner material. For a valuable lifetime prediction of the Francis runners, additional investigations should be performed considering geometrical deviations, numerical simplifications and further uncertainties.

Acknowledgments

The K-Project GSG-GreenStorageGrid is funded in the framework of COMET - Competence Centers for Excellent Technologies by the Federal Ministry of Transport, Innovation and Technology, the Federal Ministry of Science, Research and Economy, the Vienna Business Agency, the Federal Province of Lower Austria and by the Federal Province of Upper Austria. The program line COMET is administered by the Austrian Research Promotion Agency (FFG). The authors would like to thank the project partners Andritz Hydro, Verbund Hydro Power, ZT Hirtenlehner, TIWAG Tiroler Wasserkraft AG and Vorarlberger Illwerke AG for their contribution in the course of the sub-project PSP-LowLoad. Special thanks goes to Andritz Hydro for their support regarding the application of Code_Aster. The computational results presented have been achieved in part using the Vienna Scientific Cluster (VSC).

References

- [1] Teller, O et al 2013 *European Energy Storage Technology Development Roadmap towards 2030*. (Brussels: EASE/EERA Core Working Group)
- [2] Guittet M, Capezzali M, Gaudard L, Romerio F, Vuille F and Avellan F 2016 Study of the drivers and asset management of pumped-storage power plants historical and geographical perspective. *Energy* **111** 560–579. ISSN 03605442
- [3] Magnoli M V 2014 *Numerical simulation of pressure oscillations in large Francis turbines at partial and full load operating conditions and their effects on the runner structural behaviour and fatigue life*. Ph.D. thesis Technische Universität München
- [4] Eichhorn M, Doujak E and Waldner L 2016 Investigation of the fluid-structure interaction of a high head Francis turbine using OpenFOAM and Code_Aster. *28th IAHR symposium on Hydraulic Machinery and Systems*
- [5] Eichhorn M and Doujak E 2016 Impact of different operating conditions on the dynamic excitation of a high head francis turbine. *Proceedings of the ASME 2016 International Mechanical Engineering Congress & Exposition*
- [6] Dörfler P, Sick M and Coutu A 2013 *Flow-Induced Pulsation and Vibration in Hydroelectric Machinery*. (London, New York: Springer)
- [7] Maly A, Eichhorn M and Bauer C 2016 Experimental investigation of transient pressure effects in the side chambers of a reversible pump turbine model. *Proceedings of the 19th International Seminar on Hydropower Plants*
- [8] Johannesson P 2006 Extrapolation of load histories and spectra. *Fatigue & Fracture of Engineering Materials Structures* **29** 209–217
- [9] Morissette J F, Chamberland-Lauzon J, Nennemann B, Monette C, Giroux A M, Coutu A and Nicolle J 2016 Stress predictions in a francis turbine at no-load operating regime. *28th IAHR Symposium on Hydraulic Machinery and Systems*
- [10] Brown M W and Miller K J 1973 A theory of fatigue under multiaxial strain conditions. *Proceedings of the Institution of Mechanical Engineers* **187** 745–755

9.3 Impact on the Structural Damage

The results of the rainflow counting analysis described previously are used to assess the impact on the structural damage and the expected lifetime of the Francis runners in the critical low-load operation points. Therefore, the fatigue damage accumulation by Palmgren and Miner (see Chap. 5) is applied to the resulting load spectra of the numerical simulations and the strain gauge measurements.

In the original form of the Miner rule the influence of stress amplitudes below the fatigue limit σ_l is neglected, which can be described by a slope $s_o^* = \infty$ of the S-N curve (see Fig. 9.1). This assumption is usually valid for most steel and iron casting materials. For aluminum and also for steel in corrosive media, as it is the case for Francis turbines in water, a further decrease of the S-N curve below the fatigue limit appears. According to fatigue tests performed at the Fraunhofer LBF Institute for Structural Durability and System Reliability considering the runner material of the Francis turbines in water (see Gaßner et al. [33]), a slope s^* is observed below σ_l . However, the assumption of the original Miner rule can yield large discrepancies between calculated and experimentally observed lifetimes as investigations by Schütz and Zenner [85] revealed. They proposed that stress amplitudes above the fatigue limit induce defects, which further influence the damage impact of smaller dynamic stress values. To avoid unreliable fatigue assessment different modifications of the original Miner rule have been suggested as described by Köhler et al. [49]. The first approach is the elementary Miner rule, which assumes that no certain fatigue limit exists and the slope in the endurance range is $s_e^* = s$. A second procedure is the modified Miner rule proposed by Haibach [39]. Thereby, the S-N curve is extended in the endurance range with a slope $s_m^* = 2s - 1$. Both approaches are recommended in the FKM guideline (see Hänel et al. [42]) for fatigue assessment. Hence, the modified and the elementary Miner rule as well as the experimentally observed S-N curve are applied to the measured and computed load spectra of the medium and the high head Francis turbine to assess the impact on the total fatigue damage C and the expected lifetime L .

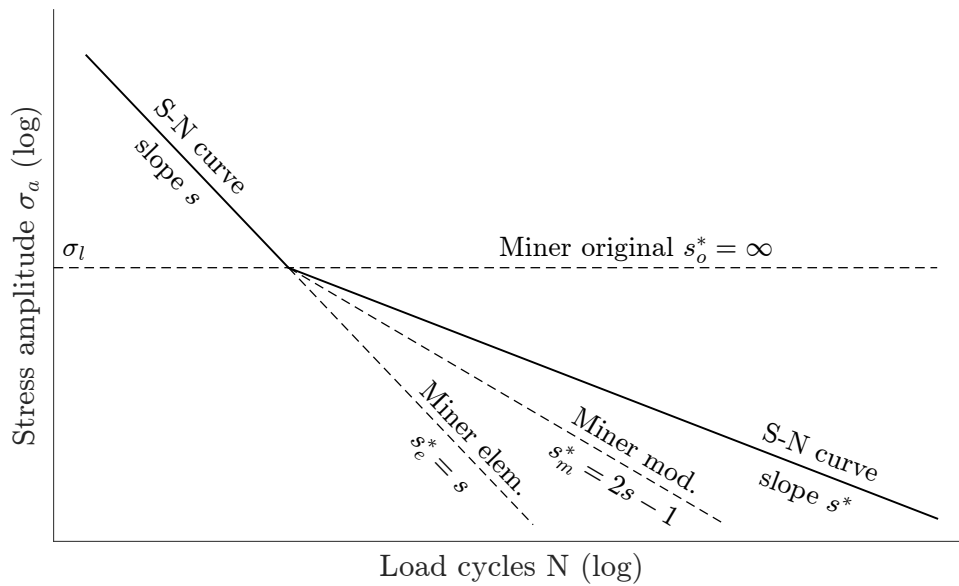


Figure 9.1: S-N curves for different damage models in the fatigue endurance range.

For the simulations the load spectra obtained with the CFD results of the SAS turbulence model are used. To assess the uncertainties of the strain gauge measurements the standard deviations of the obtained stresses and the measuring error discussed in Appendix A.1 are considered. For the results of the FSI simulations the numerical uncertainties described in Appendix A.2 are used. Due to the application of single strain gauges at the prototype site measurements the multiaxial stress state in the notches could not be obtained directly. The fatigue damage is therefore approximated using the load spectra of the closest strain gauge (SS4 for the high head runner and PS4 for the medium head runner), which is multiplied with the stress concentration factor K_s obtained from the FEM simulations:

$$K_s = \frac{\sigma_{a,max,notch}}{\sigma_{a,max,SG}}. \quad (9.1)$$

Thereby, $\sigma_{a,max,notch}$ is the maximum appearing stress amplitude in the notch and $\sigma_{a,max,SG}$ is the maximum stress amplitude at the strain gauge. The respective stress concentration factor for the high head runner is $K_s = 1.70$ and for the medium head runner $K_s = 1.83$. The resulting total fatigue damage factors C for both Francis machines at the strain gauges and at the critical notches at the trailing edge are displayed in Fig. 9.2. The results reveal low fatigue damages of the measured and computed load spectra for the according extrapolation time of 1000 s and a good agreement between the values at the respective strain gauges and in the notch.

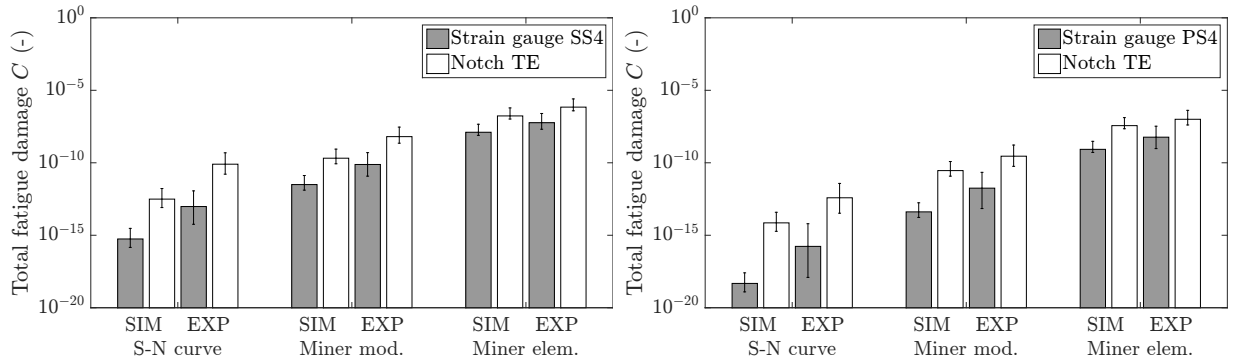


Figure 9.2: Total fatigue damage factors C for the high head runner (left) and the medium head runner (right) for different S-N curves in the endurance range.

The typical failure criteria for components considering the cumulative damage factor is $C = 1$. The mechanical fracture caused by oscillating stresses appears in fatigue tests usually at $C \neq 1$ and in most cases at $C < 1$. As the fatigue damage accumulation is subject to a distinct scattering Haibach [39] and the FKM guideline [42] recommend a reduced factor of $C_r = 0.3$. Hence, the durability of the hydraulic turbines are obtained at first for $C = 1$ and the influence of a reduced damage factor is subsequently discussed below. The expected lifetimes L of the medium and the high head Francis runner at the strain gauges and at the critical notches at the trailing edge are displayed in Fig. 9.3. The results are mainly influenced by the applied S-N curve in the endurance range as the load spectra of both machines in low-load operation are below the fatigue limit σ_l . The minimum lifetimes are therefore obtained by the elementary Miner rule as expected due to the same slope of the S-N curve in the endurance range as in the HCF area. Nevertheless, the comparison of

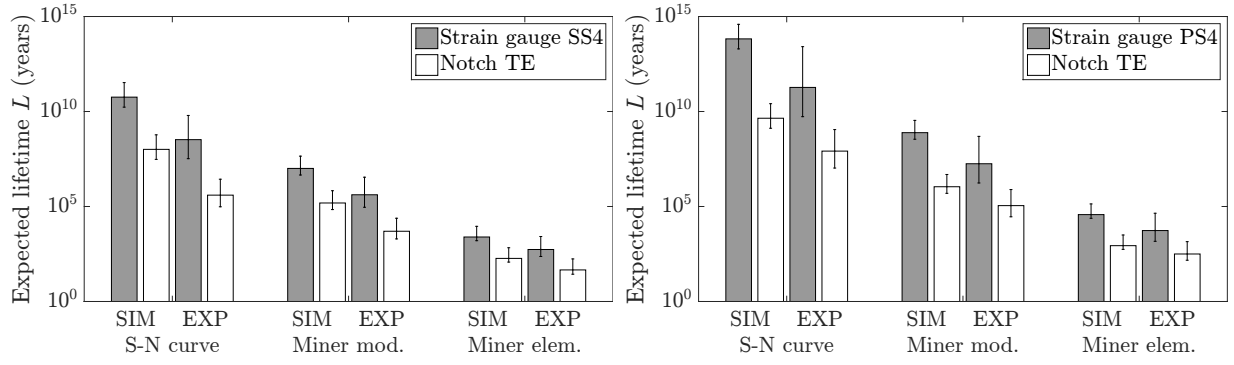


Figure 9.3: Expected lifetimes L for a total fatigue damage factor $C = 1$ for the high head runner (left) and the medium head runner (right) for different S-N curves in the endurance range.

the measured and the computed values for the different fatigue approaches reveals a good correlation.

The maximum load cycles \bar{N} for reduced damage factors $C_r < 1$ and further the lifetime L can be calculated according to Haibach [39] by $\bar{N} = C_r \cdot N_{(C=1)}$. In Tab. 9.3 the expected lifetimes for both Francis turbines using the elementary Miner rule and damage factors $C = 1$ and $C_r = 0.3$ are displayed. The minimum estimated lifetimes for the high head runner are at least 8 years obtained from the measurements and 27 years computed by the simulations. For the medium head runner the measured durability is approximately 44 years and more than 166 years according to the computations. It is important to mention that the expected lifetimes correspond to a continuous operation of the machines in the critical low-load point. In fact, the related operating hours per year are far less. For a reliable fatigue assessment realistic load assumptions have to be considered for the according steady but also transient events with the respective static and dynamic stresses. The application of the linear damage accumulation is only an estimation if failure of components occurs or not at a certain amount of time. To obtain more detailed information about the damage extent more advanced approaches like crack growth models have to be applied as discussed by Liu et al. [58], but this would exceed the scope of this thesis.

Table 9.3: Expected lifetimes L of the medium and the high head Francis turbine in low-load operation using the load spectra at the critical notch and the elementary Miner rule.

		PSP-HH			PSP-MH		
		Expected lifetime L (years)			Expected lifetime L (years)		
		L_{\min}	L_{avg}	L_{\max}	L_{\min}	L_{avg}	L_{\max}
$C = 1$	SIM	118.65	185.45	303.84	554.99	867.44	1421.16
	EXP	27.31	45.87	82.20	148.58	316.32	779.07
$C_r = 0.3$	SIM	35.60	55.64	91.15	166.50	260.23	426.35
	EXP	8.19	13.76	24.66	44.57	94.90	233.72

Chapter 10

Conclusion and Outlook

10.1 Summary of the Thesis

In the scope of this thesis a numerical approach to evaluate the impact of different operating conditions on the mechanical loads and the fatigue of prototype Francis turbines is proposed and assessed on a medium and a high head machine. Therefore, fluid-structure interactions are performed with the open-source tools OpenFOAM for the CFD simulations and Code_Aster for the FEM computations. Strain gauge measurements on the according hydraulic turbines are used to validate the numerical approach. The measured stresses reveal the highest mean values at full output power for both machines. For the high head runner significant dynamic excitations are appearing along all load conditions in the range of the blade passing frequency induced by the rotor-stator interaction. Further, the highest dynamic stress amplitudes are observed in low-load operation for both Francis turbines.

To obtain the fluid flow in different operating conditions unsteady CFD simulations are performed as the static and dynamic pressure distribution is of main importance for the mechanical response. A grid convergence study is performed for the high head runner to assess the numerical error induced by the spatial discretization and to ensure reasonable computational costs at sufficient accuracy. The boundary layer close to the solid walls is approximated using standard wall functions implemented in OpenFOAM with respect to an appropriate mesh density evaluated by the dimensionless distance y^+ . Second order interpolation schemes for the temporal and spatial discretization approaches are further applied to enable accurate numerical results. To obtain the impact of the inlet boundary condition on the global parameters and the mechanical loads, two physical models are used for the high head runner: A full model including the spiral casing, the stay vanes, the wicket gate, the runner and the draft tube and a reduced model with a cyclic inlet boundary condition without the spiral casing. The investigations reveal only marginal differences between both models regarding the head, efficiency, runner torque and also the static stresses. For the CFD simulations of the medium head runner the full model including the spiral casing is used. The numerical flow computations of both machines are validated by a comparison of the global parameters with the measured values on the according machines revealing a sufficient agreement.

As turbulence modeling can have a major impact on the fluid flow behavior the standard

two-equation RANS turbulence model $k-\omega$ SST as well as the hybrid URANS-LES model SAS is used for the unsteady CFD simulations of both Francis turbines. The comparison with pressure measurements in the draft tube cone and with the measured stress amplitudes reveals more accurate results for the SAS turbulence model in low-load operation. Especially for the medium head Francis turbine the difference between both models is significant as the $k-\omega$ SST model underestimates the appearing draft tube vortex rope. However, deviations from the measured pressure fluctuations are observed even using the SAS turbulence model. The reason could be based on the applied single-phase fluid neglecting any influence of cavitation. In the case of an appearing two-phase flow at low Thoma numbers the application of multiphase models may deliver much better results for the pressure fluctuations. Another influence could originate from the mesh density in the draft tube domain. A mesh convergence study with special focus on the pressure fluctuations could reveal further details. However, this requires high computational costs as unsteady CFD simulations with large mesh sizes have to be performed.

The averaged pressure distributions computed with the flow simulations are used to assess the static stresses on both Francis runners in different operating conditions ranging from the full-load to the low-load regime. Therefore, FEM simulations using a reduced cyclic sector model consisting of a single turbine blade are performed. The results are compared to the strain gauge measurements applied on the prototype Francis machines. For the medium head runner, the computed and measured stresses show a good agreement with only noticeable deviations between both used turbulence models at maximum power output. For the high head runner, more significant differences between the numerical results and the measurements appear. To obtain the error based on the spatial discretization of the FEM model, a grid convergence study similar to the CFD simulations is performed for the high head turbine. The results reveal reasonable values and a good agreement for the comparison with the measured stresses in the condenser operating mode, where the runner is only running in air. Further investigations considering the influence of boundary conditions for the static FEM model could help to obtain the reason for the deviations of the mean stresses at the high head Francis turbine. Nevertheless, the observed mean and equivalent von Mises stresses for both runners are much lower than the yield strength of the used material.

The influence of dynamic strains and stresses induced by the fluid flow causes varying excitations on the turbine, which can lead to fatigue cracks and expensive failure events in some cases. For high head Francis machines the rotor-stator interaction between the guide vanes and the runner blades is mainly responsible for alternating load conditions, which is proved by the site measurements. Although the flow behavior in the best efficiency point corresponds to the turbine geometry the structural loads may be significant, especially in cases of appearing resonance. Therefore, the natural mode shapes and the according eigenfrequencies of the high head runner are obtained using a modal analysis. As the surrounding water volume may affect the structural behavior, the influence of the added-mass effect is assessed by acoustic elements in the FEM model. The results reveal a major impact on the observed eigenfrequencies for higher order modes but not in the range of the blade passing frequency. Hence, appearing resonance is not expected during operation. To investigate the impact of the RSI, harmonic response simulations are performed in different operating points using the Fourier transformed pressure fluctuations at the blade passing frequency. The comparison with the measured stress amplitudes at the strain gauge positions show a

good agreement with the numerical results. The highest excitations appear at the turbine inlet as expected but the dynamic stresses are in a non-critical range.

In off-design operation inappropriate flow phenomena appear like draft tube vortex ropes or interblade vortices, which induce harmonic but also stochastic pressure fluctuations. To evaluate the impact of the critical low-load conditions measured at the medium and the high head Francis turbine, transient FEM simulations are performed using the time dependent pressure distribution obtained from the CFD computations. As the structural damping may have a significant impact on the mechanical response the approach proposed by Rayleigh is used. The related damping coefficients are calculated considering the mass participation of the low order modes. The comparison of the dynamic stress amplitudes between the numerical investigations and the strain gauge measurements reveals a good correlation. Regarding the impact of the turbulence models on the runner structure, the same behavior as for the pressure fluctuations in the CFD simulations can be observed for both hydraulic machines. Hence, the correct computation of the time dependent fluid flow is of major importance and should be evaluated accurately for future investigations.

The applicability of the numerical approach for a fatigue assessment is validated by the usage of the rainflow cycle counting algorithm to the measured and computed stress signals. Therefore, the uniaxial stresses at the strain gauge positions as well as the multiaxial stress state at the critical notches are considered. The impact on the structural impairment is further assessed by the fatigue damage accumulation of Palmgren and Miner using different models for the S-N curves in the endurance range. The expected lifetimes reveal a good agreement between the numerical investigations and the prototype site measurements.

10.2 Future Work

For a reliable assessment of the lifetime of Francis turbine runners, the appearing static and dynamic stresses at each steady but also at transient load conditions like start-stop processes or load rejection must be considered with the according operating duration. The initiation and propagation of fatigue cracks is not only influenced by high cycle events with stress amplitudes below the yield strength but also by low cycle excitations in the elasto-plastic regime during transient events. To avoid major damages on the hydraulic machines resulting in expensive repairs and downtime but also to better estimate necessary maintenance intervals, realistic load assumptions together with accurate prediction methods are needed. Although the numerical approach proposed in this thesis could be used not only for steady but also for transient operating conditions, the computational effort would still exceed the acceptable range. Prototype site measurements require also a large demand but can be used to obtain the static and dynamic stresses during start-stop operation or load rejection. Hence, a combined approach consisting of numerical fluid-structure simulations in steady load conditions and site measurements in transient events would be the best opportunity for a detailed fatigue assessment of Francis turbines.

For the application of the proposed numerical method in industrial design processes, further investigations should be done considering the added mass effect of the water volume around the runner for the transient FEM simulations. Additionally, more detailed CFD computations regarding two-phase flows could deliver more accurate results for the pressure fluctuations and the impact on the fatigue in low-load operation.

Bibliography

- [1] J. Arpe, C. Nicolet, and F. Avellan. Experimental Evidence of Hydroacoustic Pressure Waves in a Francis Turbine Elbow Draft Tube for Low Discharge Conditions. *Journal of Fluids Engineering*, 131(8):81102, 2009.
- [2] J. Arpin-Pont, M. Gagnon, A. S. Tahan, A. Coutu, and D. Thibault. Strain gauge measurement uncertainties on hydraulic turbine runner blade. *IOP Conference Series: Earth and Environmental Science*, 15(6):062042, 2012.
- [3] J. Arpin-Pont, M. Gagnon, A. S. Tahan, A. Coutu, and D. Thibault. Methodology for estimating strain gauge measurement biases and uncertainties on isotropic materials. *The Journal of Strain Analysis for Engineering Design*, 50(1):40–50, 2015.
- [4] C. Bauer. *Hydraulische Maschinen und Anlagen I & II*. Vorlesungsskriptum, TU Wien, 2015.
- [5] J. Blazek. *Computational fluid dynamics: Principles and applications*. Elsevier Science, Oxford, 2. edition, 2005.
- [6] J. Boussinesq. *Essai sur la théorie des eaux courantes*. Mémoires présentées par divers savants à l’Académie des Sciences. Imprimerie Nationale, 1877.
- [7] M. W. Brown and K. J. Miller. A theory for fatigue failure under multiaxial stress–strain conditions. *Proceedings of the Institution of Mechanical Engineers 1847-1982*, 187:745–755, 1973.
- [8] L. S. Caretto, A. D. Gosman, S. V. Patankar, and D. B. Spalding. Two Calculation Procedures for Steady, Three-Dimensional Flows with Recirculation. *Proceedings of the 3rd International Conference on Numerical Methods in Fluid Mechanics*, pages 60–68, 1972.
- [9] B. Celik, U. Ghia, P. Roache, C. Freitas, H. Coleman, and P. Raad. Procedure for Estimation and Reporting of Uncertainty Due to Discretization in CFD Applications. *Journal of Fluids Engineering*, 130(7):078001, 2008.
- [10] R. W. Clough and J. Penzien. *Dynamics of Structures*. Computers & Structures, Inc., Berkeley, USA, 3rd edition, 1995.
- [11] L. F. Coffin, jr. A study of the effects of cyclic thermal stresses on a ductile metal. In *Transactions of the ASME*, volume 76, pages 931–950. 1954.

- [12] Ph. Conrad, W. Weber, and A. Jung. Deep Part Load Flow Analysis in a Francis Model turbine by means of two-phase unsteady flow simulations. *Journal of Physics: Conference Series*, 813(1):012027, 2017.
- [13] A. Coutu and J. Chamberland-Lauzon. The impact of flexible operation on Francis runners. *International Journal on Hydropower & Dams*, Issue Two:90–93, 2015.
- [14] A. Coutu, H. Aunemo, B. Badding, and O. Velagandula. Dynamic behaviour of high head Francis turbines. In *Conference Proceedings of HYDRO*, 2005.
- [15] A. Coutu, C. Monette, and O. Velagandula. Francis runner dynamic stress calculations. In *Conference Proceedings of HYDRO*, 2007.
- [16] P. Dörfler, M. Sick, and A. Coutu. *Flow-induced pulsation and vibration in hydro-electric machinery: Engineer’s guidebook for planning, design and troubleshooting*. Springer, London and New York, 2013.
- [17] U. Dorji and R. Ghomashchi. Hydro turbine failure mechanisms: An overview. *Engineering Failure Analysis*, 44:136–147, 2014.
- [18] F. Duparchy, J. Brammer, M. Thibaud, A. Favrel, P. Y. Lowys, and F. Avellan. Mechanical impact of dynamic phenomena in Francis turbines at off design conditions. *Journal of Physics: Conference Series*, 813(1):012035, 2017.
- [19] Y. Egorov and F. Menter. Development and Application of SST-SAS Turbulence Model in the DESIDER Project. *Second Symposium on Hybrid RANS-LES Methods*, 2007.
- [20] E. Egusquiza, C. Valero, X. Huang, E. Jou, A. Guardo, and C. Rodriguez. Failure investigation of a large pump-turbine runner. *Engineering Failure Analysis*, 23:27–34, 2012.
- [21] ENTSO-E. European network of transmission system operators for electricity. URL <https://transparency.entsoe.eu/>. Accessed February 07, 2017.
- [22] S. Erne. *Numerical Investigation of Part-Load Flows in a Pump-Turbine affected by System Rotation*. PhD Thesis, TU Wien, 2013.
- [23] European Commission. *A Roadmap for moving to a competitive low carbon economy in 2050*. Brussels, 2011.
- [24] Eurostat. *Energy, transport and environment indicators*. Publications Office of the European Union, Luxemburg, 2015.
- [25] J. Ferziger and M. Peric. *Numerische Strömungsmechanik*. Springer Berlin Heidelberg, 2008.
- [26] F. Flemming, J. Foust, J. Koutnik, and R. K. Fisher. Overload Surge Investigation Using CFD Data. *International Journal of Fluid Machinery and Systems*, 2(4):315–323, 2009.

- [27] M. Flores, G. Urquiza, and J. M. Rodríguez. A Fatigue Analysis of a Hydraulic Francis Turbine Runner. *World Journal of Mechanics*, 02(01):28–34, 2012.
- [28] D. Frunzăverde, S. Muntean, G. Mărginean, V. Câmpian, L. Marşavina, R. Terzi, and V. Şerban. Failure analysis of a Francis turbine runner. *IOP Conference Series: Earth and Environmental Science*, 12:012115, 2010.
- [29] M. Gagnon, S. A. Tahan, P. Bocher, and D. Thibault. Impact of startup scheme on Francis runner life expectancy. *IOP Conference Series: Earth and Environmental Science*, 12:012107, 2010.
- [30] M. Gagnon, A. Tahan, P. Bocher, and D. Thibault. The role of high cycle fatigue (HCF) onset in Francis runner reliability. *IOP Conference Series: Earth and Environmental Science*, 15(2):022005, 2012.
- [31] M. Gagnon, A. Tahan, P. Bocher, and D. Thibault. On the stochastic simulation of hydroelectric turbine blades transient response. *Mechanical Systems and Signal Processing*, 32:178–187, 2012.
- [32] M. Gagnon, A. Tahan, P. Bocher, and D. Thibault. Influence of load spectrum assumptions on the expected reliability of hydroelectric turbines: A case study. *Structural Safety*, 50:1–8, 2014.
- [33] E. Gaßner, O. Buxbaum, H. Ostermann, and H. Rückert. *Ausfallsichere Bemessung von Laufrädern für Wasserkraftmaschinen aus rostfreiem Stahlguss unter Berücksichtigung von Korrosion und Gefügestand: Abschlussbericht zum Gemeinschaftsprogramm "Stahlguß"*. Fraunhofer-Institut für Betriebsfestigkeit, Darmstadt, 1983.
- [34] J. Giesecke and E. Mosonyi. *Wasserkraftanlagen*. Springer Berlin Heidelberg, 2009.
- [35] J. Goodman. *Mechanics applied to engineering*. Longmans, Green and Co, London, 1904.
- [36] B. Graf and L. Chen. Correlation of Acoustic Fluid-Structural Interaction Method for Modal Analysis with experimental results of a Hydraulic Prototype Turbine Runner in Water. *Proceedings of ISMA2010 including USD2010*, 2010.
- [37] R. Guillaume, J. L. Deniau, D. Scolaro, and C. Colombet. Influence of the rotor-stator interaction on the dynamic stresses of Francis runners. *IOP Conference Series: Earth and Environmental Science*, 15(5):052011, 2012.
- [38] M. Guittet, M. Capezzali, L. Gaudard, F. Romerio, F. Vuille, and F. Avellan. Study of the drivers and asset management of pumped-storage power plants historical and geographical perspective. *Energy*, 111:560–579, 2016.
- [39] E. Haibach. *Betriebsfestigkeit: Verfahren und Daten zur Bauteilberechnung*. VDI-Buch. Springer, Berlin, 3rd edition, 2006.
- [40] B. P. Haigh. *Report on alternating stress tests of sample of mild steel*. British Association Stress Committee, Manchester, UK, 1915.

- [41] E. Hairer and G. Wanner. *Solving Ordinary Differential Equations. II, Stiff and Differential - Algebraic Problems*, volume 14 of *Springer series in computational mathematics*. Springer, Berlin, 1991.
- [42] B. Hänel, E. Haibach, T. Seeger, G. Wirthgen, and H. Zenner. *Rechnerischer Festigkeitsnachweis für Maschinenbauteile aus Stahl, Eisenguss- und Aluminiumwerkstoffen*. FKM-Richtlinie. VDMA-Verl., Frankfurt am Main, 5. edition, 2003.
- [43] X. Huang, C. Oram, and M. Sick. Static and dynamic stress analyses of the prototype high head Francis runner based on site measurement. *IOP Conference Series: Earth and Environmental Science*, 22(3):032052, 2014.
- [44] B. Hübner, U. Seidel, and S. Roth. Application of fluid-structure coupling to predict the dynamic behavior of turbine components. *IOP Conference Series: Earth and Environmental Science*, 12:012009, 2010.
- [45] H.-J. Huth. *Fatigue Design of Hydraulic Turbine Runners*. PhD Thesis, Norwegian University of Science and Technology (NTNU), Trondheim, 2005.
- [46] R. I. Issa. Solution of the implicitly discretised fluid flow equations by operator-splitting. *Journal of Computational Physics*, 62(1):40–65, 1986.
- [47] P. Johannesson. Extrapolation of load histories and spectra. *Fatigue Fracture of Engineering Materials and Structures*, 29(3):209–217, 2006.
- [48] H. Keck and M. Sick. Thirty years of numerical flow simulation in hydraulic turbomachines. *Acta Mechanica*, 201(1-4):211–229, 2008.
- [49] M. Köhler, S. Jenne, K. Pötter, and H. Zenner. *Zählverfahren und Lastannahme in der Betriebsfestigkeit*. Springer Berlin Heidelberg, 2012.
- [50] T. Krappel, A. Ruprecht, S. Riedelbauch, R. Jester-Zuerker, and A. Jung. Investigation of Francis Turbine Part Load Instabilities using Flow Simulations with a Hybrid RANS-LES Turbulence Model. *IOP Conference Series: Earth and Environmental Science*, 22(3):032001, 2014.
- [51] S. Lais, Q. W. Liang, U. Henggeler, and T. Weiss. Dynamic Analysis of Francis Runners - Experiment and Numerical Simulation. *International Journal of Fluid Machinery and Systems*, 2(4), 2009.
- [52] B. E. Launder and D. B. Spalding. The numerical computation of turbulent flows. *Computer Methods in Applied Mechanics and Engineering*, 3(2):269–289, 1974.
- [53] M. Lenarcic and Ch. Bauer. Numerical investigations of the unsteady flow in a high-head Francis turbine using FOAM-extend. *WasserWirtschaft Extra*, 13/2015:33–37, 2015.
- [54] M. Lenarcic, M. Eichhorn, S. J. Schoder, and C. Bauer. Numerical investigation of a high head Francis turbine under steady operating conditions using foam-extend. *Journal of Physics: Conference Series*, 579:012008, 2015.

-
- [55] W. Leonard et al. *Energy storage in power supply systems with a high share of renewable energy sources: Significance, state of the art, need for action*. VDE, Frankfurt am Main, 2008.
- [56] Q. W. Liang, C. G. Rodriguez, E. Egusquiza, X. Escaler, M. Farhat, and F. Avelan. Numerical simulation of fluid added mass effect on a Francis turbine runner. *Computers & Fluids*, 36(6):1106–1118, 2007.
- [57] Q. W. Liang, S. Lais, C. Gentner, and O. Braun. Efficient runner safety assessment during early design phase and root cause analysis. *IOP Conference Series: Earth and Environmental Science*, 15(5):052009, 2012.
- [58] X. Liu, Y. Luo, and Z. Wang. A review on fatigue damage mechanism in hydro turbines. *Renewable and Sustainable Energy Reviews*, 54:1–14, 2016.
- [59] J. Löfflad and M. Eissner. Life time assessment and plant operation optimization based on geometry scan and strain gauge testing – START/STOP optimization. *The 10th International conference on hydraulic efficiency measurements*, 2014.
- [60] J. Löfflad, M. Eissner, and B. Graf. Strain gauge measurements of rotating parts with telemetry. *The 9th International conference on hydraulic efficiency measurements*, 2012.
- [61] M. V. Magnoli. *Numerical simulation of pressure oscillations in large Francis turbines at partial and full load operating conditions and their effects on the runner structural behaviour and fatigue life*. PhD Thesis, TU München, 2014.
- [62] M. V. Magnoli and M. Maiwald. Influence of Hydraulic Design on Stability and on Pressure Pulsations in Francis Turbines at Overload, Part Load and Deep Part Load based on Numerical Simulations and Experimental Model Test Results. *IOP Conference Series: Earth and Environmental Science*, 22(3):032013, 2014.
- [63] S. S. Manson. Fatigue: A complex subject - Some simple approximations. *Experimental Mechanics*, 5(4):193–226, 1965.
- [64] M. Matsuishi and T. Endo. Fatigue of metals subjected to varying stress. *Japan Society of Mechanical Engineers*, 1968.
- [65] F. R. Menter. Zonal Two Equation k-omega Turbulence Models for Aerodynamic Flows. *AIAA 24th Fluid Dynamics Conference*, 1993.
- [66] F. R. Menter. Two-equation eddy-viscosity turbulence models for engineering applications. *AIAA Journal*, 32(8):1598–1605, 1994.
- [67] F. R. Menter and Y. Egorov. A Scale Adaptive Simulation Model using Two-Equation Models. *43rd AIAA Aerospace Sciences Meeting and Exhibit*, 2005.
- [68] K. J. Miller. Fatigue under complex stress. *Metal Science*, pages 432–438, 1977.
- [69] M. A. Miner. Cumulative damage in fatigue. *Journal of applied mechanics*, 12, 3, pages 159 – 164, 1945.

- [70] C. Monette, H. Marmont, J. Chamberland-Lauzon, A. Skagerstrand, A. Coutu, and J. Carlevi. Cost of enlarged operating zone for an existing Francis runner. *IOP Conference Series: Earth and Environmental Science*, 49:072018, 2016.
- [71] W. Montero, R. Farag, V. Díaz, M. Ramirez, and B. L. Boada. Uncertainties associated with strain-measuring systems using resistance strain gauges. *The Journal of Strain Analysis for Engineering Design*, 46(1):1–13, 2011.
- [72] J. F. Morissette, J. Chamberland-Lauzon, B. Nennemann, C. Monette, A. M. Giroux, A. Coutu, and J. Nicolle. Stress predictions in a Francis turbine at no-load operating regime. *IOP Conference Series: Earth and Environmental Science*, 49:072016, 2016.
- [73] J. Morrow. Cyclic Plastic Strain Energy and Fatigue of Metals. *ASTM STP 378*, pages 45–87, 1965.
- [74] B. Nennemann, J. F. Morissette, J. Chamberland-Lauzon, C. Monette, O. Braun, M. Melot, A. Coutu, J. Nicolle, and A. M. Giroux. Challenges in Dynamic Pressure and Stress Predictions at No-Load Operation in Hydraulic Turbines. *IOP Conference Series: Earth and Environmental Science*, 22(3):032055, 2014.
- [75] N. M. Newmark. A Method of Computation for Structural Dynamics. *ASCE Journal of Engineering Mechanics Division*, 85, pages 67–94, 1959.
- [76] OpenFOAM Foundation. OpenFOAM User Guide: Version 2.3.1, 2014.
- [77] M. Page, M. Beaudoin, and A. M. Giroux. Steady-state capabilities for hydroturbines with OpenFOAM. *IOP Conference Series: Earth and Environmental Science*, 12: 012076, 2010.
- [78] A. Palmgren. Die Lebensdauer von Kugellagern. *VDI Zeitschrift*, 68, 14, pages 339 – 341, 1924.
- [79] J. Pople. *Errors and uncertainties in strain measurement*. Elsevier Applied Science. London, 2. edition, 1992.
- [80] J. Raabe. *Hydro power: The design, use, and function of hydromechan., hydraul., and electr. equipment*. VDI-Verl., Düsseldorf, 1985.
- [81] F. G. Rammerstorfer. *Grundlagen der Finite Elemente Methoden*. Vorlesungsskriptum, TU Wien, 2008.
- [82] S. Rehman, L. M. Al-Hadhrani, and Md. M. Alam. Pumped hydro energy storage system: A technological review. *Renewable and Sustainable Energy Reviews*, 44:586–598, 2015.
- [83] J. C. Rotta. *Turbulente Strömungen*. Vieweg+Teubner Verlag, Wiesbaden, 1972.
- [84] R. Schilling, H.-P. Ernst, C. Watzelt, and W. Knapp. Investigation of the incidence and deviation angles in high specic speed Francis Turbine. *Proceedings of the 16th IAHR Symposium on Hydraulic Machinery and Systems*, (vol. 2):779–788, 1992.

- [85] W. Schütz and H. Zenner. Schadensakkumulationshypothesen zur Lebensdauer-vorhersage bei schwingender Beanspruchung. Teil 1. - Ein kritischer Überblick. *Materialwissenschaft und Werkstofftechnik*, 4(1):25–33, 1973.
- [86] U. Seidel, B. Hübner, J. Löfflad, and P. Faigle. Evaluation of RSI-induced stresses in Francis runners. *26th IAHR Symposium on Hydraulic Machinery and Systems*, 2012.
- [87] U. Seidel, C. Mende, B. Hübner, W. Weber, and A. Otto. Dynamic loads in Francis runners and their impact on fatigue life. *IOP Conference Series: Earth and Environmental Science*, 22(3):032054, 2014.
- [88] M. Sick, W. Michler, T. Weiss, and H. Keck. Recent developments in the dynamic analysis of water turbines. *Proceedings of the Institution of Mechanical Engineers, Part A: Journal of Power and Energy*, 223(4):415–427, 2009.
- [89] J. Smagorinsky. General Circulation Experiments with the Primitive Equations. *Monthly Weather Review*, 91(3):99–164, 1963.
- [90] P. Spalart and S. Allmaras. A one-equation turbulence model for aerodynamic flows. *30th AIAA Aerospace Sciences Meeting and Exhibit*, 1992.
- [91] O. Teller et al. *European Energy Storage Technology Development Roadmap towards 2030*. EASE/EERA Core Working Group, Brussels, 2013.
- [92] D. Thibault, M. Gagnon, and S. Godin. Bridging the gap between metallurgy and fatigue reliability of hydraulic turbine runners. *IOP Conference Series: Earth and Environmental Science*, 22(1):012019, 2014.
- [93] C. Trivedi and M. J. Cervantes. Fluid-structure interactions in Francis turbines: A perspective review. *Renewable and Sustainable Energy Reviews*, 68:87–101, 2017.
- [94] C. Trivedi, M. J. Cervantes, B. K. Gandhi, and O. G. Dahlhaug. Experimental and Numerical Studies for a High Head Francis Turbine at Several Operating Points. *Journal of Fluids Engineering*, 135(11):111102, 2013.
- [95] C. Trivedi, B. K. Gandhi, and M. J. Cervantes. Effect of transients on Francis turbine runner life: A review. *Journal of Hydraulic Research*, 51(2):121–132, 2013.
- [96] C. Trivedi, M. J. Cervantes, O. G. Dahlhaug, and B. K. Gandhi. Experimental Investigation of a High Head Francis Turbine During Spin-No-Load Operation. *Journal of Fluids Engineering*, 137(6):061106, 2015.
- [97] P. Unterberger. *Development of a Multistage Pump-Turbine for Decentralized Small Hydro Applications*. PhD Thesis, TU Wien, 2014.
- [98] D. Valentín, D. Ramos, M. Bossio, A. Presas, E. Egusquiza, and C. Valero. Influence of the boundary conditions on the natural frequencies of a Francis turbine. *IOP Conference Series: Earth and Environmental Science*, 49:072004, 2016.

-
- [99] D. Valentín, A. Presas, E. Egusquiza, C. Valero, and M. Bossio. Dynamic response of the MICA runner. Experiment and simulation. *Journal of Physics: Conference Series*, 813(1):012036, 2017.
- [100] O.V. Vasilyev, T. S. Lund, and P. Moin. A General Class of Commutative Filters for LES in Complex Geometries. *Journal of Computational Physics*, 146(1):82–104, 1998.
- [101] M. Wachauer. *Numerische Lebensdauerberechnung einer Francis Turbine im Auslegungspunkt*. Diploma Thesis, TU Wien, 2016.
- [102] C. H. Wang and M. W. Brown. Life Prediction Techniques for Variable Amplitude Multiaxial Fatigue - Part 1: Theories. *Journal of Engineering Materials and Technology*, 118(3):367, 1996.
- [103] C. H. Wang and M. W. Brown. Inelastic deformation and fatigue under complex loading. *Proceedings of the 12th International Conference on Structural Mechanics in Reactor Technology*, pages 159 – 170, 1997.
- [104] W. Weber, F. Locquenghien, Ph. Conrad, and Jiri Koutnik. Dynamic stresses in a Francis model turbine at deep part load. *Journal of Physics: Conference Series*, 813(1):012014, 2017.
- [105] D. C. Wilcox. Reassessment of the scale-determining equation for advanced turbulence models. *AIAA Journal*, 26(11):1299–1310, 1988.
- [106] K. Yamamoto, A. Müller, A. Favrel, C. Landry, and F. Avellan. Flow characteristics and influence associated with inter-blade cavitation vortices at deep part load operations of a Francis turbine. *Journal of Physics: Conference Series*, 813(1):012029, 2017.
- [107] K. Zach, H. Auer, G. Körbler, and G. Lettner. *The Role of Bulk Energy Storage in Facilitating Renewable Energy Expansion*. Wien, 2012.

Appendix A

Uncertainty Assessment

To achieve a proper assessment of the static and dynamic stresses measured with strain gauges and to validate the numerical simulations, the possible uncertainties resulting from measurement and modeling approaches have to be discussed. This will be done in the following sections by means of the high head Francis turbine.

A.1 Strain Gauge Measurements

According to Arpin-Pont et al. [2, 3] measurements using strain gauges are subject to biases (systematic errors) and uncertainties (random errors), which influence the estimated or true value. Pople [79] observed more than 70 sources for uncertainties, which are displayed in groups in Fig. A.1. According to Montero et al. [71] the most important influences are the measurement device, the positioning of the strain gauge, the temperature, the sensitivity due to transverse strains and the non-linearity of the Wheatstone bridge. Arpin-Pont et al. [2, 3] developed a methodology to estimate the biases and uncertainties due to the location

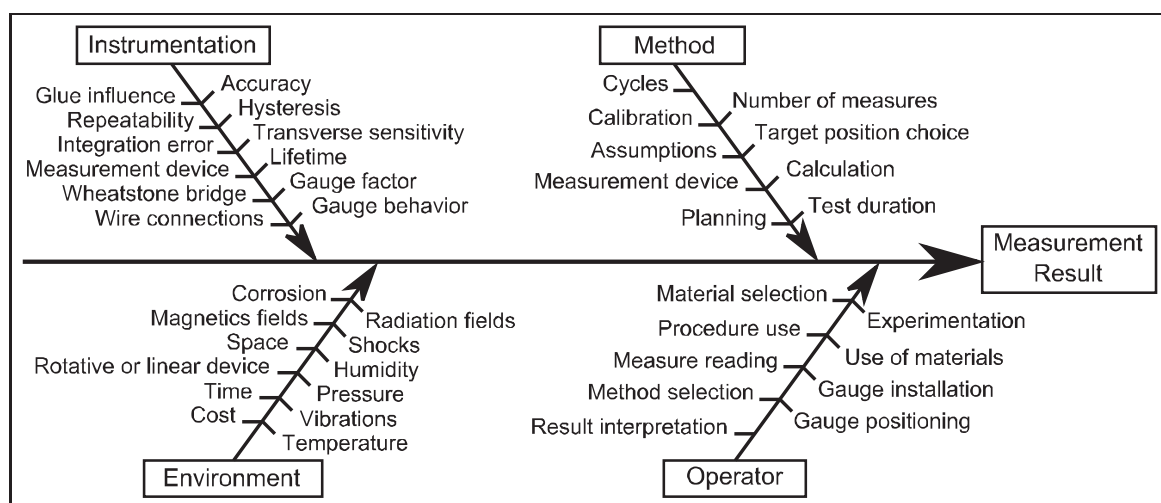


Figure A.1: Strain gauge measurement uncertainties. Graphics from Arpin-Pont et al. [3].

and misalignment error, the integration effect and the transverse sensitivity error. This approach is based on statistical Monte Carlo simulations using virtual strain gauges in a Finite Element Analysis. This is especially useful for welded gauges with a non-negligible impact of positioning errors but requires also a large effort. For bonded strain gauges, which have been used for the measurement procedures described in the scope of this thesis, those influences may be less. However, if high strain gradients appear in the area around the intended target location (e.g. close to notches) the uncertainties can be significant too. The stress variation at the strain gauge positions will be discussed on the basis of the FEM simulations in the following section. Due to complicated installation conditions of the sensors at the hydraulic turbine blades a total measurement error of $E_m = 5\%$ is considered. Temperature fluctuations as well as an eventual slip of the bonded strain gauges between the beginning and the end of the measurement procedure have been already considered by a drift correction. In Fig. A.2 the static and dynamic stresses of the high head Francis turbine are displayed including the measurement error E_m and the standard deviation of the temporal fluctuations.

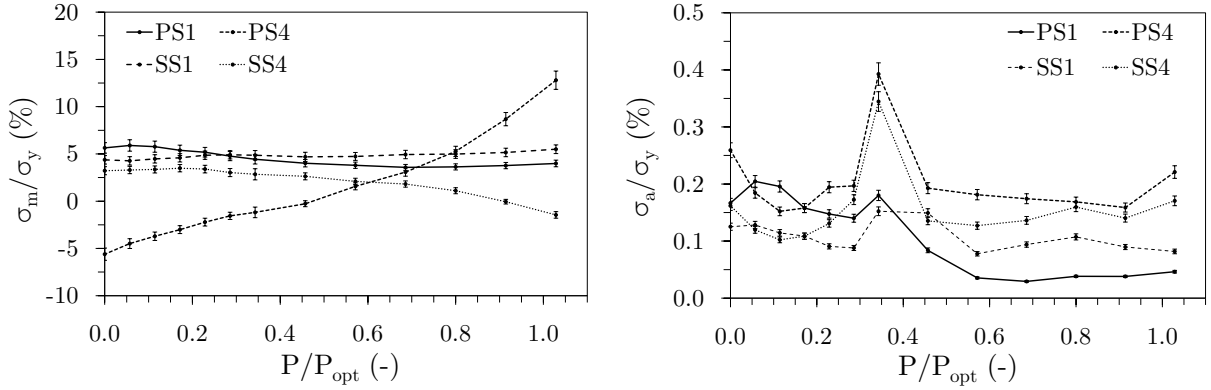


Figure A.2: Measured static (left) and dynamic stresses (right) for PSP-HH including the measurement uncertainties.

A.2 Numerical Simulations

A.2.1 CFD Simulations

Similar to measurement approaches a non-negligible amount of uncertainties remain as well for the results of numerical flow simulations. Different kind of error types are responsible for those uncertainties, which can be categorized according to Fig. A.3. One error source is the numerical approximation of the Navier-Stokes equations to solve the complex flow in hydraulic turbomachines. Further, physical parameters and model definitions like an incompressible fluid are based on simplifications introducing additional errors. Multiphase simulation approaches may increase the accuracy but also the computational effort. As previously discussed, turbulence modeling has a major impact on the numerical results of a fluid flow. To obtain its influence different models have been used in the scope of this thesis. Another possible source for deviations belongs to the discretization and the according

interpolation schemes. To keep the introduced errors at an appropriate low level second order approaches have been applied for both spatial and temporal discretization methods. To obtain the numerical uncertainty due to the spatial discretization regarding the mesh density a grid convergence study has been performed using the Richardson extrapolation technique. The procedure and results have been described already in Chap. 6. As the quality of the used meshes considering the orthogonality and cell ratio has also a significant impact on the accuracy of the results, appropriate limits have been observed. The usage of a finite number of iteration steps introduces a truncation error, which has been minimized by an according convergence criteria. The stability and accuracy of the CFD simulations have been ensured by an appropriate physical time step size and a limited Courant number.

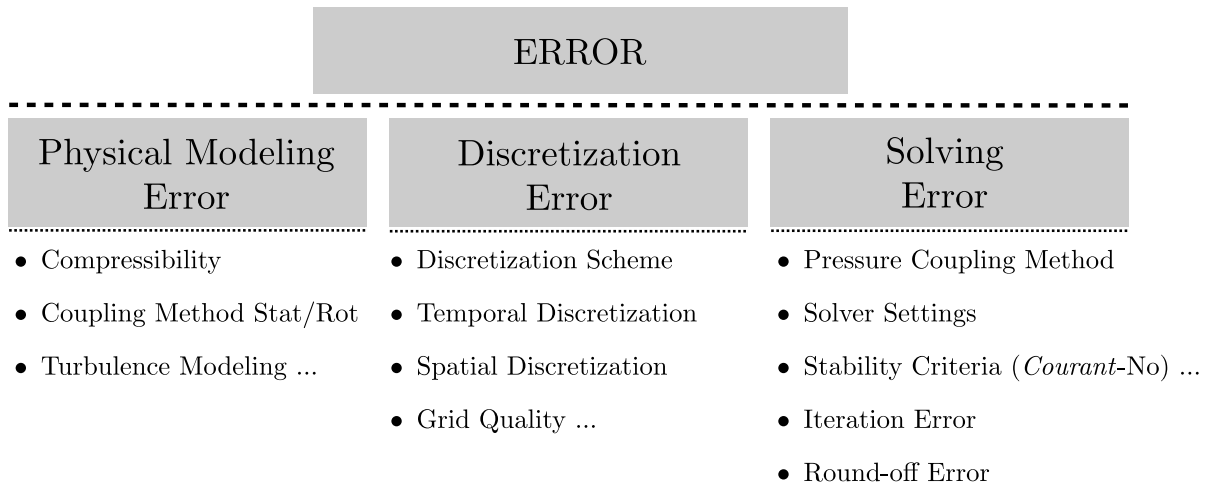


Figure A.3: Different types of error sources for CFD simulations. Graphics from Erne [22].

A.2.2 FEM Simulations

The error sources for the FEM simulations can be considered similar to the CFD computations. Simplifications of physical parameters and models but also geometrical deviations can lead to significant uncertainties. Therefore, the existing geometry of the investigated runner blade for the high head Francis turbine has been surveyed and the material data has been observed from technical reports. The discretization process has also a major impact on the numerical error. To assure reliable and accurate results, a second order interpolation approach has been used for the tetrahedral structural grids. To obtain the influence of the mesh density on the FEM simulations due to the spatial discretization, a grid convergence study according to Celik et al. [9], similar to the CFD computations, is performed and discussed as follows.

At first, the results for the static FEM analysis are assessed using three different mesh densities for the cyclic model of the high head runner. The grid densities and the refinement factor for the coarse (G3), medium (G2) and fine grid (G1) are summarized in Tab. A.1. For the evaluation of the grid convergence study static FEM simulations are performed using the centrifugal forces induced by the runner rotation at the nominal rotational speed.

Table A.1: Mesh densities of the cyclic runner model for PSP-HH.

	Coarse grid	Medium grid	Fine grid
Number of cells N_c	40,627	103,277	230,835
Number of nodes n_n	83,551	217,876	495,194
Normalized mesh size h_n	1.78	1.31	1.00
Grid refinement factor r_g	-	1.36	1.31

The resulting stresses at the strain gauge positions PS1, PS4, SS1 and SS4 are used to assess the numerical error. The results are displayed in Fig. A.4 (left) revealing a monotonic convergence for each sensor position. The maximum relative error e_{ext}^2 for the medium grid with the normalized mesh size $h_n^2 = 1.31$ compared to the extrapolated value appears at PS4 with $e_{ext}^2 \approx 2.4\%$. The medium sized mesh has been used as well for the static FEM simulations of PSP-HH. In Fig. A.4 (right) the computed stresses with the medium grid are compared to the stresses measured at the synchronous condenser mode, where the turbine was running in air and therefore only the centrifugal forces were acting on the structure. For the strain gauge positions PS1 and PS3 no results are available due to sensor damages. The measurement uncertainty, consisting of the standard deviation of the stress variation along the time and the measurement error E_m , is figured as well. The stresses for the FEM simulations are obtained from all nodes at the strain gauge positions. To obtain the influence of the spatial discretization the stress variation for the different nodes are assessed using the standard deviation and displayed as well. As the sensors PS1, PS4, SS1 and SS4 have been attached close to the notches of the runner, the spatial difference is bigger than for the other strain gauges. The comparison reveals a proper agreement for the numerical simulations. Only for the sensors SS2 and SS3 the deviations from the measurements are more significant.

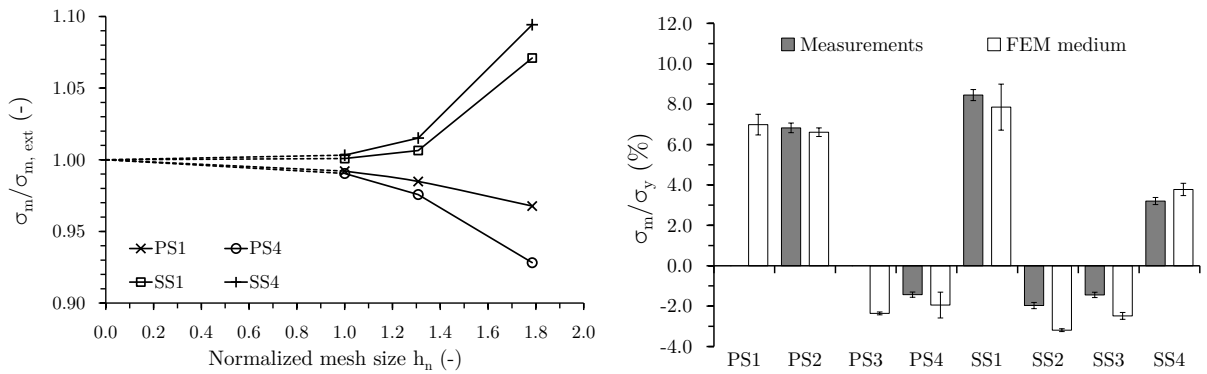


Figure A.4: Grid convergence (left) and comparison of the medium mesh with the measured stresses (right) for the static FEM analysis using the cyclic runner model of PSP-HH.

To assess the numerical error of the dynamic structural investigations a grid convergence study is performed for the full runner geometry of the high head Francis turbine. Therefore, static FEM simulations are performed similar to the previously described investigation as

Table A.2: Mesh densities of the full runner model for PSP-HH.

	Coarse grid	Medium grid	Fine grid
Number of cells N_c	105,790	228,113	611,531
Number of nodes n_n	208,557	458,981	1,214,028
Normalized mesh size h_n	1.80	1.39	1.00
Grid refinement factor r_g	-	1.30	1.39

well as a modal analysis for three different mesh sizes to obtain the influence on the natural eigenfrequencies of the structure. The grid densities and the refinement factor for the coarse (G3), medium (G2) and fine grid (G1) of the full runner geometry are summarized in Tab. A.2. The stresses at the four strain gauge positions computed by the static FEM simulations using the full runner model are displayed in Fig. A.5 (left) revealing a monotonic convergence. The maximum relative error e_{ext}^2 for the medium grid with the normalized mesh size $h_n^2 = 1.39$ compared to the extrapolated value appears at PS4 with $e_{ext}^2 \approx 1.8\%$. The medium sized mesh has been used as well for the dynamic FEM simulations of PSP-HH. In Fig. A.5 (right) the computed stresses with the medium grid are compared to the stresses measured at the synchronous condenser mode. The comparison reveals a proper agreement for the numerical simulations similar to the grid convergence study for the cyclic model.

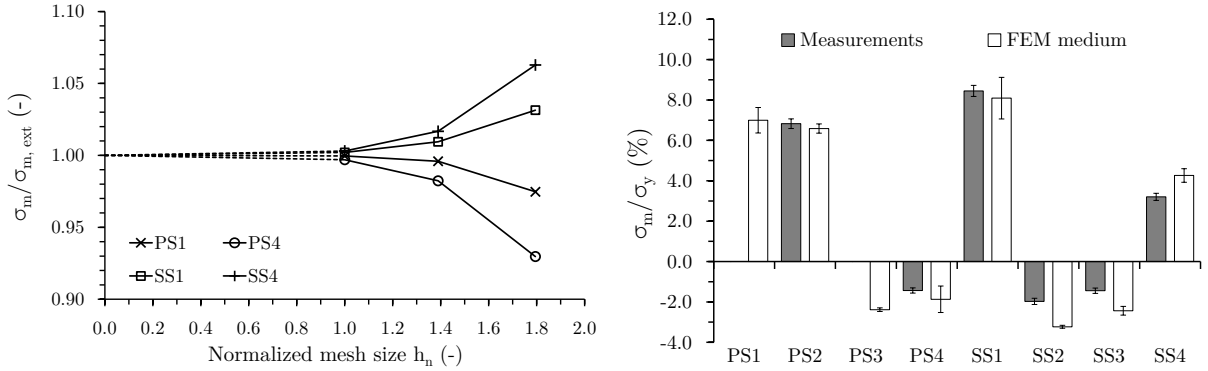


Figure A.5: Grid convergence (left) and comparison of the medium mesh with the measured stresses (right) for the static FEM analysis using the full runner model of PSP-HH.

In Fig. A.6 the influence of the mesh density on the eigenfrequencies f of the first five natural modes is displayed. The results reveal a monotonic convergence for all observed eigenmodes. The maximum relative error e_{ext}^2 appears at mode five for the medium grid compared to the extrapolated value with $e_{ext}^2 \approx 3.5\%$.

For the total numerical error of the FSI simulations the uncertainties of the CFD and FEM computations from the different sources have to be considered.

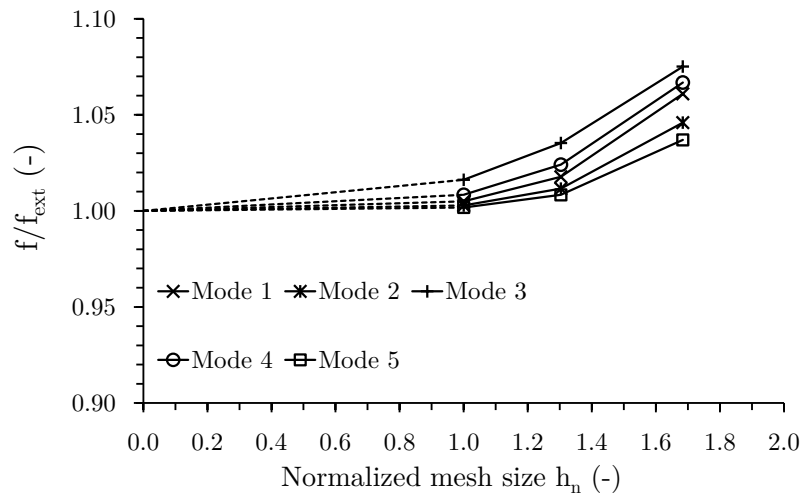


Figure A.6: Grid convergence for the first five eigenmodes of the full runner model of PSP-HH

Markus Eichhorn

Curriculum Vitae

Personal Details

Date of birth 9. März 1986, Vienna
Nationality Austria

Education

01/2013 **Diploma examination**, TU Wien
Passed with excellent success

10/2005 – 12/2012 **Study of Mechanical Engineering**, TU Wien
Focus on: Hydraulic machinery and systems, Thermodynamics

09/1996 – 06/2004 **Higher school degree**, Bundesgymnasium und Bundesrealgymnasium Laa/Thaya
Passed with good success

Community Service

10/2004 – 09/2005 **Caritas Mobile Dienste**, Haugsdorf

Work Experience

04/2013 – 05/2017 **Project assistant**, TU Wien
Institute for Energy systems and Thermodynamics, Research Group for Fluid-Flow Machinery

07/2011 – 08/2011 **Internship**, Höller Elektrotechnik GmbH, Untermarkersdorf
Electric installations, Assembly of photovoltaic systems

07/2010 – 08/2010 **Internship**, Tiroler Wasserkraft AG, Innsbruck
Design of hydraulic pumped storage plants

07/2009 – 09/2009 **Internship**, ODTec OG, Wien
Electric installations

07/2008 – 08/2008 **Internship**, Otto Bock Healthcare, Wien
Logistics/Commissioning

08/2007 **Internship**, Siemens AG, Wien
Inspection and implementation of protection and control devices

Languages

Native language **German**

Foreign language **English**, fluent (C1 - European Framework of Reference for Languages)

Software Skills

Operating systems Microsoft, Linux (Ubuntu, CentOS)

Text processing MS Office, Open Office, \LaTeX

CAD SolidWorks, CATIA V5, AutoCAD

CFD OpenFOAM, ANSYS CFX, Fluent, ICEM CFD, Star-CCM+

FEM Code_Aster, ANSYS Mechanical

Visualization ParaView, SALOME platform, CFD-Post, Gnuplot, TecPlot, SigmaPlot

Image processing Inkscape

Programming codes Python, C++

Data processing SciPy, MATLAB, LabVIEW

Publications and Scientific Work

Conference papers with presentation

- 02/2017 M. Eichhorn, A. Taruffi and C. Bauer: *Expected load spectra of prototype Francis turbines in low-load operation using numerical simulations and site measurements*. 7th IAHR Meeting of the Working Group on Cavitation and Dynamic Problems, Porto, 2017. In: *Journal of Physics: Conference Series*, 813/1, 012052
- 11/2016 M. Eichhorn, L. Waldner and C. Bauer: *Fatigue analysis of a medium head Francis runner at low-load operation using numerical investigations*. 19th International Seminar on Hydropower Plants, Vienna, 2016.
- 11/2016 M. Eichhorn and E. Doujak: *Impact of Different Operating Conditions on the Dynamic Excitation of a High Head Francis Turbine*. ASME 2016 International Mechanical Engineering Congress & Exposition, Phoenix, 2016.
- 07/2016 M. Eichhorn, E. Doujak and L. Waldner: *Investigation of the fluid-structure interaction of a high head Francis turbine using OpenFOAM and Code_Aster*. 28th IAHR Symposium on Hydraulic Machinery and Systems, Grenoble, 2016. In: *IOP Conference Series: Earth and Environmental Science*, 49, 072005.
- 11/2014 M. Eichhorn, E. Doujak and A. Schübl: *Cavitation measurements in hydraulic machines by using accelerometers*. 18th International Seminar on Hydropower Plants, Vienna, 2014.

Conference papers with contribution

- 11/2016 A. Maly, M. Eichhorn and C. Bauer: *Experimental investigation of transient pressure effects in the side chambers of a reversible pump turbine model*. 19th International Seminar on Hydropower Plants, Vienna, 2016.
- 11/2016 J. Unterluggauer, M. Eichhorn and E. Doujak: *Fatigue analysis of Francis turbines with different specific speeds using site measurements*. 19th International Seminar on Hydropower Plants, Vienna, 2016.
- 04/2016 E. Doujak and M. Eichhorn: *An Approach to Evaluate the Lifetime of a High Head Francis runner*. 16th International Symposium on Transport Phenomena and Dynamics of Rotating Machinery, Honolulu, 2016.
- 12/2014 M. Lenarcic, M. Eichhorn, S. Schoder and C. Bauer: *Numerical investigation of a high head Francis turbine under steady operating conditions using foam-extend*. 1st Francis-99 Workshop, Trondheim, 2014. In: *Journal of Physics: Conference Series*, 579, 012008.

Journal contributions

- 05/2015 M. Eichhorn, E. Doujak and A. Schübl: *Cavitation measurements in hydraulic machines by using accelerometers*. In: *Wasserwirtschaft Extra*, 105, S. 89 - 93, 2015.

Diploma thesis

- 01/2013 M. Eichhorn: *Velocity and acceleration measurements on the casing of hydraulic laboratory models*. *Diploma thesis*, TU Wien, 2013.

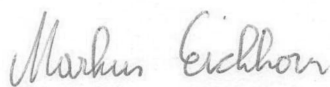
Cooperation in scientific projects

- 06/2013 – 05/2017 GSG - Green Storage Grid, Sub-project PSP-LowLoad: "Unsteady behavior of turbines and pump turbines in low-load operation".

Contribution to the application of scientific projects

- 09/2016 LIFE+: "Method development for the fatigue analysis of hydraulic turbines using condition optimized maintenance strategies".
- 10/2014 Top-/Anschubfinanzierung: "Detailed investigation of the transient behavior of a pump turbine in synchronous condenser and pump start-up operation".

Wien, 23. Mai 2017



Markus Eichhorn